Multi-Frequency Analysis of Intraday Variable Radio Sources

Dissertation

zur

Erlangung des Doktorgrades (Dr. rer. nat.)

der

Mathematisch-Naturwissenschaftlichen Fakultät

der

Rheinischen Friedrich-Wilhelms-Universität Bonn

vorgelegt von

Giuseppe Cimò

aus

Palermo (Italien)

Bonn 2003

Angefertigt mit Genehmigung der Mathematisch-Naturwissenschaftlichen Fakultät der Rheinischen Friedrich-Wilhelms-Universität Bonn

1. Referent: Prof. Dr. U. Klein

2. Referent: Priv. Doz. Dr. W. K. Huchtmeier

Tag der Promotion:

Contents

List of Tables

List of Figures

Introduction

Active Galactic Nuclei (AGN) show significant flux density variability across the whole electromagnetic spectrum on a wide range of time scales, from years to less than one day. Variations on intraday time scales have been detected in the γ-regime since the early experiments in this band (Mattox et al. 1993). In the optical band, rapid intranight variability has been observed both in total intensity and polarization (Angel and Stockman 1980). In the radio regime, variability on time scales of less than one day was discovered in the mid eighties (Witzel et al. 1986, Heeschen et al. 1987). It was also found (Quirrenbach et al. 1992) that about 30 % of all compact flat-spectrum sources show Intraday Variability (IDV).

While fast variations can be well explained at high energies (optical to γ-band) using models for accretion disks and relativistic jets, at cm-wavelengths, the observed rapid variations imply, via a causality argument, a very small source size and a very high apparent brightness temperature (of up to 10^{21} K), if we consider these variations as intrinsic. To prevent the "Compton catastrophe", which limits the brightness temperature to 10^{12} K (Kellermann and Pauliny-Toth 1969), IDV would require relativistic boosting with Doppler factors of up to $D = 1000$. This is much higher than so far observed with VLBI. Qian et al. (1996) proposed a modified shock-in-jet model, which relies on a special geometry, to prevent such high Doppler-factors. In this model, a thin shock moves relativistically along an oscillating jet. The observed brightness temperature, T_b^{obs}, then scales with the 5^{th} power of the intrinsic Lorenz factor and only moderate Doppler factors ($D \leq 60$) are needed.

Alternative models, which are based on collective plasma emission processes, allow brightness temperatures far in excess of the inverse Compton limit (Benford 1992, Benford and Lesch 1998). However, such models can explain high brightness temperatures only within a limited bandwidth (10–100 GHz), which makes hard to describe a

broad-band phenomenon as the Intraday Variability.

Another important process to consider is the radiation propagation through the Interstellar Medium (ISM). The sizes of intraday variable sources at cm-wavelengths appear to be typically smaller than the scattering size, set by the ISM in our galaxy. Hence, IDV sources show refractive interstellar scintillation (RISS). The variations in sources like 0917+62 can be explained mainly by RISS (cf. Rickett et al. 1995), but this explanation clearly fails in other sources like 0716+71 (Wagner and Witzel 1995), where correlated radio-optical IDV is present and most recently IDV at 9 mm has been detected (Krichbaum et al. 2002).
Evidence for RISS as being the main cause for rapid variability has recently become very strong in at least two sources: 0405−385 (Jauncey et al. 2000) and J1819+3845 (Dennett-Thorpe and de Bruyn 2000). In these objects, the extremely fast variability ($\sim 600\,\%$ in less than one hour) shows an annual modulation of the time scales, which is predicted by the RISS theory (Dennett-Thorpe and de Bruyn 2001) if the orbital motion of the Earth and the velocity of the scattering screen are taken into account.
In addition, interstellar scintillation is becoming a useful tool to detect microarcsecond structures in the radio cores of AGNs by using the interstellar medium as an interferometer (Macquart et al. 2002).
Due to small source sizes, either refractive interstellar scintillation (RISS) or source intrinsic effects or a mixture of both are possible causes for Intraday Variability. Therefore, observations at mm and submillimeter wavelengths are important, since they would help to disentangle between extrinsic (dominant at longer cm-wavelengths) and intrinsic (dominant at mm/optical-bands) contributions for the observed rapid variability.

Even 15 years after its discovery, Intraday Variability in flat-spectrum radio sources still remains a hot and controversial topic in astronomy and is still requiring an explanation. In the last decade a lot of effort was spent trying to disentangle the different mechanisms responsible for the observed rapid variations. In this work, we would like to provide a further contribution to the understanding of Intraday Variability. After an introduction to the observational characteristics of IDV (chapter 1), the data measured

in the last 15 years (chapter 2) will be used to perform a statistical analysis of the phenomenon (chapters 3 and 4). Also, recent RISS-related models will be compared to our data and physical parameters of the ISM and radio sources will be derived (chapters 5 and 6). High frequency approaches to search for rapid variability of flat-spectrum radio sources in total intensity and polarization were applied and the results will also be presented (chapters 7 and 8). Finally, an overall interpretation of the results and some implications about the physics of compact structures and the characteristics of the interstellar medium will be discussed (chapter 9).

Chapter 1

IntraDay Variability of Active Galactic Nuclei

Variability of active galactic nuclei on timescales of weeks to years is an useful instrument to study the inner regions of these objects. In the radio regime, total flux density and polarization variations on shorter timescales, less than one day, were discovered in the mid eighties (Witzel et al. 1986, Heeschen et al. 1987). Such Intraday Variability (IDV) has also been detected in other bands of the electromagnetic spectrum up to γ-ray energy.

1.1 Observational IDV

Intraday variability of flat-spectrum radio sources has been detected in all electromagnetic spectral bands. Rapid flares in Gamma-emission and optical fast variability seem to be related to radiative phenomena from central regions in AGNs. In the cm-regime, intraday variability is present in $\sim 30\,\%$ of all flat spectrum sources (Quirrenbach et al. 1992). The light curve of an IDV object shows variations at the $10-20\,\%$ level in total intensity with time scales from 0.5 up to 3 days (fig. 1.1, *top*) showing strict correlations among the frequencies. In some cases the light curves can also have time lags. Moreover, a factor 3 or more in the variability of the linearly polarized flux density is usually detected with similar time scales. Correlations and, in some cases, anti-correlation were observed between total intensity and polarization. Furthermore, the polarization angle showed very fast variations and in few cases a $180\,^\circ$-swing (Rickett et al. 1995).

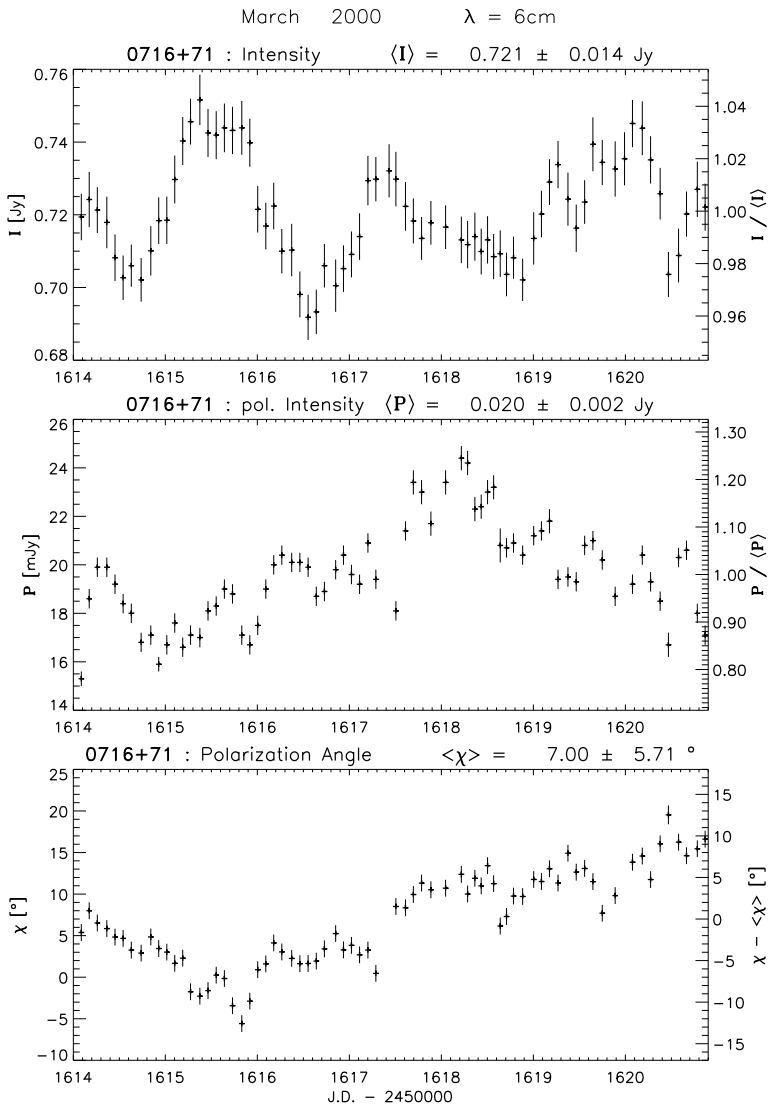

Figure 1.1: Typical light curve of an IDV source (0716+714). The top panel shows the total intensity variability. Polarization variations are plotted in the central panel. On the bottom, we see the behaviour of the polarization angle. (These data were observed in March 2000.)

Regarding the broad-band properties, simultaneous radio-optical observations were carried out and correlated features were observed in 0716+714 (Wagner et al. 1996, see fig. 1.2) and in 0958+658 (Wagner et al. 1993).

In the gravitational lens B0218+357, Biggs et al. (1999) discovered time delayed and correlated rapid variations in the lensed images. Such rapid variation (with time scale of $\sim$ 2 days in the source frame) is interpreted (Biggs et al. 2001) as intrinsic flux density change in the background object.

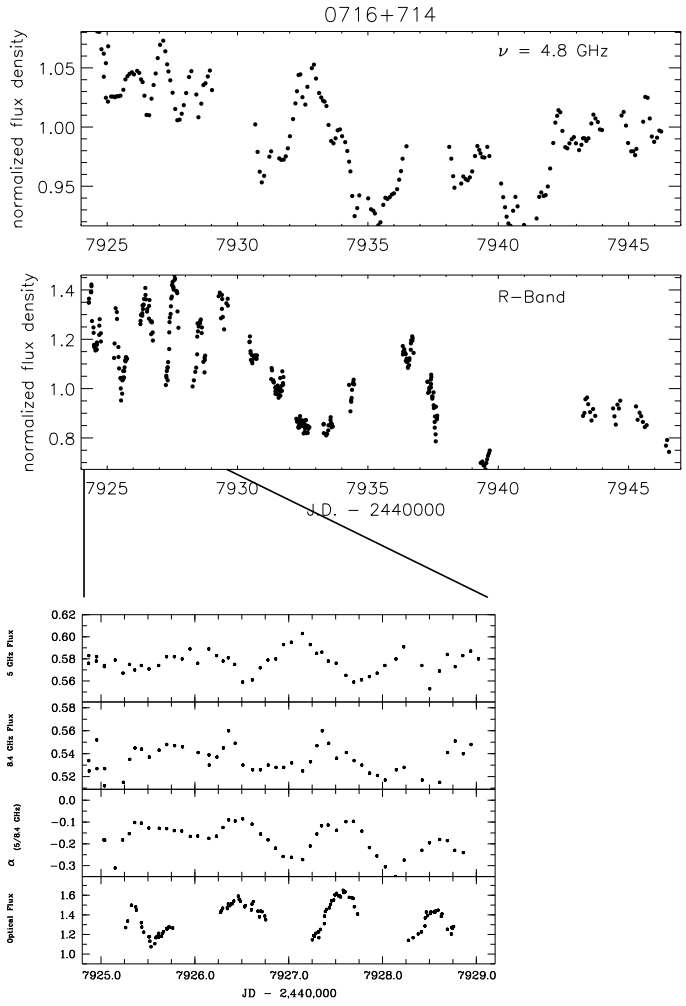

Figure 1.2: Correlated radio-optical IDV in 0716+714 observed in 1990 (Wagner et al. 1996). Note the mutual transition from fast 'quasi-periodic' variability mode to slower variations after J.D. 2447929.

1.2 Source-intrinsic variability

The light-travel (causality) argument sets a limit on the size of the emitting region:

$$\Delta l < c \cdot \Delta t \tag{1.1}$$

where Δl is the linear size of the variable emitting region, Δt is the time interval of the observed variation and c the speed of light (assumed as upper limit for the velocity of the perturbation).

If the variability is intrinsic, the very short time scales imply very small source sizes. Calculating the brightness temperature of the variable object (for typically observed

values of the flux density variation ΔS, luminosity distance D_L and redshift z):

$$T_b[\mathrm{K}] = 4.5 \cdot 10^{10} \cdot \Delta S[Jy] \cdot \left(\frac{\lambda[cm] \cdot D_L[Mpc]}{\Delta t[d] \cdot (1+\mathrm{z})} \right)^2 , \tag{1.2}$$

we obtain $T_b = 10^{14} - 10^{18}\,\mathrm{K}$ (up to 10^{21} for very extreme objects).
Such high temperatures would exceed the inverse Compton limit of$T_b = 10^{12}\,\mathrm{K}$ (Kellermann and Pauliny-Toth 1969) for incoherent synchrotron emission. Relativistic beaming of the radiation was suggested to avoid the Compton limit violation. Introducing the Doppler factor[1] $D = (\Gamma(1 - \frac{v}{c} \cdot \cos\theta))^{-1}$, the brightness temperature is reduced by D^{-3}. In particular, following the description of Verschuur and Kellermann (1988): $D^{-(3-\alpha)}$ for a blob moving inside the jet and $D^{-(2-\alpha)}$ for a continuous jet. We use $S \propto \nu^{-\alpha}$.

From relativistic considerations, the flux density measured from the observer, S_ν, is related to the flux density in the frame of the source, S_{int}, via the Doppler factor:

$$S_\nu = D^{3-\alpha}\, S_{int}. \tag{1.3}$$

The measured surface flux density is $S_\nu \propto L/\Omega$, where Ω is the solid angle seen by the observer and can be estimated via light-travel argument: $\Omega = c^2 \Delta t^2$.
Now, it is possible to evaluate the brightness temperature and from eq. 1.2 we obtain:

$$T_b \propto S_\nu / \nu^2. \tag{1.4}$$

Recalling the Lorentz transformation for the time ($\Delta t = \frac{1}{D} \cdot \Delta t_{int}$) and the frequency ($\nu = D \cdot \nu_{int}$) we immediately obtain:

$$T_b = D^3 \cdot T_b^{int} \tag{1.5}$$

The relativistic effects as the superluminal motions observed in the VLBI cores ($v_{app} \approx 40c$ Marscher et al. 2000), can explain only moderate values of D, but much higher values ($D = 100 - 1000$) would be needed to bring the brightness temperature down to $10^{12}\,\mathrm{K}$.

[1] $\Gamma = (1 - \frac{v^2}{c^2})^{-1/2}$ is the Lorentz factor.

1.2.1 Shock-in-Jet Model

Shocks moving inside jets can provide a possible explanation for the rapid flux density changes in the flat-spectrum radio sources. In these models, outbursts are produced by the acceleration of highly relativistic particles in a turbulent jet. Such models (eg. Qian et al. 1991) are able to reproduce the polarization features of IDV, but some problems still remain unexplained like the frequency dependence of the variations and the quasi-periodicity (about 2-3 days) of the variability that was observed in some sources.

Special geometry effects can be taken into account to solve the discrepancies between the models and the observational evidence. Thin shocks can illuminate the knots which are emitted at relativistic speed from the core in helical trajectories and with a viewing angle very close to the line of sight (Qian et al. 1996). In this case, frequency-correlated variations would be expected and it is possible to explain the quasi-periodicity of the phenomenon. Moreover the apparent brightness temperature can be reduced using only moderate Doppler and Lorentz factors: $T_b \propto \Gamma^2 D^3$ and the required factors are similar (even slightly greater) to those involved from superluminal motions (eg. Bach et al. 2002).

If these models can solve the inverse Compton limit violation, it is however hard to believe that such special geometry and very small viewing angles (Beckert et al. 2002b) are common in AGNs.

1.2.2 Coherent emission

Alternative models based on coherent synchrotron emission processes should allow brightness temperatures far in excess of the inverse Compton limit (Benford 1992, Benford and Lesch 1998). In incoherently emitting synchrotron sources, the circular polarization is usually relatively small (Legg and Westfold 1968), of the order of the $0.1 - 0.5\,\%$. In coherent emission processes, like synchrotron masers or synchrotron-cyclotron emission, one would expect appreciable circular polarization which is not observed in typical IDV sources. Larger circular polarization can be obtained in the interstellar medium (ISM) by Faraday conversion from linear to circular (Jones and O'dell 1977), or if the magnetic fields are highly ordered.

Recently, relatively strong circular polarization has been observed in quasars and BL Lacs objects, in particular the IDV source PKS 1519–273 showed intraday variations even in the circular polarized flux density. This phenomenon was explained by Macquart (2002) in terms of propagation effects.

1.3 Propagation through the Interstellar Medium: Refractive Interstellar Scintillation

The twinkling of star-light in a clear night is known since long time. This first example of scintillation is caused by the scattering of star light in the Earth's atmosphere. Similarly, for compact radio sources, the turbulence in the interstellar medium causes a change in the phase of the incoming radio waves: the paths of the waves are distorted producing spatial variations in the received flux density. The phenomenon of scintillation then occurs (fig. 1.3), since the turbulent medium is in motion with respect to the observer. Let us consider a thin layer in the ISM as a screen and assume that the

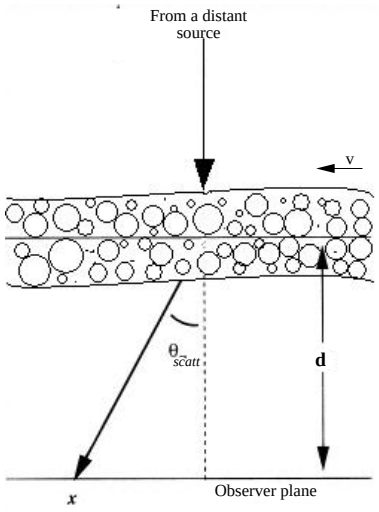

Figure 1.3: Schematic representation of scattering due to the interstellar medium.

radiation passing through it changes its phase. Equation 1.6, the so-called Fresnel-Kirchhoff equation, corresponds to the change in amplitude of the incoming wave, due to the screen, seen by an observer in its coordinate frame (X, Y) (Narayan 1992). The Fresnel-Kirchhoff equation contains the effects of a change in the phase $\phi(x, y)$ of an

incoming radio wave:

$$\Psi(X,Y) = \frac{e^{-i\pi/2}}{2\pi r_{\rm F}} \int\int \exp\left(i\phi(x,y) + i\frac{(x-X)^2+(y-Y)^2}{2\,r_{\rm F}}\right) dx\,dy \qquad (1.6)$$

$$r_{\rm F} = \sqrt{\frac{\lambda \cdot \mathrm{d}}{2\pi}} \qquad (1.7)$$

where we defined the Fresnel scale $r_{\rm F}$ for radiation, at the wavelength λ, scattered by a screen at distance d from the observer. In particular the second term in the exponential indicates the phase changes due to the path distortion from the point(x, y) to the point (X, Y). The amplitude modulation occurs within an angular scaleθ_{scatt} and the source scintillates only if its apparent size is smaller thanθ_{scatt}. The spatial scale that defines the strength of scintillation is called *diffractive scale*:

$$r_d = \frac{\lambda}{2\pi\,\theta_{scatt}} \qquad (1.8)$$

When $r_d > r_{\rm F}$, we refer to **weak (refractive) scattering**. From eq. 1.7 and eq. 1.8, it is possible to state that the weak scintillation is dominant at short radio wavelengths and small distances. In such regime the amplitude of the flux density varies "weakly" around its unscattered value due to the path distortion within$r_{\rm F}$. We define the typical temporal scale for weak scattering $t_{weak} \sim r_{\rm F}/v$, where v is the screen velocity seen by the observer.

The **strong scattering** regime occurs when $r_d < r_{\rm F}$. In this case, the dominant spatial scale is r_d but also the size of the scattering screen has to be taken into account. We define the *refractive scale* r_{refr} as the region in the screen generating the variations; this spatial scale corresponds to the angular sizeθ_{scatt}. Therefore, in the strong regime two different types of scintillation are considered: spatial scales fromr_d to r_{refr} imply "diffractive" scintillation and between r_{refr} and $r_{\rm F}$ the scintillation is "refractive". The corresponding time scales are: $t_d \sim r_d/v$ and $t_r \sim r_{refr}/v$.

Finally, we can describe the scintillation features of the extragalactic radio sources. Assuming a source angular size θ_{source}, the scattering size is:

diffractive: θ_{source} is smaller than the diffractive angular scale, $\theta_d = r_d/\mathrm{d}$.

refractive strong: $\theta_{source} \lesssim \theta_{scatt}$. Strong effects become less prominent if the source size is comparable to the scattering size. From eqs. 1.7 and 1.8, it follows: $\theta_{scatt} = \sqrt{\frac{\lambda}{2\pi \mathrm{d}}}$.

refractive weak: $\theta_{source} \gtrsim \theta_{scatt}$. We are in the regime of *quenched scattering*. The variations involved become smaller and they disappear for$\theta_{source} > \theta_{weak} = r_{\mathrm{F}}/\mathrm{d}$.

The angular sizes of the extra-galactic sources in the radio band are always larger than the diffractive angular size in our galaxy and so the diffractive scintillation is not present. On the other hand, (strong and weak) refractive interstellar scintillation (**RISS**) is present and it is responsible for flux density variations with time scales from weeks down to hours of flat-spectrum radio sources.
The polarization characteristics of IDV can also be described by interstellar scattering (Rickett et al. 1995, Qian et al. 2001): the superposition of two scintillation components with non-parallel $\vec{E}$ vectors can create modulation of the polarization and correlations (or anti-correlations) with the total flux density.
However, RISS theory cannot completely explain all the observations and a mixture of intrinsic and extrinsic effects may occur. In particular, scintillation cannot explain the quasi-periodicity observed in some sources and the broad-band correlations like the simultaneous variability in 0716+714 (fig. 1.2). Regarding the polarization, scintillation models can not yet explain the observed 180°-swings of the polarization angle.

1.3.1 Annual modulation

The apparent relative velocity between the orbital motion of the Earth and the scattering screen is modulated by the composition of the Earth's velocity vector and the velocity vector of the screen (Bondi et al. 1994): it results in a seasonal change of the time scale.
In detail, such *annual modulation* of the time scales is due to changes of the transverse velocity of the Earth across the scattering medium. The transverse velocity, the perpendicular component of the relative velocity of the scattering screen, consists of three components: the Earth's orbital motion $\vec{v}_{\oplus}$, the motion of the sun towards the solar Apex $\vec{v}_{\odot}$ and the motion of the scattering screen $\vec{v}_s$ with respect to the Local Standard

of Rest:

$$\vec{v} = \vec{v}_{\oplus} + \vec{v}_{\odot} + \vec{v}_s \tag{1.9}$$

the transverse velocity is: $v_{\perp} = v \cdot \sin\vartheta$, where ϑ is the angle between the velocity and the line of sight.

In September 1998, Kraus et al. (1999) found a dramatic slow down in the variability of 0917+624. Figure 1.4 (see Qian and Zhang 2001) shows the relative velocity of the Earth with respect to a screen in the direction of this quasar. The four curves in the picture 1.4 correspond to the different velocities assumed for the scattering screen. The change observed by Kraus et al. (1999) corresponds to the minimum around day 250–300 (September–October), but observations by Fuhrmann et al. (2002) demonstrated that 0917+624 was not variable for the following two years. Krichbaum et al. (2002) suggested that a blending with a possible new jet component recently ejected may be the reason for the "disappearance" of IDV in the radio core.

Notably, other sources located in the vicinity of 0917+624 (eg. 0716+714, 0954+658) so far did not show any sign of annual modulation in their variability pattern. If IDV would be solely due to interstellar scattering, this is hard to understand.

1.3.2 Very rapid IDV sources

Recently, very fast variable objects were discovered: PKS 0405–385 (Kedziora-Chudczer et al. 1997), J1819+385 (Dennett-Thorpe and de Bruyn 2000) and PKS 1257–326 (Bignall et al. 2002). These objects vary in amplitude up to 600% in the cm-regime on time scales of less than one hour. Different experiments indicated that the very fast variations in these extreme IDVs are caused by scintillation. In fact, all these objects showed the seasonal changes discussed above: in particular J1819+385 reproduced the predicted annual modulation during two consecutive years.

Simultaneous observations at 6 cm of PKS 0405-385 with the ATCA (Australian Telescope Compact Array, Australia) and VLA (Very Large Telescope, USA) showed a significant time lag between the arrival times of the variability patterns at the two telescopes (Jauncey et al. 2000). The IDV features arrived first at the VLA and 140 seconds later at the ATCA, this large time lag shows that the variations are not intrinsic to the source and they can only be explained by a scattering screen at a distance of few

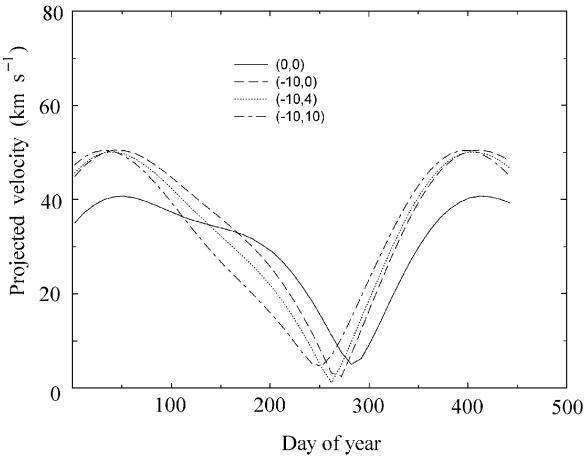

Figure 1.4: The relative velocity of the Earth in the direction of 0917+62. The three curves corresponds to the motion of the scattering medium in right ascension and declination: (v_m^α, v_m^δ). The solid line corresponds to a stationary screen, the dashed line to a velocity of -10 km/s in right ascension and 0 in declination, the dotted line to -10 km/s in α and 4 km/s in δ, and the dotted-dashed line to -10 km/s and 10 km/s in the directions α and δ, respectively.

tens of parsec.

The intrinsic brightness temperatures derived for these extreme IDV objects are$\sim 10^{15}$ and still violate the inverse Compton limits. Eqs. 1.3 and 1.4 are valid in the general case and it is possible to calculate the brightness temperature without using the light-travel argument 1.1. From the Lorentz transformation for the frequency ($\nu = D \cdot \nu_{int}$), it results:

$$T_b = D \cdot T_b^{int} \tag{1.10}$$

Due to the linear dependence of the T_b on the Doppler factor, one needs, for intrinsically variable sources, high Doppler factors ($D \sim 1000$) to avoid the violation of the inverse Compton limit and again one has to take beamed radiation very close to the line of sight and intrinsically active core into account, to describe the IDV characteristics of

these peculiar radio sources. However, the high brightness temperature problem can be avoid in a pure extrinsic interpretation of the extreme IDV requiring a scattering screen at distances in the range 3–30 pc (Rickett et al. 2002).

1.3.3 Microlensing

Gravitational lensing of quasars by an intermediate galaxy located near the line of sight is a well known phenomenon. However, such a general relativistic effect can also occur if one considers perturbations of the gravitational field due to single stars within galaxies (therefore *microlensing*). The amplification effect varies because of the relative velocity between the "lens" and the Earth: this leads to a flux density variability of the background object. Observational characteristics of intrinsic IDV and microlensing are similar and it is difficult to disentangle the two phenomena (Wambsganss and Kundic 1995). Moreover microlensing requires relativistic boosting and high intrinsic activity in the lensed object (i.e. the source must also intrinsically vary).

Subramanian and Gopal-Krishna (1991) proposed a model which combines superluminal motion and microlensing: the rapid variability is generated by the apparent faster-than-light motion of the knots, in the jets, relative to the stars of a foreground galaxy. Such superluminal microlensing could produce rapid and frequent outburst on even intrinsically non-variable radio sources.

Although microlensing effects could reproduce some observational characteristics of IDV, it is hard to believe that all the observed rapid variations are due to this phenomenon. In particular, microlensing is achromatic and can not reproduce the observed broad-band variability.

Part I

Observations and Data Reduction

Chapter 2

Data at cm-wavelengths

In this work, a complete statistical analysis of the rapid variability in AGNs was performed. We combined all the Effelsberg and VLA data of the IDV monitoring projects taken from 1985 up to 2000. In this chapter, the selection criteria of the complete sample of flat-spectrum radio sources is discussed. Then, observations and data reduction procedures of the data obtained at the Effelsberg radio telescope is described and a new set of data measured in March 2000 is presented.

2.1 The complete sample of flat-spectrum radio sources

The radio sources were selected from the 1 Jy catalogue (Kühr et al. 1981), which covers the whole sky except for the galactic plane region ($\mid b \mid < 10^\circ$) and the Magellanic clouds. This catalogue consists of 518 objects and, at 5 GHz, is complete with a flux density limit of 1 Jy. From the overall source list, the radio sources with declination higher than 50° were extracted (60 objects). Finally among these, we found 32 flat-spectrum[1] radio sources (tab. 2.1), which form our complete sample. In detail the sample consists of 18 quasars (QSO), 9 BL Lacs (BL), 3 galaxies (GAL) and 2 empty fields (EF). In galactic coordinates, these sources are distributed in the region defined by $10^\circ \leq b \leq 60^\circ$. Out of the complete sample, our IDV archive contains some additional measurements of interesting sources at various declinations and spectral indices (see bottom of table 2.1). These sources were chosen mainly since they are frequently observed at other telescopes and with VLBI.

Table 2.2 (center panel) summarizes the flux density monitoring projects carried out

[1] $\alpha < 0.5$, we use: $S \propto \nu^{-\alpha}$

with the 100-m radio telescope. Presentation and description of the data (since 1989 up to 1999) are given in Kraus et al. (2003). The March 2000 data are analyzed in this work. Furthermore, we used the data from Heeschen et al. (1987) (tab. 2.2, top panel) and the IDV monitoring data (tab. 2.2, bottom panel) obtained at the VLA (Very Large Array[2]) which are presented in Quirrenbach et al. (2000).

2.2 Effelsberg data

From 1985 to 2000, several monitoring projects of rapid variability in blazars were carried out using the 100-m Effelsberg radio telescope of the Max-Planck-Institut für Radioastronomie (Bonn). This instrument is able to pick up the radio emission in the frequency range between 408 MHz and 86 GHz using receivers in both primary and secondary (Gregory) focus.

Our archive contains flux density monitoring data of flat-spectrum radio sources at 11, 6, 2.8 and 0.9 cm (2.7, 4.85, 10.45 and 32 GHz, respectively), all these receivers are located in the secondary focus.

Here, a new set of observations at 2.8, 6, 11 cm, carried out from March 10th to 17th, 2000 during a radio-optical campaign (see section 5.4), is included: table 2.3 summarizes the observations and in appendix A the light curves of all the observed flat spectrum radio sources are shown. Observations of non-variable sources assured a reliable flux density calibration allowing to correct for instrumental and atmospheric effects. Besides the total power, linear polarization information was collected: the incoming radiation was split by a circular transducer in the left (LHC) and right (RHC) components of the polarization. These signals enter a polarimeter which provides as output the Stokes parameters I, Q, U (and V). The output of a receiver consists of four signals:

$$Sig_1 = S_{LHP} \cdot S_{LHP} \tag{2.1}$$

$$Sig_2 = S_{LHP} \cdot S_{RHP} \cdot \sin\Theta \tag{2.2}$$

$$Sig_3 = S_{LHP} \cdot S_{RHP} \cdot \cos\Theta \tag{2.3}$$

$$Sig_4 = S_{RHP} \cdot S_{RHP} \tag{2.4}$$

[2]A facility of the NRAO (National Radio Astronomy Observatory).

S_{LCP} is the signal in left-hand circular polarization, S_{RCP} is the right-hand polarized signal and Θ is the phase shift between these two component of the polarization. The total flux density is proportional to $Sig_1 + Sig_4$. Circular polarization could be measured as $V = Sig_1 - Sig_4$. In our sources it is typically $\leq 0.5\%$ and therefore neglected in this work.
At 0.9, 2.8 and 6 cm the *multi-beam* technique was used. The receivers consist of a main feed (which observes the source) and secondary feeds (pointing at the empty sky). In this way, it is possible to take into account and remove time variable effects due to the Earth atmosphere. The data reduction program (TOOLBOX) combines instantaneously the output of the different horns.

All the sources are point-like compared to the resolutions of the telescope at the different frequencies and were observed using the *cross-scan* technique: the telescope is driven in two orthogonal directions (usually azimuth and elevation) centered on the source position. Such cross scans are repeated various times to increase the integration time: the number of subscans depends on the weakness of the radio source. The signal-to-noise ratio increases with increasing integration time t_{int}:

$$\frac{\Delta T_{noise}}{T_{sys}} = \frac{K}{\sqrt{\Delta\nu\, t_{int}}} \tag{2.5}$$

where K is a constant that depends on the receiver system, ΔT_{noise} indicates the RMS fluctuations (that is the minimum noise uncertainty), T_{sys} the system temperature (that is the whole system noise) and $\Delta\nu$ is the bandwidth.

2.3 Data reduction and Calibration

2.3.1 Total Intensity

The data reduction was performed using CONT2, a task of the standard software package TOOLBOX of the MPIfR. For each subscan CONT2 adds the signals of eq. 2.1 and eq. 2.4 and calculates the respective error from the RMS of the signals. Finally, the program fits a Gaussian on the average of the subscans in the two directions. The amplitudes of the Gaussian fits are proportional to the observed flux densities in azimuth and elevation. Such fits may be not exactly centered to the zero position, e.g. because

of gravity effects which change the dish shape. The 100-m Effelsberg radio telescope is built following the principle of homology that allows the reflecting structure to deform into a new paraboloid with a slightly different focal point. It is then only necessary to move the secondary reflector to maintain optimal performance. A paraboloid shape allows to correct for the off-sets in the pointing using the following formulae:

$$S_{elv}^{true} = S_{elv}^{obs} \cdot \exp\left(4 \ln 2 \frac{(\mathrm{COL}^*)^2}{\theta_{azi}^2}\right) \tag{2.6}$$

$$S_{azi}^{true} = S_{azi}^{obs} \cdot \exp\left(4 \ln 2 \frac{(\mathrm{NulE})^2}{\theta_{elv}^2}\right). \tag{2.7}$$

COL* and NulE are the pointing corrections and θ_x ($x = azi$ or elv) is the measured HPBW in the "x" direction (note the cross correction between azimuth and elevation). After the pointing adjustments, the azimuth and elevation Gaussian fits are averaged. Another important correction to consider is how the telescope efficiency varies at different elevations. In this case, frequent observations of primary and secondary calibrators (i.e. steep-spectrum radio sources) are used to build the gain curve of the telescope. Such a gain correction curve consists of a polynomial fit of the normalized flux densities of the calibrators as a function of the elevation.

Finally, relatively long term variations due to atmospheric or systematic time-dependent effects are corrected by comparison with the secondary calibrators. The duty cycle of these calibrators is the same as for our program sources: a calibrator is always observed after an IDV candidate. In this way, systematic effects can be recognized and removed. The resulting value for the flux density should now be correct but it is still expressed in telescope units. An absolute flux density scale (Baars et al. 1977, Ott et al. 1994) is used to calculate the actual flux density of primary calibrators (eg. 3C286, NGC7027):

$$\log S[\mathrm{Jy}] = a + b \log \nu[\mathrm{MHz}] + c \log^2 \nu[\mathrm{MHz}] \tag{2.8}$$

where a, b, c are coefficients given in Baars et al. (1977) at the observing frequency ν. The scaling factor is the ratio between the calculated value and the average of the observed ones. Finally, all the measurements of our sources are multiplied by this factor.

The scattering of the non-variable sources is an indication of the achieved measurement accuracy and it is taken into account for the estimate of the final uncertainties that lie

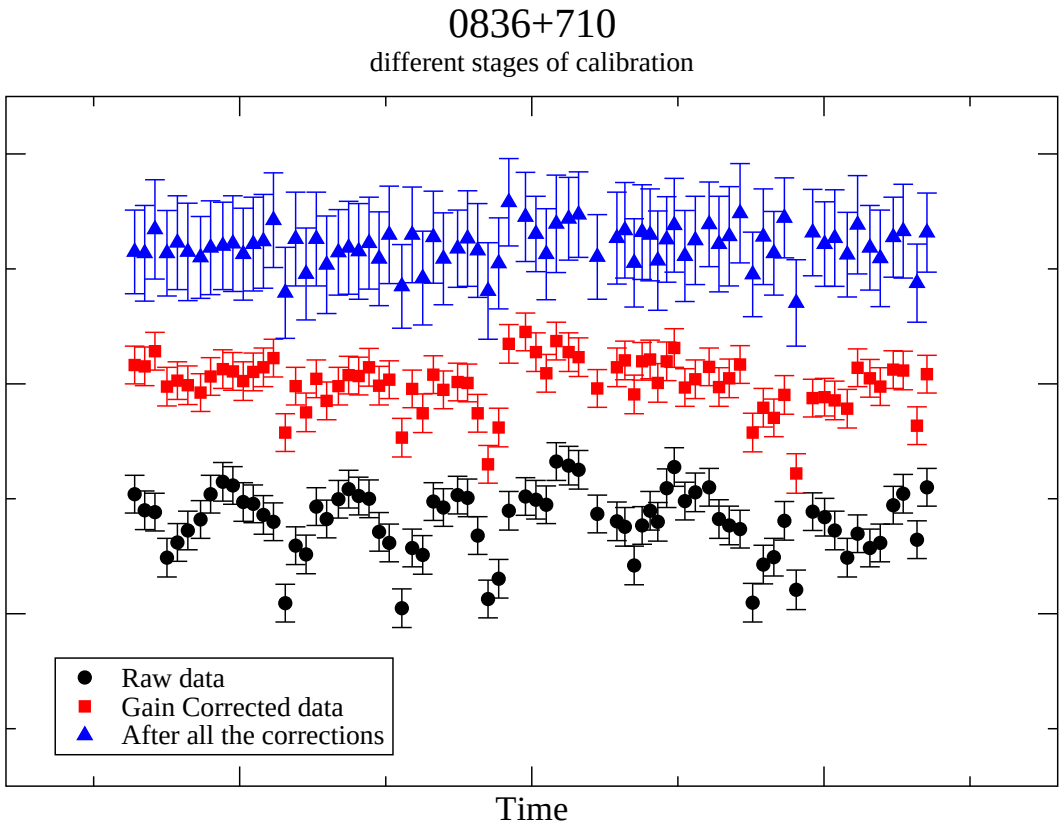

Figure 2.1: Importance of secondary calibrators. *Circles:* Normalized flux density measurements of 0816+710 without any correction. *Squares:* 0816+710 after the gain curve application. *Triangles:* Final values corrected for the time dependent effects. The errors take into account the RMS fluctuations of all the calibrators. For plotting convenience, the light curves are shifted by arbitrary values.

in the range of $0.5-1\,\%$ of the total flux density. As example, figure 2.1 shows the "light curves" of 0836+710, used in March 2000 as secondary calibrator, at different stages of the calibration process. One should note that the final light curve has larger errors. This is due to the fact that we propagate the formal measurement uncertainties with the values of RMS of the non-variable objects to have an indication of the remaining systematic errors on the variability.

2.3.2 Polarization

Regarding the polarized signal, the data reduction software CONT2 works with eq. 2.2 and eq. 2.3 since they are related to the Stokes parameter Q and U:

$$Q = 2 \cdot Sig_2 \tag{2.9}$$

$$U = 2 \cdot Sig_3 \tag{2.10}$$

The CONT2 output for the polarization includes the intrinsic polarization of the object and other effects like the instrumental polarization, "*cross talk*", and the parallactic angle (eq. 2.15). Following the Turlo et al. (1985) analysis for linear polarization, it is possible to determine the influence of the instrumental polarization during astronomical observations:

The intrinsic polarization can be described by the vector $\mathbf{S^{true}}$(I,Q,U) (again we neglect V) and what one measures is $\mathbf{S^{obs}}$(I,Q,U), that is the observed polarization containing the intrinsic one and the *cross talk*. The relationship between these vectors is:

$$\mathbf{S}^{obs}(I,Q,U) = \mathbf{M} \cdot \mathbf{S}^{true}(I,Q,U) \tag{2.11}$$

where $\mathbf{M}$ is the 3×3 *Müller* matrix. We can decompose $\mathbf{M}$ into two parts, $\mathbf{M} = \mathbf{T} \cdot \mathbf{P}$. The $\mathbf{T}$ matrix contains only information about the instrumental polarization and $\mathbf{P}$ takes into account the time dependent polarization variations due to parallactic angle ($P.A.$) changes:

$$\mathbf{P} = \begin{pmatrix} 1 & 0 & 0 \\ 0 & \cos 2 \cdot P.A. & -\sin 2 \cdot P.A. \\ 0 & \sin 2 \cdot P.A. & \cos 2 \cdot P.A. \end{pmatrix}. \tag{2.12}$$

Due to the Earth rotation, the sources cover a circle in the sky (described by the parallactic angle) and the polarization vectors change their orientation. In particular the polarization angle:

$$\chi = 0.5 \cdot \arctan\left(\frac{U}{Q}\right) \tag{2.13}$$

becomes:

$$\chi^{true} = \chi^{obs} + P.A. - \tilde{\gamma} \tag{2.14}$$

where $\tilde{\gamma}$ is the directional coupler angle of the noise diode, used for the receiver calibration, and the parallactic angle. It is:

$$P.A. = \arctan\left(\pm\frac{\cos(Lat)\sin(\Delta h)}{sin(Lat)\cos(\delta) - \cos(Lat)\sin(\delta)\cos(\Delta h)}\right) \tag{2.15}$$

where Δh is the hour angle, δ the declination of the source and Lat is the latitude of the radio telescope (for the 100-m Effelsberg radio telescope: $Lat = 50\,^\circ 31\,' 30\,''$). The argument of the arctangent is positive when $0 < \Delta h < 12$ and negative for $12 < \Delta h < 24$. From a linear independent set of observations of known calibrators, it is possible to

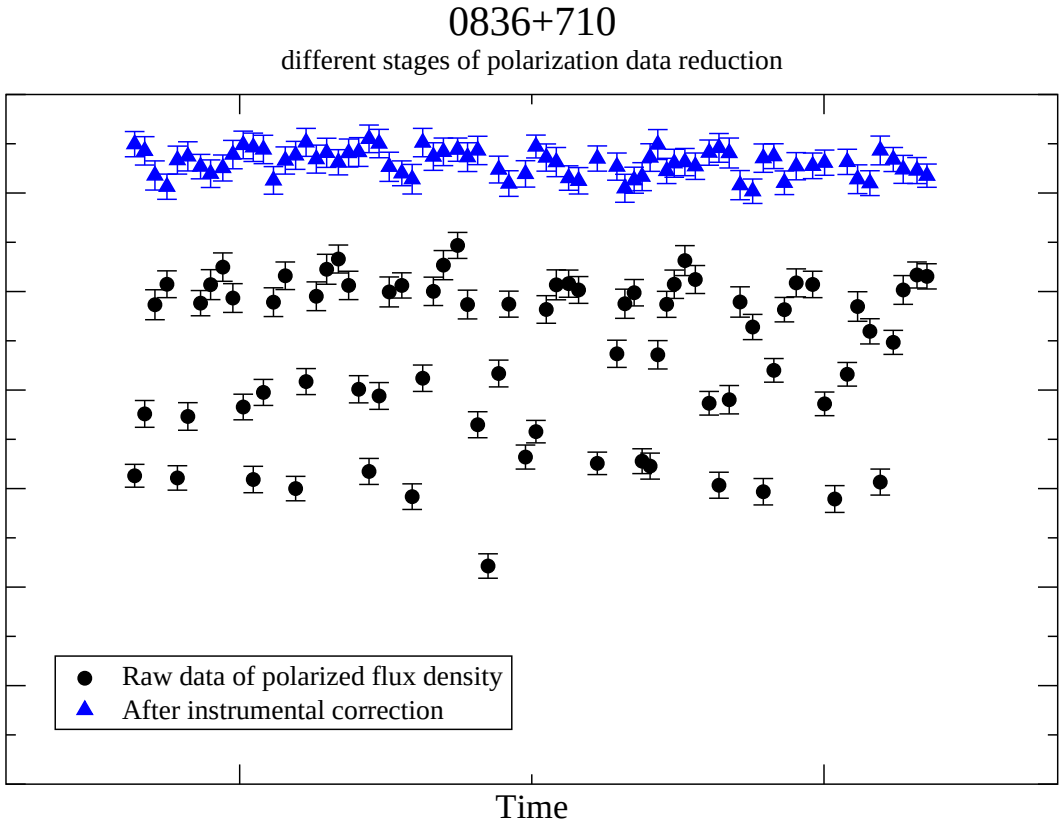

Figure 2.2: Importance of the secondary calibrators in the data reduction of polarization. *Circles:* Polarized flux density measurements of 0816+710 without any calibration. *Triangles:* This light curve is the result of corrections. For plotting convenience, the light curves are shifted of arbitrary values.

derive the elements of $\mathbf{M}$. Inverting the Müller matrix, one can calculate the true polarization vector of the observed source using at least three observations. To obtain a better fit, different sources were used: non-variable sources with well defined polarization (eg. 3C286 and 0836+710) and unpolarized objects such as 0951+699. The unknown coefficients of the linear system given by the equation $\mathbf{S^{obs}} = \mathbf{T} \cdot \mathbf{P} \cdot \mathbf{S^{true}}$ are determined by least-square fits on the observed values, that is the matrix $\mathbf{S^{obs}}$. Following such procedures it is possible to reach an accuracy for the linear polarization of $< 5\,\%$ and for the polarization angle $< 5^\circ$. Figure 2.2 shows as an example the polarization raw data and the corrected polarized flux densities.

Name	b_{II}	ID	z	$\alpha_{11/6}$	Type
0016+73	+10.7	QSO	1.781	-0.16	I
0153+74	+12.4	QSO	2.338	0.32	0
0212+73	+12.0	BL	2.367	0.12	0
0454+84	+24.7	BL	0.122	-0.38	II
0602+67	+20.9	EF	-	-0.39	II
0615+82	+26.0	QSO	0.710	0.03	0
0716+71	+28.0	BL	-	-0.21	II
0723+67	+28.4	QSO	0.846	0.33	0
0831+55	+36.6	GAL	0.241	0.46	0
0833+58	+36.6	QSO	2.101	-1.31	0
0836+71	+34.4	QSO	2.172	0.33	0
0850+58	+38.9	QSO	1.322	-0.78	II
0917+62	+41.0	QSO	1.446	-0.25	0
0945+66	+41.9	EF	-	0.46	0
0954+55	+47.9	QSO	0.901	0.12	0
0954+65	+43.1	BL	0.367	-0.25	II
1031+56	+51.9	QSO	0.459	0.31	0
1039+81	+34.7	QSO	1.254	-0.40	II
1150+81	+35.8	QSO	1.250	0.09	I
1418+54	+58.3	BL	0.152	-0.24	II
1435+63	+49.7	QSO	2.068	0.23	I
1637+57	+40.4	QSO	0.750	-0.56	II
1642+69	+36.6	QSO	0.751	0.26	II
1739+52	+31.7	QSO	1.379	-0.07	II
1749+70	+30.7	BL	0.770	0.33	I
1803+78	+29.1	BL	0.684	-0.26	I
1807+69	+29.2	GAL	0.051	0.35	II
1823+56	+26.1	BL	0.664	-0.17	I
1928+73	+23.5	QSO	0.302	0.01	0
1954+51	+11.8	QSO	1.230	0.14	II
2007+77	+22.7	BL	0.342	-0.67	I
2021+61	+13.8	GAL	0.227	-0.10	0
0235+16	-39.1	BL	0.851	1.09	II
0804+49	+42.1	QSO	1.433	-.67	II
0828+49	+32.6	BL/QSO	0.548	.46	II
1458+71	+59.9	QSO	0.905	.18	0
1504+37	+36.4	GAL	0.674	-.06	II
2200+42	−10.4	BL/GAL	0.069	-.19	II

Table 2.1: List of the complete sample: flat-spectrum sources at high declination ($\delta > 50^\circ$). We also show: the galactic latitudes, optical identifications, known redshifts (Stickel et al. 1994) and the spectral indices evaluated between 11 and 6 cm (Kühr et al. 1981). The last 6 sources do not belong to the complete sample but were as well observed and analyzed in this work. *Last column*: IDV type (at 6 cm) from observations (see section 3.2).

Date	N	Frequencies [GHz]				
04/05/1985 – 06/05/1985	8	2.70*				
15/08/1985 – 19/08/1985	15	2.70*				
27/12/1985 – 31/12/1985	15	2.70*				
22/12/1989 – 29/12/1989	6		4.75		10.55	
31/07/1990 – 03/08/1990	8	2.70	4.75			
17/05/1991 – 24/05/1991	11	2.70	4.75			
27/12/1991 – 03/01/1992	10	2.70*	4.75*		10.55*	
10/04/1993 – 13/04/1993	3		4.75			
18/06/1993 – 20/06/1993	4		4.75			
01/09/1995 – 08/09/1995	4	2.70	4.85			
05/12/1997 – 08/12/1997	4		4.85		10.45	
25/12/1997 – 31/12/1997	9	2.70	4.85		10.45	
17/09/1998 – 22/09/1998	5		4.85		10.45	32*
08/02/1999 – 14/02/1999	5		4.85			
10/03/2000 – 17/03/2000	9	2.70	4.85		10.45	
04/05/1989 – 09/05/1989	9	1.49	4.86	8.44	15.0	
29/01/1990 – 23/02/1990	3	1.49*	4.86*	8.44*	15.0*	
02/10/1992 – 23/10/1992	9	1.49*	4.86*	8.44*		

Table 2.2: Summary of all IDV experiments carried out since 1985. The " * " indicates the lack of polarization information at that frequency due to bad weather conditions or technical problems. N is the number of flat-spectrum sources observed. The data in the top panel are discussed in Heeschen et al. (1987). The center panel shows the Effelsberg data presented in Kraus et al. (2003) plus the March 2000 experiment discussed in this work. The bottom panel shows the VLA monitoring experiments, which are discussed in Quirrenbach et al. (2000).

$\lambda = 11\,\mathrm{cm}$		**TOT**		$m_0 = 0.51\,\%$			
Source	N	S[Jy]	Δ_S	m[%]	Y[%]	χ^2_r	type
0716+71	74	0.738	0.021	2.87	8.47	35.443	II
0836+71	74	2.698	0.014	0.51	0.00	1.309	0
0917+62	36	1.460	0.020	1.35	3.74	8.930	I
0954+65	91	0.473	0.020	4.13	12.31	54.357	0
1150+81	28	1.735	0.015	0.88	2.16	3.888	0
1749+70	26	0.684	0.006	0.91	2.26	3.407	0
1803+78	36	2.495	0.059	2.36	6.92	28.338	I
3C309.1	37	5.038	0.018	0.37	0.00	0.693	0

$\lambda = 6\,\mathrm{cm}$		**TOT**		$m_0 = 0.42\,\%$			
Source	N	S[Jy]	Δ_S	m[%]	Y[%]	χ^2_r	type
0716+71	73	0.721	0.014	1.96	5.76	4.728	II
0836+71	73	2.397	0.010	.42	0.13	0.192	0
0917+62	35	1.515	0.011	.70	1.70	0.604	0
0954+65	90	0.595	0.015	2.58	7.64	8.812	II
1150+81	28	1.548	0.008	.50	0.80	0.322	0
1749+70	27	0.630	0.004	.69	1.65	0.513	0
1803+78	35	2.728	0.043	1.59	4.61	3.216	I
3C309.1	36	3.646	0.012	.33	0.00	0.139	0

$\lambda = 2.8\,\mathrm{cm}$		**TOT**		$m_0 = 0.75\,\%$			
Source	N	S[Jy]	Δ_S	m[%]	Y[%]	χ^2_r	type
0716+71	58	0.850	0.016	1.92	5.32	0.984	II
0836+71	61	2.329	0.017	0.75	0.00	0.154	0
0917+62	28	1.362	0.017	1.24	2.95	0.409	I
0954+65	67	0.690	0.013	1.94	5.35	1.023	II
1150+81	23	1.271	0.015	1.21	2.85	0.393	0
1749+70	22	0.563	0.010	1.83	5.02	0.819	I
1803+78	31	2.795	0.037	1.32	3.27	0.470	I
3C309.1	30	2.419	0.029	1.19	2.76	0.377	0

Table 2.3: Observations in March 2000. $\lambda = 11\,\mathrm{cm}$,6 cm, 2.8 cm: Total intensity. The columns correspond to source name, number of data points, mean flux density and its error, the modulation index (see section 3.1 eq. 3.1), the variability amplitude (see section 3.1 eq. 3.4), the reduced χ^2 (see section 3.1 eq. 3.3) and the variability type (see section 3.2).

$\lambda = 11\,\mathrm{cm}$		**POL**		$m_{\mathrm{P},0} = 1.07\,\%$			$\sigma_{\chi,0} = 0.19\,^\circ$		
Source	N	P[Jy]	Δ_{P}	$\mathrm{m}_{\mathrm{P}[\%]}$	$\mathrm{Y}_{\mathrm{P}[\%]}$	$\chi^2_r(\mathrm{P})$	$\chi[^\circ]$	Δ_χ	$\chi^2_r(\chi)$
0716+71	74	.0285	.0044	15.47	46.29	9.169	-7.16	5.37	21.034
0836+71	74	.2131	.0067	3.16	8.93	8.338	100.72	.91	23.611
0917+62	37	.0480	.0027	5.59	16.47	6.170	32.31	2.62	9.725
0954+65	91	.0248	.0030	11.94	35.69	4.221	11.44	6.42	21.470
1150+81	28	.0406	.0034	8.38	24.93	7.689	118.56	2.89	6.595
1749+70	26	.0086	.0021	24.23	72.62	2.360	86.17	24.93	27.610
1803+78	36	.1331	.0064	4.81	14.08	32.200	46.06	1.55	19.806
3C309.1	37	.1848	.0025	1.36	2.52	2.625	102.59	1.33	19.872

$\lambda = 6\,\mathrm{cm}$		**POL**		$m_{\mathrm{P},0} = 1.06\,\%$			$\sigma_{\chi,0} = 0.35\,^\circ$		
Source	N	P[Jy]	Δ_{P}	$\mathrm{m}_{\mathrm{P}[\%]}$	$\mathrm{Y}_{\mathrm{P}[\%]}$	$\chi^2_r(\mathrm{P})$	$\chi[^\circ]$	Δ_χ	$\chi^2_r(\chi)$
0716+71	73	.0202	.0021	10.67	31.84	111.145	6.00	6.46	781.451
0836+71	73	.1689	.0030	1.77	4.27	82.491	105.34	1.46	261.217
0917+62	35	.0628	.0017	2.78	7.70	124.571	32.85	1.23	134.481
0954+65	89	.0188	.0023	12.02	35.92	461.670	41.63	3.22	165.226
1150+81	28	.0466	.0011	2.31	6.17	28.799	77.99	3.28	434.723
1749+70	27	.0090	.0008	9.24	27.52	10.441	86.72	12.38	67.963
1803+78	35	.1561	.0590	37.77	113.27	*******	90.82	8.28	*******
3C309.1	37	.0906	.0023	2.51	6.83	97.988	67.81	1.83	193.704

$\lambda = 2.8\,\mathrm{cm}$		**POL**		$m_{\mathrm{P},0} = 2.64\,\%$			$\sigma_{\chi,0} = 0.21\,^\circ$		
Source	N	P[Jy]	Δ_{P}	$\mathrm{m}_{\mathrm{P}[\%]}$	$\mathrm{Y}_{\mathrm{P}[\%]}$	$\chi^2_r(\mathrm{P})$	$\chi[^\circ]$	Δ_χ	$\chi^2_r(\chi)$
0716+71	58	.0207	.0028	13.60	40.04	11.334	18.61	9.55	338.708
0836+71	61	.1079	.0056	5.19	13.41	26.880	113.16	3.23	47.451
0917+62	28	.0496	.0025	5.11	13.13	10.201	36.37	1.47	10.488
0954+65	67	.0062	.0077	124.30	372.80	40.791	30.73	26.28	120.815
1150+81	23	.0217	.0021	9.80	28.30	5.775	78.67	2.48	10.582
1749+70	22	.0092	.0019	20.88	62.14	5.336	83.42	7.63	13.469
1803+78	31	.1945	.0094	4.86	12.23	84.803	109.60	1.30	98.371
3C309.1	30	.0381	.0035	9.30	26.75	13.153	45.61	2.90	12.274

Table 2.4: Observations in March 2000. $\lambda = 11\,\mathrm{cm}$, 6 cm, 2.8 cm: Polarization. The columns correspond to source name, number of data points, mean polarized flux density P and its error, the modulation index of P (see section 3.1.1 eq. 3.5), the variability amplitude for P (see section 3.1.1 eq. 3.6), the reduced χ^2 for the polarized flux density (see section 3.1 eq. 3.3), the mean polarization angle χ, the standard deviation of χ and the reduced χ^2 for the polarization angle.

Part II

Data analysis

Chapter 3

Mathematical methods

For a quantitative description of the characteristics of variability, a time series analysis of the measured data points was performed. In this chapter, useful definitions for the data analysis and the mathematical instruments are summarized.

3.1 Modulation Index and Variability Amplitude

First of all, it is important to quantify the amount of variability in a light curve. Heeschen et al. (1987) developed some useful instruments and tests to describe the rapid variability in extragalactic radio sources. Here we follow their work introducing the most important details.

We define the *modulation index*, m, which provides the most direct indication of the variability characteristics of a source at a given frequency:

$$m[\%] = 100 \cdot \frac{\sigma_S}{< S >} \tag{3.1}$$

where $< S >$ is the flux density averaged over time and σ_S is the standard deviation of the flux density variations. It is measured from the data and can be related to theoretical models (see section 5.2). The modulation index depends on the measurement accuracy during the observations. A high m can be due to large measurement uncertainties. However, m alone is not the final proof for the existence of variability since the errors of the measurements of S are ignored. A χ^2-test is used to verify the hypothesis of variability. For each source, we test the hypothesis that the flux density remains constant during the observing period and is equal to the average of the

measured values. In this way, it results:

$$\chi^2 = \sum_{i=1}^{N} \left(\frac{S_i - < S >}{\delta S_i} \right)^2 \tag{3.2}$$

$$\chi^2_r = \frac{1}{N-1} \chi^2 \tag{3.3}$$

where χ^2_r is the reduced value of χ^2, N is the number of observations, S_i are the measured flux densities and δS_i the respective errors. Finally, the sources are considered variable, if the probability of the flux density to be constant is $\leq 0.1\%$.

It is useful to define the *variability amplitude*, Y, a noise-corrected parameter that describes the amount of variations in a light curve. The variability amplitude is given by:

$$Y[\%] = 3\sqrt{m^2 - m_0^2} \tag{3.4}$$

where m_0 is the mean modulation index of the non-variable sources and is a measure of the calibration accuracy. The variability amplitude indicates the level of the variations independently from the measurement uncertainty, which is contained in the modulation index of the calibrators. The variability amplitude is important to compare observations carried out at different epochs and frequencies. The multiplying factor of 3 is arbitrary and it is used for consistency with the original definition by Heeschen et al. (1987). In particular, this factor makes the variability amplitude of the same order as the observed peak-to-peak magnitude of the variations. The value of Y for the non-variable sources is set to zero.

3.1.1 Polarization

In the data reduction process, we measure the Stokes parameters Q and U (and their respective errors), which define the linear polarization features of the radiation. However, the quantities P (polarized flux density), and χ (polarization angle) are more relevant for a description of the variations. Similar to the total intensity discussion, we define modulation index and variability amplitude for the polarized intensity:

$$m_{\mathrm{P}}[\%] = 100 \cdot \frac{\sigma_{\mathrm{P}}}{< \mathrm{P} >} \tag{3.5}$$

$$Y_{\mathrm{P}}[\%] = 3\sqrt{m_{\mathrm{P}}^2 - m_{\mathrm{P},0}^2} \tag{3.6}$$

and for the polarization angle:

$$m_\chi[^\circ] = \sigma_\chi \tag{3.7}$$

$$Y_\chi[^\circ] = 3\sqrt{\sigma_\chi^2 - \sigma_{\chi,0}^2}. \tag{3.8}$$

As described in the section 2.3.2, observations of non-variable sources are necessary to calibrate the polarization data which are very sensitive to systematic effects. Furthermore, the secondary calibrators were used to set the noise level of the polarization variations: $m_{\mathrm{P},0}$ and $\sigma_{\chi,0}$.
Again, the χ^2 hypothesis test was used to identify the variability in polarization with a level of confidence equal to 99.9%.

3.1.2 Discussion of the uncertainty for the modulation index

An important point to discuss is the evaluation of the error for the modulation index, which consists of the measurement uncertainties and the statistical errors due to the occurrence of a stochastic event.
The error of the mean flux density, $\delta < S >$, is the contribution to the m uncertainty and takes into account the measurement accuracy. However, variations in the flux density are a stochastic process observed within a finite periodT_{tot} with a characteristic time scale t_{var}. Therefore, the error on a number n of independent variations during the observing period has to be taken into account for the overall uncertainty on the variability. Such number corresponds to:

$$n = \frac{T_{tot}}{t_{var}} \tag{3.9}$$

and its error is:

$$\delta n = 0.85\frac{1}{\sqrt{n}} \tag{3.10}$$

the factor 0.85 comes from the analytic solution of this statistical problem as it is described in Jenkins and Watts (1969).
But the question is how to properly identify the time scalet_{var}: if n takes into account the possible lack of variations in the stochastic process because of a limited observing period, one should also consider the variations on time scales below the sampling time.

In principle the data could show variations on a point by point basis. It is possible to have a significant variation at least within three data points which is more conservative than the limit set by Nyquist theorem for two data points. In this case, we can have:

$$\tilde{n} = \frac{T_{tot}}{3 < t_s >} \tag{3.11}$$

$$\delta\tilde{n} = \frac{1}{\tilde{n}} \tag{3.12}$$

where $< t_s >$ is the mean sampling interval.
The final errors for the modulation index used in this work were evaluated as propagation of the independent errors δn, $\delta\tilde{n}$ and $\delta < S >$.

3.2 Structure Function

The temporal structure of the variability in a data set can be studied in a mathematical way using *Structure Function* (SF) analysis. Following the definition of Rutman 1978, we write the first increment[1] of a random process (in our case the flux density variations $S(t)$ in the light curve of a compact flat-spectrum radio source) as:

$$\Delta S(t,\tau) = S(t+\tau) - S(t) \tag{3.13}$$

were τ is the time lag and $S(t)$ is the flux density at the time t. By definition, the first order structure function is the average over the time of the square of the first increment:

$$SF(\tau) =< (S(t) - S(t+\tau))^2 >_t \tag{3.14}$$

At $\tau \to 0$, the structure function yields to the noise level of the measurements. For $\tau \gg T^*$, where T^* is the largest correlation time scale in the data, the structure function is proportional to the variance of the variations, i.e. to the square of the modulation index: $SF(\tau \gg T^*) = 2\sigma_S^2 \propto m^2$. For shorter time lags, the structure function has a dependence on τ with a power law less than or equal to 2 (Rutman (1978)). The changes

[1]For the Mth-order increment, we have:

$$\Delta^{(M)} g(t,\tau) = \sum_{k=0}^{M} (-1)^k \begin{pmatrix} M \\ k \end{pmatrix} S(t + (M-k)\tau)$$

in such dependence are related to the periodicity and time scales of the variations in a time series: a maximum in the SF reflects the typical time scale of the variations while the presence of periodicity in our data produces minima in the structure function.

The different types of intraday variability are defined according to the shape of the structure function. Following Heeschen et al. (1987) we define three IDV classes:
A monotonic increase in the SF defines a **Type I** source, that is a long-term variable. In fact the lack of a maximum in the SF indicates that it is not possible to define a typical time scale during the observing period and in this case the source is variable with a time scale larger than the observing period. A maximum implies that fast variations are present (**Type II**) with a time scale defined by the time lag in the structure function, by definition (Wagner and Witzel 1995) an intraday variable source reaches such maximum within two days. **Type 0** denotes the non-variable sources and the SF is constant and dominated by the noise. The last column of table 2.1 indicates the IDV types (at 6 cm) in our sample. Figure 3.1 (*left*) shows the structure function for some radio sources observed in March 2000 at 6 cm. 0716+714 is a prototype of a type II object. In this case, the SF increases and reaches a maximum before the two days limit (vertical dashed line). For an IDV source, the typical time scale corresponds to a time lag close to the maximum in the SF (5.3). In the case of 1803+784 (type I), we note a monotonic increase of the SF without a well-defined maximum. Finally the structure function of 0836+710 is flat as expected for a secondary calibrator.

3.3 Other instruments for the time series analysis: Autocorrelation function, Power Spectrum and Cross-Correlation function

In the data analysis process, *autocorrelation function*, *power spectra* and *cross-correlation functions* were used to obtain further quantitative measurements from the time series.

An instrument for the time series analysis is the autocorrelation function (Edelson and Krolik 1988):

$$\rho(\tau) =< (S(t) \cdot S(t-\tau)) >_t \tag{3.15}$$

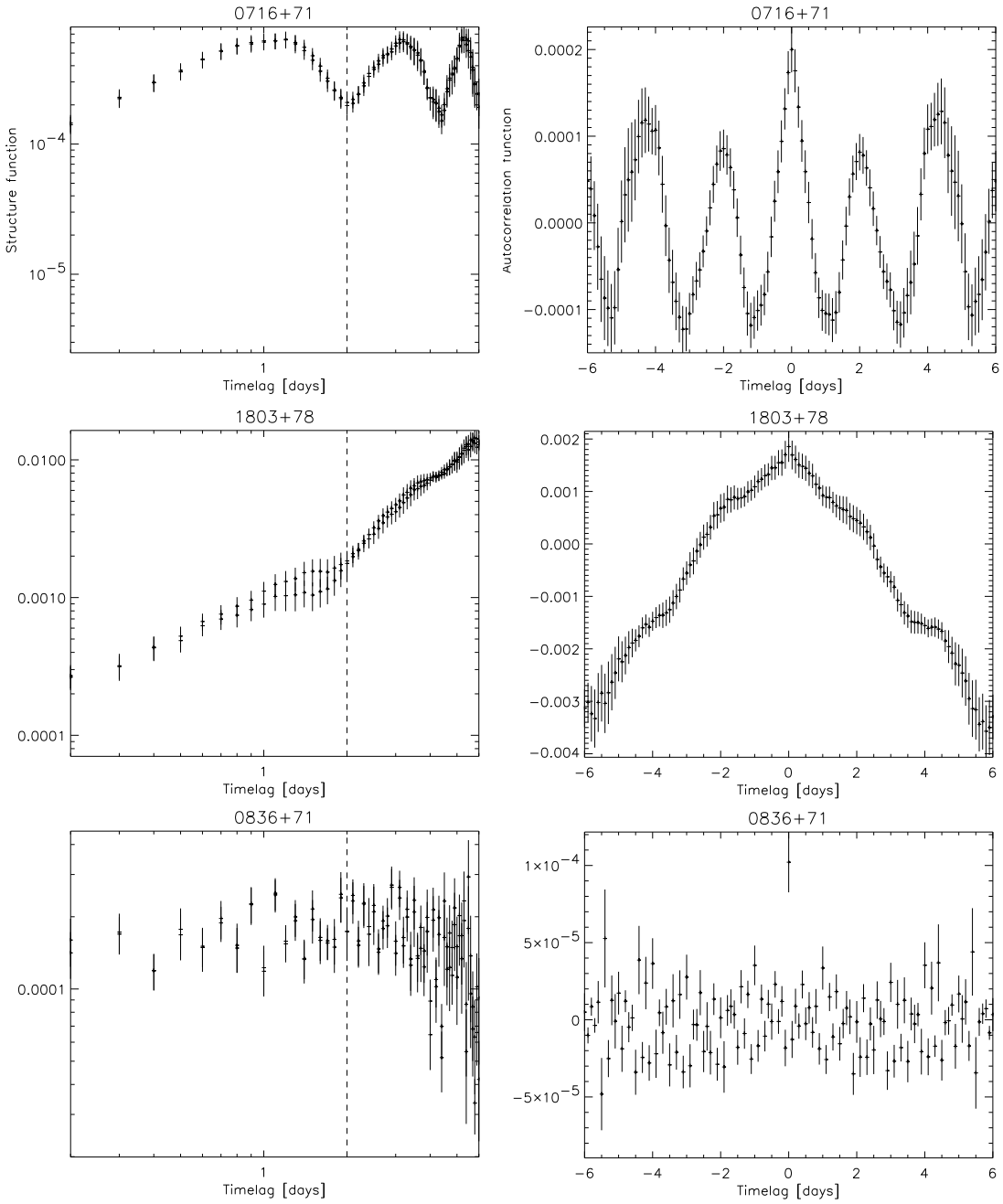

Figure 3.1: The structure functions are plotted on the *left* side of this figure. On the *right*, the autocorrelation functions are showed. The three sources plotted represent the different kinds of IDV. *Top:* type II, *center:* type I and *bottom* type 0. Measurements carried out in March 2000 at 6 cm.

As for the SF, ρ provides quantitative information about the periodicity and the typical time scales in a light curve (fig. 3.1 *right*). In particular, the square of the modulation index corresponds to the autocorrelation function at zero time lag: $m^2 = \rho(\tau \to 0)$.

The structure function and the autocorrelation function are related by the formula:

$$\mathrm{SF}(\tau) = 2[\rho(0) - \rho(\tau)] \tag{3.16}$$

which is not valid for $\tau = 0$ (because we do not deal with ideal data and for $\tau = 0$, as we have seen above, the SF corresponds to the noise). For large τ the autocorrelation is close to zero: that proves $\mathrm{SF}(\tau \gg T^*) = 2\rho(0) = 2m^2$ (see above).

The power spectrum is the square modulus of the Fourier transformation of the data:

$$\mathcal{P}S = |\mathrm{FT}[S(t)]|^2 \tag{3.17}$$

The power spectrum analysis is applied to time series in order to detect periodicities (or quasi-periodicities) by the presence of significant peaks at various frequencies ($\tilde{\nu}$). A peak in the power spectrum corresponds to a characteristic time ($t \overset{\mathrm{FT}}{\longmapsto} \tilde{\nu}$), but each spectrum contains also several other peaks which are produced by the irregular and not equidistant sampling of the data. In the software used here, a CLEAN algorithm is used to remove alias peaks in the power spectrum, which are caused by the irregular time sampling (Roberts et al. 1987 and Högbom 1974).
In this work, the power spectrum is only used as a cross-check for the time series analysis performed with the structure function. For a given $S(t)$ both methods should yield similar variability time scales.

In some cases, it is important to check whether two data sets are correlated with each other with (or without) a certain time lag. The cross-correlation function gives an indication on the correlation degree between two time series, $X(t)$ and $Y(t)$. The mathematical definition of the cross-correlation function is:

$$\mathrm{CCF}_{X,Y}(\tau) = < X(t+\tau) \cdot Y(t) >_t \tag{3.18}$$

We immediately note that the CCF becomes the autocorrelation function in the particular case of $X(t) = Y(t)$. An application of CCF is to check for correlation between polarization and total intensity or between data at different frequencies (see chapter 4).

Part III

Results

Chapter 4

Statistics

From the comparison of recent measurements with similar previous data (eg. Quirrenbach et al. 1992), one immediately sees that some objects changed IDV characteristics. However about one third of the sources in our complete sample showed variations of type II at least once and an overall two thirds can be considered variable (type I or type II). Such findings are largely consistent with previous analysis (Heeschen et al. 1987, Quirrenbach et al. 1992).
In this chapter, we perform a complete statistical analysis combining the new data (March 2000) with our previous measurements at the 100-m radio telescope and at VLA (Heeschen et al. 1987, Quirrenbach et al. 1992, Quirrenbach et al. 2000 and Kraus et al. 2003) as described in section 2.1. Finally we compare the results with the competing models for IDV.

4.1 Galactic dependences of the IDV phenomenon

It is important to verify the correlations between modulation indices of rapid variable sources and observable parameters strictly related to our Galaxy. From studies on the Dispersion Measures of Pulsars (Nordgren et al. 1992) the scattering medium is distributed in the Galaxy with a well defined latitude dependence: we expect that the concentration of the ionized gas increases as one gets closer to the galactic plane.
Following the refractive interstellar scintillation theory, Shapirovskaya and Larchenkova (1995) noted that one should observe a strong correlation between the modulation index of the intraday variable sources and the galactic latitude. These authors tried to calculate the distribution of the modulation indices along the galactic latitude b,

using data from different samples in a wide range of frequencies (from 80 MHz to 37 GHz). Their work is a statistical analysis that is based on long term variability: i.e. low frequency variability and "flickering" (Heeschen 1984). They conclude that a clear correlation is present but still not in agreement with the predicted correlation from the RISS theory ($m \propto \frac{1}{\sqrt{\sin(b)}}$). However, Shapirovskaya and Larchenkova (1995) used in their study, together with other data, the 6 cm sample observed and analyzed in Quirrenbach et al. (1992), who show that it is difficult to find a clear correlation between m and b. The two cited works are not in contrast because they are based on different approach to the problem and on a different analysis. However in both cases, the findings were not consistent with the large scale structure distribution of the ISM, derived from pulsar measurements. Furthermore, Kedziora-Chudczer et al. (2001) found no clear correlations between the maximum of variability for the observed sources and the galactic latitude, in the statistical analysis of the ATCA survey for intraday variability.

Regarding our data, figure 4.1 shows the variability amplitudes of all our variable (type I and II) sources plotted versus galactic latitude b: No evidence for correlations is found either in the total intensity or in the polarization variability. From such analysis one finds that same variable sources show different IDV behaviors at different epochs: eg. for 0917+624, which is at $b = +41\,^\circ$, one sees that the values of the amplitude of modulation show a huge scattering (~ 3 up to ~ 20).

The sources in our sample are not evenly distributed, most of them lie in a region of the sky $20\,^\circ < b < 50\,^\circ$, which is also occupied by galactic loops (see Heeschen et al. 1987). Therefore it is hard to perform a conclusive statistical study with such a still limited sample. The lack of strong b-dependence together with the RISS theory which limits the distance of the scattering screen to few tens of parsec demonstrates, however, that the scattering is not caused by the global matter distribution in the ISM, but could be due to clouds localized and homogeneously distributed in our surrounding.

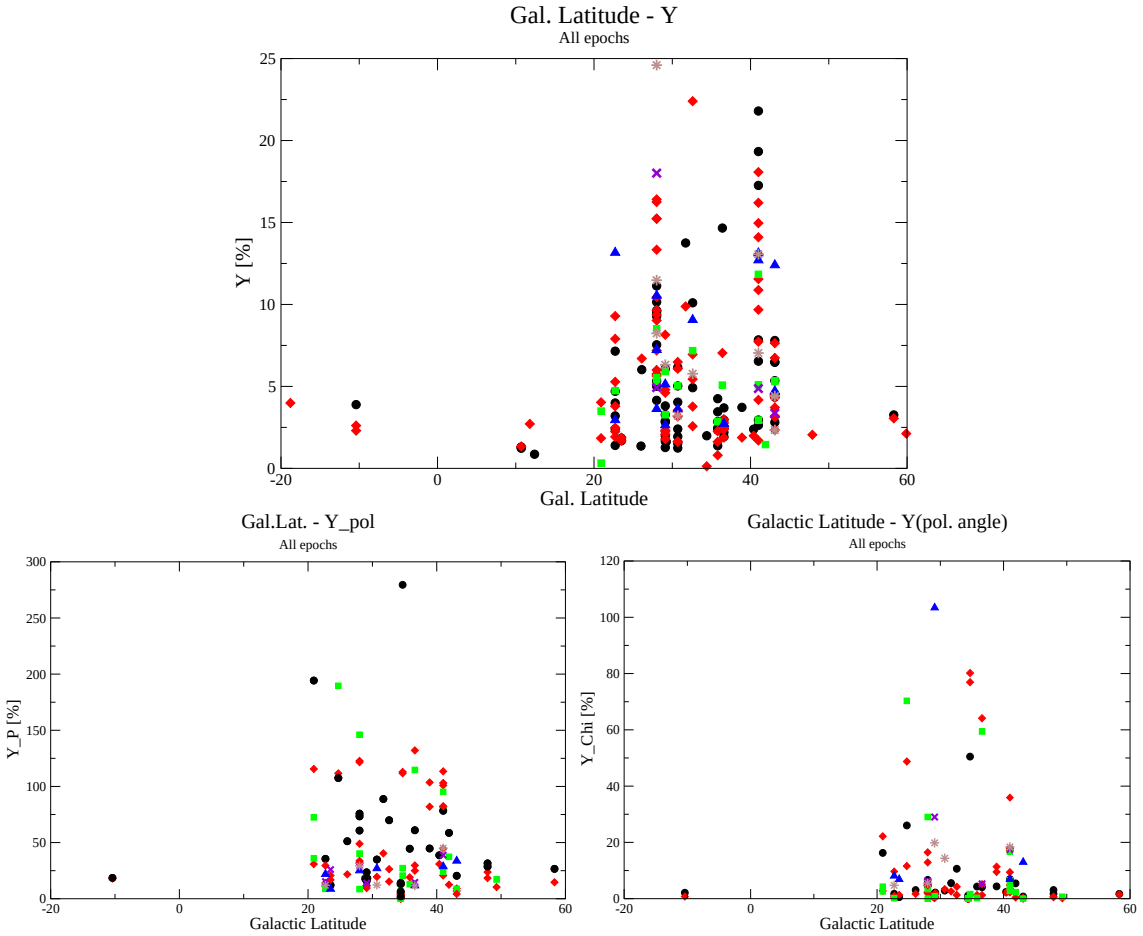

Figure 4.1: Variability amplitudes and galactic latitude (summary of all epochs). The *top panel* shows the total intensity information. On the *bottom:* the *left panel* shows the variability amplitudes of the polarized flux density and the *right panel* the polarization angle variability. *Blue triangles*: 20 cm, *Black circles*: 11 cm, *Red diamonds*: 6 cm, *Brown stars*: 3.6 cm, *Green squares*: 2.8 cm and *Violet crosses*: 2 cm.

4.2 Source-intrinsic characteristics and rapid variability

Another test is to study the variations in view of intrinsic properties of radio sources. First, we analyze a possible dependence of the variability on the brightness of the source. Figure 4.2 shows the total flux density of all the sources at all epochs, the different symbols represent different observing wavelength: 20 cm corresponds to blue triangles, 11 cm to black circles, 6 cm to red diamonds, 3.6 cm to brown stars, 2.8 cm to green squares and 2 cm to violet crosses. Moreover for the total intensity a linear least-square fit was performed on all the data sets to show the possible correlations between

S and Y. The correlation degree between the fit and the data is small, however, the outcoming trend could be considered as an indication of larger variability at low flux densities. The slope of the fit could indicate intrinsic long-term changes in the flux density of quasars and BL Lacs. Such long term variability is interpreted as structural variations in the innermost regions of the jets: eg. emission of new jet components or shock propagation inside the jets. In fact, we may argue that when a new component is emitted from the core, the variability is quenched due to a larger apparent source size or because the long-term core activity dominates on the intrinsic mechanism causing the rapid variability.
However, one should also consider the ratio between the compact core flux density and the extended (non-scintillating) jet emission. The low variability, observed at high flux densities, could be explained in terms of a stronger contribution of the jet emission to the total flux density. Such effect should vanish at shorter wavelengths since the emission is more dominated by the radiation from the compact core. The slightly inverted slope of the least-square fits on the 2.8 cm data, shown in figure 4.3, validate such interpretation. However, one could also take into account an intrinsic contribution to the variability, which becomes more dominant at shorter wavelengths.

In a more general way, it is possible that a mixture of both intrinsic and extrinsic effects is always present. At higher frequencies (and in some epochs even at low frequency) the sole extrinsic explanation is not sufficient to describe the observed variability.

The occurrence of IDV may also be dependent on redshift:
From the distribution of the variability amplitude (fig. 4.4), one immediately notes that the variability can be strong or weak without any dependence on redshift. As for the galactic latitude correlation, the plot shows again that the same sources behave in a different way at different epochs. Such changes of the IDV characteristics with the epoch and the lack of any evidence on z dependence demonstrate again that the scattering screen is very localized in the Galaxy. Again the intrinsic structural changes in the observed objects must play an important role in the evolution of the IDV characteristics.

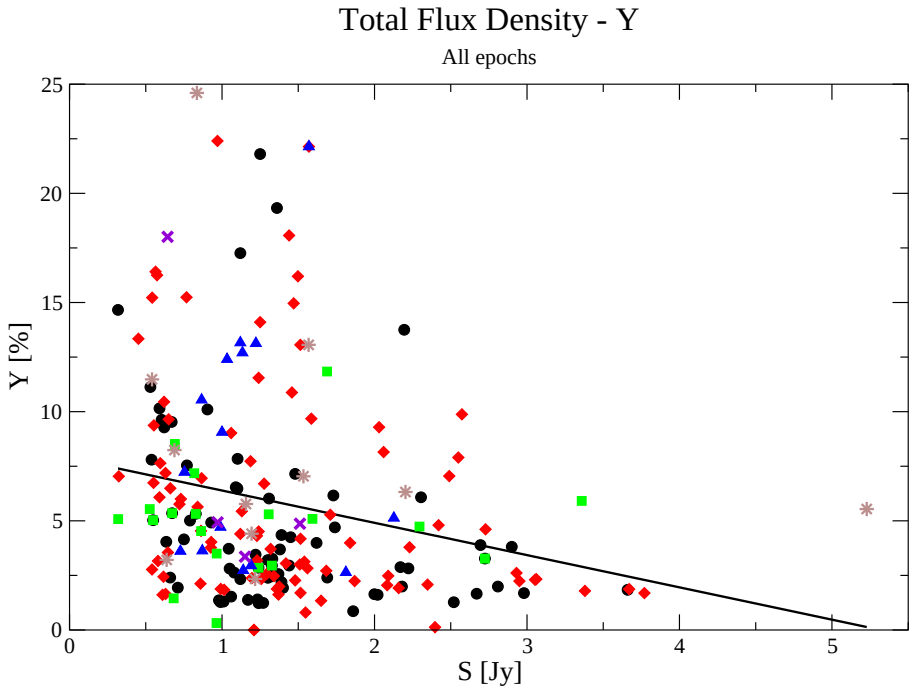

Figure 4.2: Total flux density against variability. *Blue triangles*: 20 cm, *Black circles*: 11 cm, *Red diamonds*: 6 cm, *Brown stars*: 3.6 cm, *Green squares*: 2.8 cm and *Violet crosses*: 2 cm. The least square fit on all the data is also shown (*black straight lines*).

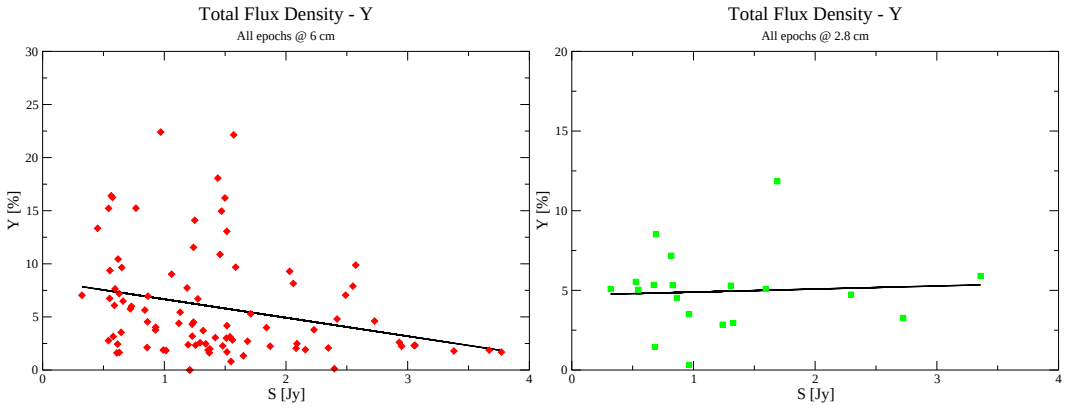

Figure 4.3: Total flux density against variability at 6 (**left panel** and 2.8 cm (**right panel**), respectively. The least square fits on the data are also shown (*black straight lines*).

4.2.1 Spectral index variability

Correlation between the measured amplitude of variations and the spectral indices (fig. 4.5), calculated by Kühr et al. (1981), allows to compare source-intrinsic characteristics to rapid variability. The available data for the single sources in our archive are too sparse for this kind of analysis, but a statistical study on our complete sample gives

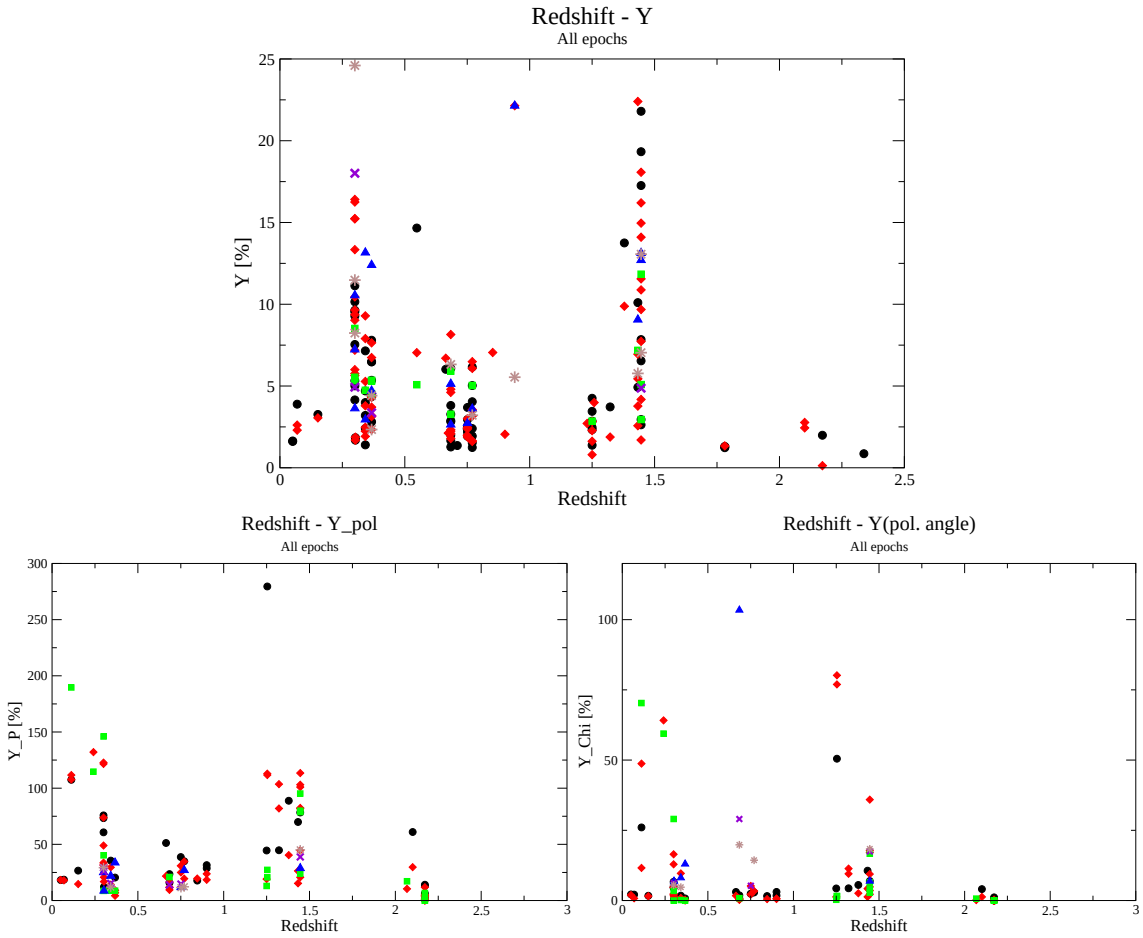

Figure 4.4: Variability amplitude against redshift. The *top panel* shows the total intensity information. On the *bottom*: the *left panel* shows the variability amplitudes of the polarized flux density and the *right panel* the polarization angle variability. *Blue triangles*: 20 cm, *Black circles*: 11 cm, *Red diamonds*: 6 cm, *Brown stars*: 3.6 cm, *Green squares*: 2.8 cm and *Violet crosses*: 2 cm.

an overall description of the variability behaviour at any epoch.

Figure 4.5 shows that the highest variability in total intensity and polarization are directly related to a very flat-spectrum radio core (α from ~ -0.5 up to ~ 0). Previous studies, here confirmed, predict that sources with steeper spectrum are less variable (see Quirrenbach et al. 1992 and recently Kedziora-Chudczer et al. 2001 for a sample of southern hemisphere radio sources). In this analysis we note an indication that even very inverted-spectrum sources show less variability. The synchrotron theory predicts (eg. Lobanov and Zensus 1999) that the emission of a new component in the compact core of an AGNs produces an increase in the spectral index: the spectrum becomes flatter or, in case of flat self-absorbed components, more inverted. Under

such assumption we have again a connection between intrinsic changes in the radio core and IDV characteristics. In section 4.2 the emission of a new component from the core was already related to a change in the IDV pattern, now we have a further indication of such a scenario: in a quiescent phase of the flat-spectrum radio core, the rapid variability is present, while in a flaring phase (more inverted spectrum) the variations could be quenched by the emission of new components and a larger core size: the scattering effects are reduced by the increase in the apparent source size and/or the intrinsic variability is dominated by strong core activity.

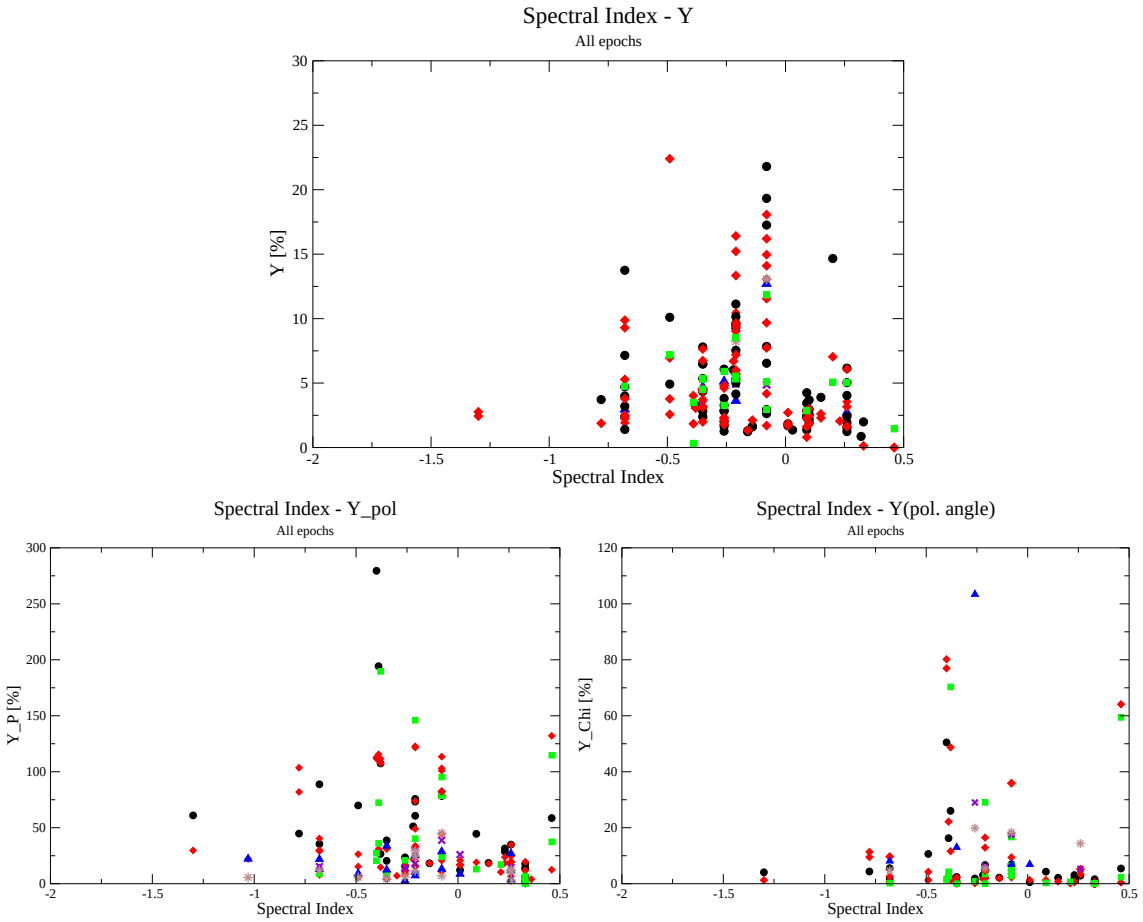

Figure 4.5: Variability amplitude against spectral index. The *top panel* shows the total intensity information. On the *bottom*: the *left panel* shows the variability amplitudes of the polarized flux density and the *right panel* the polarization angle variability. *Blue triangles*: 20 cm, *Black circles*: 11 cm, *Red diamonds*: 6 cm, *Brown stars*: 3.6 cm, *Green squares*: 2.8 cm and *Violet crosses*: 2 cm.

During a single session of observations, it is possible to study the variation of the spectral index with the time. Figure 4.6 shows the spectral index variability in March

2000 of 0716+714 compared to the nearby secondary calibrator 0836+710. While in the calibrator, as expected, a constant relation between the flux density at 11 and 6 cm is shown, for 0716+714 large and very rapid (intraday) variability of the spectral index is clearly observable. Such behaviour could be explained within the RISS theory considering the frequency dependence on the strength of variability (see eq. 5.3): the growth in flux density affects the variability at different frequencies in different ways.

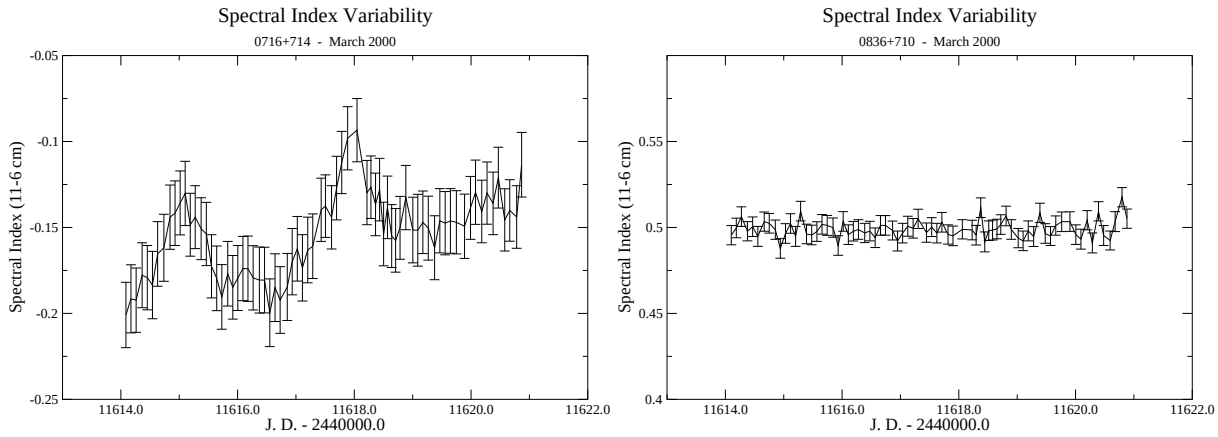

Figure 4.6: Spectral index variability of 0716+714 and 0836+710 in March 2000.

4.2.2 Polarization angle variability at different frequency

It was shown that the IDV characteristics are more pronounced in the polarized flux density P and polarization angle χ. Propagation of the radiation through the interstellar medium can rotate the polarization angle via *Faraday Rotation*. Faraday rotation occurs when a linearly polarized electromagnetic wave passes through a magnetized plasma: the two circular polarized components of the wave pass through the plasma with two different speeds and, after a certain path, the phase shift of these components is changed causing a rotation of the polarization vector:

$$\Delta\chi[rad] = \lambda^2 \cdot 8.1 \cdot 10^5 \int n_e B_{\|} \mathrm{d}l \tag{4.1}$$

where $B_{\|}$ is the magnetic field along the line of sight, λ is the wavelength measured in meter and dl, the pathlength, in parsec.

In principle, via propagation effects, it is possible to describe the variations of the polarization angle. Our study, of which figure 4.7 is an example, shows a complex

pattern of the rotation of the polarization angle with the frequency. Assuming that the observed variations are due to Faraday rotation, one has to consider very fast and physically improbable changes either in the electron density of the screen or in the magnetic field along the line of sight with time scales of around 1 day. The nature of the variations must therefore lie in the source. We suggest a multi-component structure (Qian et al. 2001) of the innermost regions of the radio jet. The vector, which results from the sum of the polarization vectors of the various components, could have a different orientation and amplitude at different frequencies. Therefore, if one of the components scintillates, we could have changes in the difference of the resulting polarization angles and the pattern seen in figure 4.7 could be reproduced.
Multi-component models are able to explain some of the polarization characteristics of the intraday variable radio sources via interstellar scintillation. Qian et al. (2001) use a 2-component model to describe the rapid polarization variations at 20 cm of the quasar 0917+624. Recently, Rickett et al. (2002) made a fit of the polarization pattern of the extreme intraday variable PKS 0405−38 using two polarized components in the parsec-scale structure of the source. However, Qian et al. (2002) have also tried 3-, 4-, and 5-component models and a complete description of all the observed polarization characteristics of IDV was still not possible, mainly the polarization angle changes could not be reproduced.
In conclusion, the *apparent "Faraday rotation"* (fig. 4.7) could be interpreted as an indication of a complex structure in the jets with at least two (if not more) ultra-compact components. High resolution observations (e.g. VLBI and millimeter VLBI) are necessary to check the relationship between the scintillating components and the observed VLBI structures.

4.3 Analysis of the Time scales

The changes of the characteristic variability time scales of 0716+714 were analyzed to search for possible correlations with other variability characteristics of this source.
The time scales have been derived from the structure functions of the variability light curves (see section 3.2): in this analysis, the first maximum in the SF was used to extract the typical time scale, t_{IDV}. The power spectra (see section 3.3) were also used

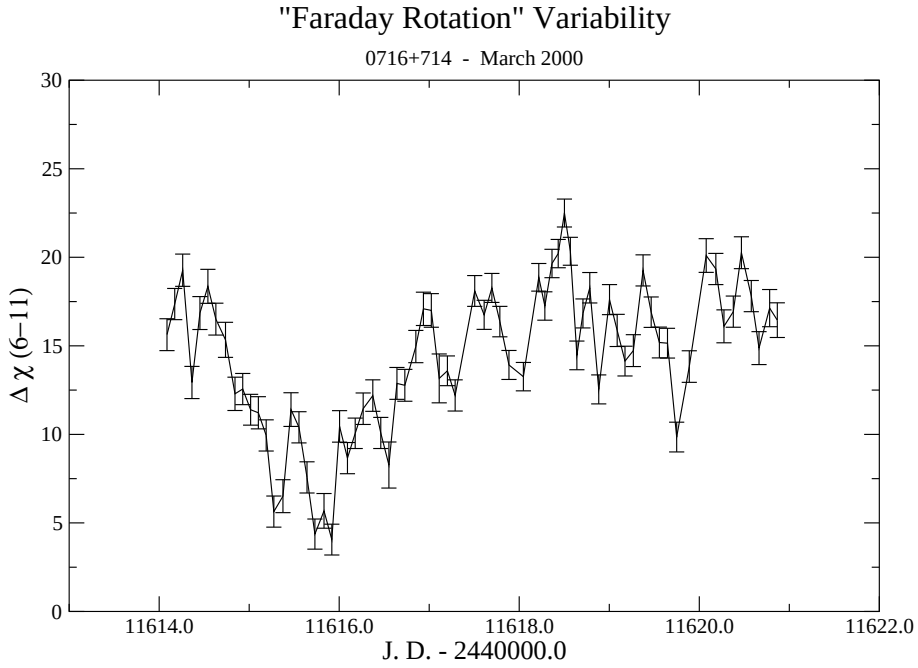

Figure 4.7: "Faraday Rotation" variability of 0716+714 in March 2000.

to improve the determination of the time scales in cases of "noisy" light curves.

First of all, a comparison was performed between the long-term variability of 0716+714 and t_{IDV}. Figure 4.8 shows, on the bottom panel, the measurements of the total flux density of 0716+714 from the AGN monitoring of the University of Michigan Radio Astronomical Observatory (UMRAO) at 5 GHz. These data are compared with the time scales of the source from the IDV monitoring experiments, which are shown on the top panel: no clear correlations can be seen between changes of the IDV time scales and the rising (or descending) phases of the radio light curve. From the lack of correlation could follow the interpretation that the characteristics of IDV are independent of the physical process, eg. the emission of new VLBI components, causing the long term variability. However, it is important to consider that the measurements of t_{IDV} are too sparse to completely exclude any dependence among the various variability characteristics of the AGNs.

Moreover, one can immediately note that the characteristic variability time scale of 0716+714 changes with the observing epoch. At 5 GHz a factor 2 variations in t_{IDV} are observed. It is possible to test whether the observed rapid variability could be caused by an annual modulation (see section 1.3.1), which is due to the orbital motion of the Earth. In figure 4.9, the IDV time scales are plotted with respect to the month,

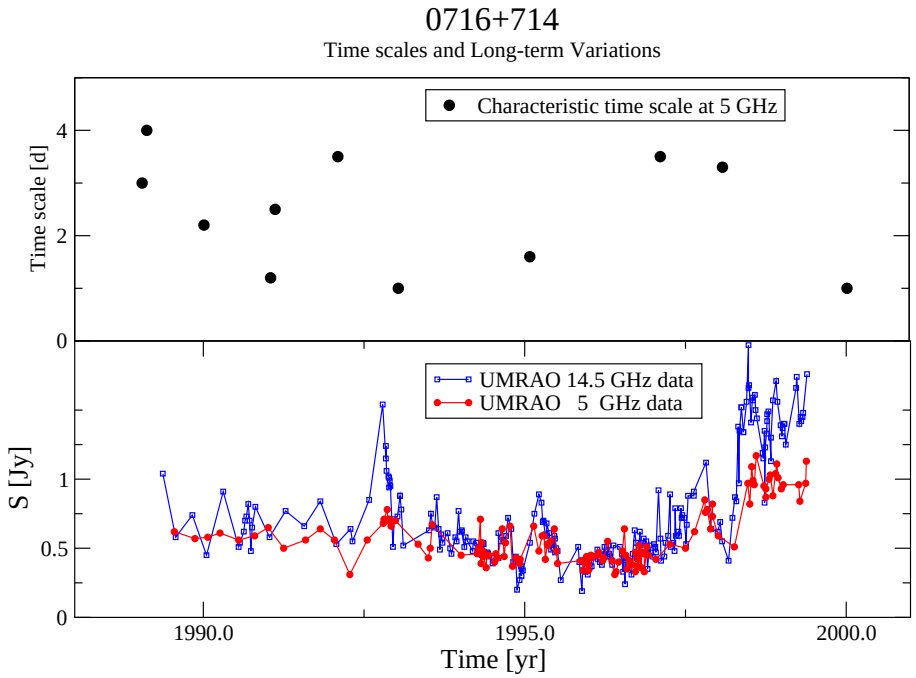

Figure 4.8: Time scales of 0716+714 (*top panel*) compared to a long-term light curve at 5 GHz (*bottom panel*), data from the UMRAO monitoring of AGNs at 5 and 14.5 GHz.

in which the observations were carried out. The slow-down of the variability around

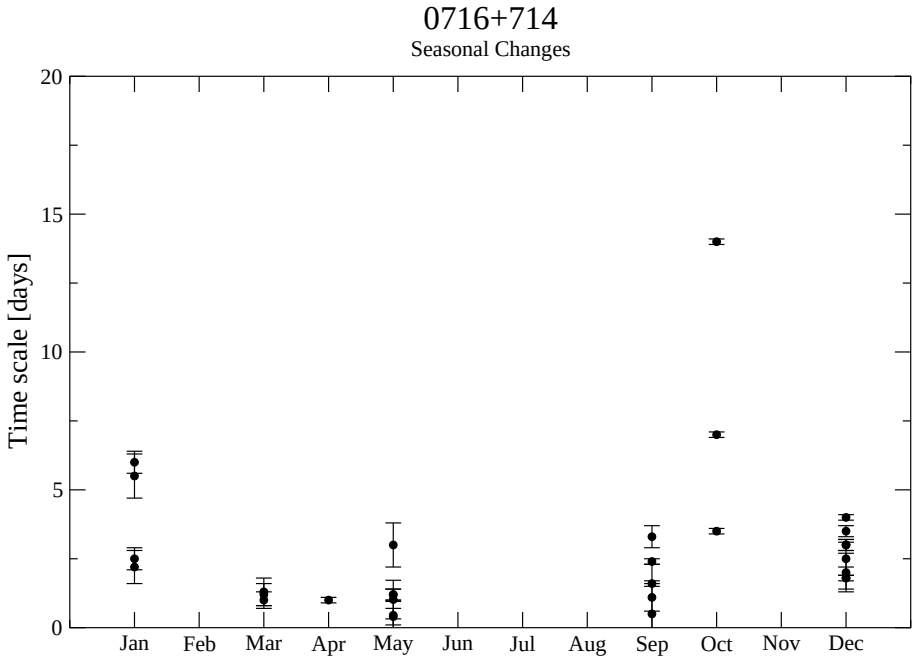

Figure 4.9: Time scales of 0716+714 against period of the year.

October could be an indication of a seasonal modulation of the IDV. One could, therefore, argue that scintillation effects could play an important role in the changes of the

variability characteristics of 0716+714.

A systematic analysis of the variability time scales for all the sources of the complete sample is in progress. This complete study will provide further information about the physical processes, or the mixture of precesses, of the short term variability in blazars.

Chapter 5

A multi-frequency approach

Multi-frequency observations constrain the competing models describing the rapid variability observed in flat-spectrum radio sources. Furthermore RISS models, applied to the IDV sources, could be combined with VLBI and/or pulsar observations to put some further constraints to the ISM structure and the intrinsic source sizes. In this chapter we compare statistical models for the RISS to our data and we try to analyze the mixture of the causes for the rapid variability in active galactic nuclei.

5.1 Variability characteristics of flat-spectrum radio sources

The scattering theory (see section 1.3) predicts two regimes of refractive interstellar scintillation: weak and strong. A change between strong and weak regimes occurs around 3–8 GHz (Walker 1998): below a critical frequency ν_c, which can be determined with multi-frequency observations, the scattering is strong. As it was shown in the chapter 4, different IDV patterns at different epochs for the same source is a common phenomenon.

In figure 5.1 we analyze the changes in the variability strength, Y, in 0716+714 for 6 different epochs, combining all available data including 3 sessions observed with the VLA (see Quirrenbach et al. 2000):

May 1989 (VLA data): The variability rises from 20 cm up to 6 cm and at shorter wavelength a decrease in the amplitudes of the variations is observed.

February 1990 (VLA data): The variability is larger and during this observing ses-

sion a correlation between radio and optical regimes was observed (see 1.2, Wagner et al. 1996). As in May 1989, the variations rise from 20 cm up to 6 cm and decrease at 3.6 cm. But at this epoch, the variability amplitudes rise again towards higher frequency (2 cm).

December 1991: Again the variability at 6 cm, i.e. $\nu_c \sim 5$ GHz, is more pronounced than at other wavelengths.

October 1992 (VLA data): A monotonic increase of the variability amplitude up to 3.6 cm was observed.

September 1998: The variations are more pronounced at very high frequency. In particular, the observed IDV at 32 GHz (Krichbaum et al. 2002) is difficult to explain with the interstellar scintillation model.

March 2000: During the radio-optical campaign (see 5.4), 0716+714 showed a decrease in the variability amplitude from low towards higher frequencies as expected in the weak scattering regime.

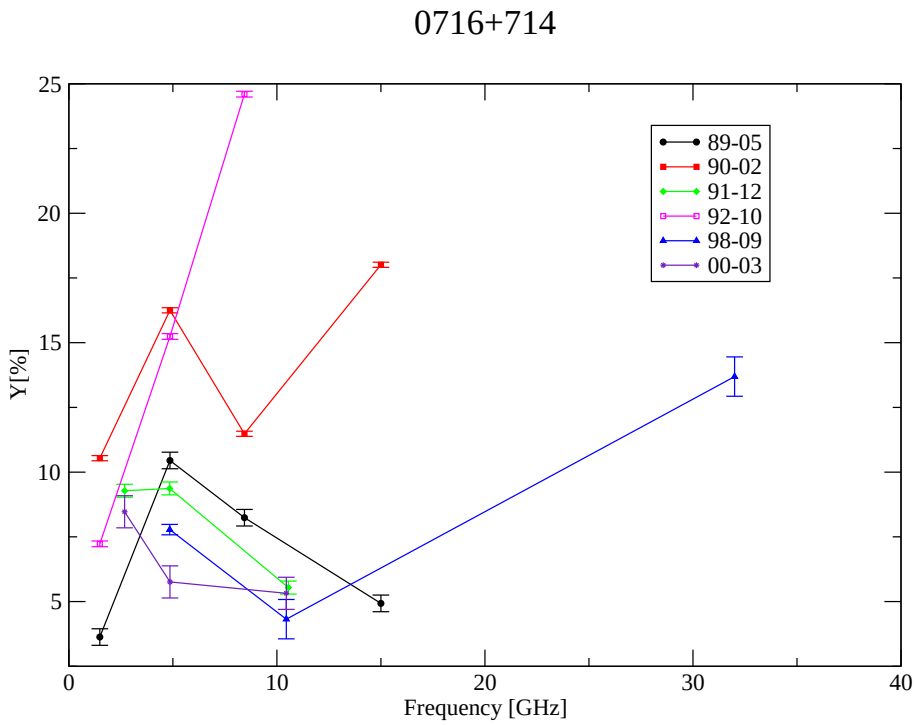

Figure 5.1: Variability amplitudes against frequency at different epochs.

From this overall analysis of the frequency dependence of$Y$, we immediately note that the frequency in which the variability is more pronounced (i.e. ν_c) differs with the epoch and the amplitude of such variability changes, too. Moreover the curves show many trends and slopes and one can argue that different mechanisms can be simultaneously involved but alternatively dominant in the occurrence of IDV. Once again it is possible to interpret the different variability behaviors in the same sources as changes either in the source structure or in the interstellar medium favoring an explanation of the IDV phenomenon that takes into account both intrinsic and extrinsic models.
Changes in the variability characteristics of the studied objects with the observing epochs are common: some sources appeared to be type II or type 0 depending on the epoch of the observations (see Kraus et al. 2003). Equation 1.9 tells us that the relative velocity of the scattering screen varies during the course of one year due to changes in the projected velocity vector of the Earth. The annual modulation (section 1.3.1) successfully explains the changes in the variability characteristics for the extremely rapid IDV sources (eg. J1819+38, see section 1.3.2), but it is not clear whether it plays an important role in the "classic" IDV. In figure 5.1, the curve for February 1992 and March 2000 (also for October 1992 and September 1998) are extremely different although the observations were carried out in similar periods of the year, when the relative velocity between the Earth and the scattering screen is similar. Excluding therefore an extrinsic phenomenon like annual modulation of the time scales, one can argue that the changes in the variability pattern are due to source-intrinsic structure changes which, however, also effect the RISS-related features of the source. We can assume that the apparent size of the variable component changes and quenches the variability as Fuhrmann et al. (2002) interpreted in the case of the radio core 0917+624 (section 1.3.1).
In this view, it is hard to find an overall conclusion with a statistical study if only one of the two competitive models for the rapid variations in the AGNs is considered. Flat-spectrum radio sources are strongly variable on longer time scales due to intrinsic modification of the source structure like the emission of new components: hence IDV shows different characteristics at different epochs due to changes in the apparent source size. Changes in the source morphology and scattering can be strictly related and a comprehensive explanation of the IDV phenomenon has to consider a mixture of both intrinsic and extrinsic contributions.

Finally, in some cases, we also see an increase of the variability amplitudes at high frequencies. This is not in agreement with the expectations from RISS: because of the frequency dependence of the modulation index (see below, eq. 5.3) in the refractive interstellar scintillation theory, the flickering vanishes towards higher frequencies. Therefore RISS cannot explain the observed trends and one has to take into account a source intrinsic contribution, which increasingly dominates towards higher frequencies.

5.2 Modeling the quenched scintillation

In section 1.3, we discussed the theory of refractive interstellar scintillation. Now, we want to analyze the data with a model (Beckert et al. 2002a) for the quenched scattering.

Coles et al. (1987) found a relation between the autocorrelation function and physical characteristics of the interstellar medium. In particular, taking into account the source size and its brightness profile, it is possible to describe the fast and slow variations (hours to months) of the flux density within the refractive interstellar scintillation theory.

The spacial spectrum of the electron density fluctuations in the ISM is:

$$\Phi(z, \mathrm{q}) = C_N^2(z)\mathrm{q}^{-\beta} \qquad (\mathrm{q}_{min} < \mathrm{q} < \mathrm{q}_{max}) \tag{5.1}$$

where z is the coordinate along the line of sight, q is the spacial frequency (q_{min} and q_{max} are the lower and upper cut-off in the power law[1]), $C_N^2(z)$ defines the turbulence of the interstellar gas and such turbulence is described by the *scattering measure*: SM=$\int C_N^2(z)\mathrm{d}z$. The autocorrelation function can be related from theoretical considerations to the physical parameter for the interstellar medium which is here described by the Fresnel angular scale, θ_F (= r_F/d, see section 1.3), and $\Phi(z, \mathrm{q})$. Coles et al. (1987) report:

$$\rho(\mathbf{x}) = 8\pi r_e \lambda^2 \int_0^\mathrm{d} \int_{-\infty}^{+\infty} \exp[i\mathbf{x}\mathrm{q}] \cdot \Phi(z, \mathrm{q}) \cdot \sin^2(\mathrm{q}z\theta_F/\sqrt{2}) \cdot |V(\mathbf{q})|^2 \mathrm{d}z\mathrm{d}\mathbf{q} \tag{5.2}$$

λ is the observing wavelength, d the distance and $|V(\mathbf{q})|^2$ the visibility of the source brightness profile. Physically, $\mathbf{q}$ is a two dimensional spacial vector perpendicular to

[1]The exponent β for a Kolmogorov spectrum of the density fluctuations in the ISM is equal to 11/3.

the line of sight in screen reference frame. In the observer plane, it corresponds to the vector $\mathbf{x}$=$\mathbf{v}$t (see section 1.3.1). Beckert et al. (2002a) solved in an analytical way equation 5.2 for different source luminosity profiles and it is now possible to relate ISM parameters to observational quantities as the modulation index:

$$m^2 = 2\left(\frac{r_e}{\mathrm{d}\theta^2}\right)^2 \lambda^4 (\mathrm{d}\theta)^{\beta-2} SM \cdot f(\beta) \tag{5.3}$$

θ is the apparent source size. The function $f(\beta)$ depends on β as well as on the chosen profile for the source brightness and, in any case, it has a value close to unity.
Such analytical model for m is used to test the propagation effects in the IDV phenomenon. Equation 5.3 relates the modulation index to observable parameters of the ISM. In this work, we assume some values for these parameters and compare the model to the observations. The figure 5.2 shows the frequency dependent patterns of the modulation index of the rapid variable radio sources observed in March 2000. In the same figure we plotted a theoretical curve which was derived with the following assumptions:

- $C_N^2 \sim 10^{-3}\,\mathrm{m}^{-20/3}$ (Coles et al. 1987). For the scattering measure SM, we assumed a slab model for the ISM: we consider only a slab 1 pc wide of constant C_N^2 at distance d responsible for the turbulence causing the interstellar scattering.

- We used two values for the distance of the scattering screen: d= 10 and 100 pc.

- $\theta = 100\mu$as at 11 cm. The source size can be estimated from the analysis of the structure function (see section 5.3) and it is consistent with the upper limits set by VLBI measurements.

The resulting curves (fig. 5.2 open circles and open squares) are valid in weak (or quenched) scattering and in March 2000 seems to reproduce qualitatively the behaviour of the rapid variable objects. The discrepancies start at higher frequencies: the observed sources show an increasing trend toward the highest ν. One can argue that intrinsic variations are always present, but dominated at cm-wavelengths by the scintillation. The unexpected (for RISS) enhanced variability, observed in some sources, could be explained with a more and more dominant entanglement of intrinsic effects.

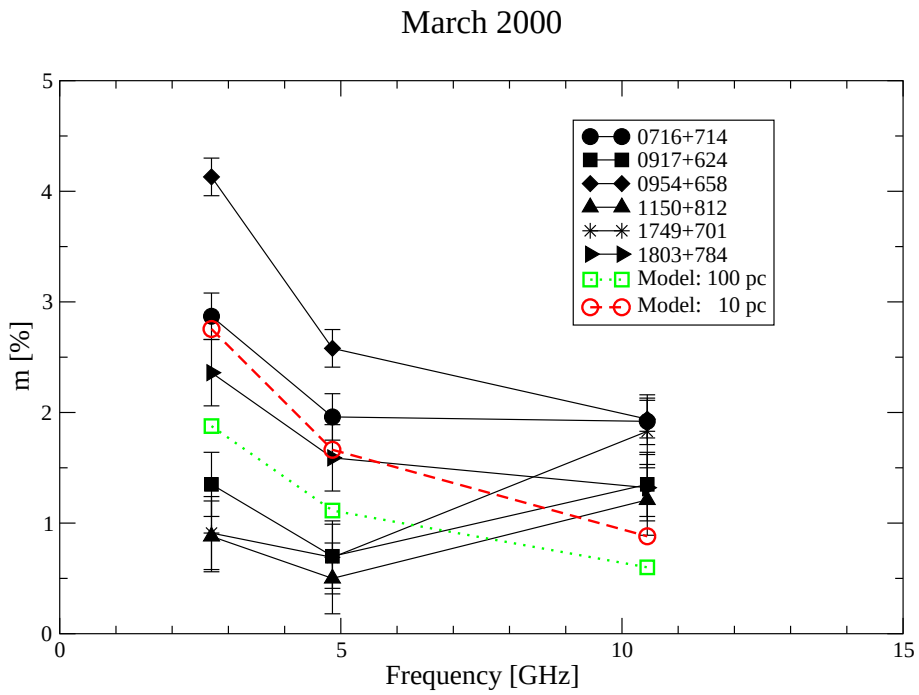

Figure 5.2: Modulation Index against frequency during March 2000 for the variable sources. The open (red) circles and the open (green) squares represent the model described in the text using screen distances of 10 pc and 100 pc, respectively.

5.3 The Structure Function and the compactness of the flat-spectrum radio sources.

In the section 3.2, the mathematical definition of the structure function was given and it was discussed what kind of information can be provided from the characteristic time scales of time series. From the analytical solution of the autocorrelation function (section 5.2), it is possible to relate the time scales from the SF to physical characteristics of either the interstellar medium (in case of sole scattering) or the source size and its brightness profile (in a more general case). Beckert et al. (2002a) built a slab model for the scattering measure and they find that for small time lags up to a break time scale, t_{ISM} (which depends only on the interstellar medium characteristics) the SF shows a quadratic dependence on the time lag:

$$SF(\theta) = 2\rho(0)\left(\frac{\upsilon\tau}{\mathrm{d}\theta}\right)^2 f(\beta) \tag{5.4}$$

We tried to fit our data with such model: figure 5.3 shows the SF of 0716+714 in March 2000 and the best fit of the model on the data. The horizontal line corresponds to the modulation index and the typical IDV time scale t_{IDV} is derived from the SF

using the modulation index from the data: t_{IDV} corresponds to the time lag (plus a theoretical factor of 1.207, see Beckert et al. 2002a) when the SF cross the $2m^2$-'plateau' (see figure 5.3). The fit at small time lags is not a quadratic function as expected and the break at t_{ISM} is not present. We can argue either that the variability is not due to the propagation through the ISM or that the slab model is too simple to describe the frequency dependence of the IDV. In the first case, intrinsic variability can be superimposed to the variations due to the refractive scattering and the structure function contains information on both mechanisms. In the second case, the slope of the SF can be reproduced, if one considers a stratified medium: many slabs of constant (but different) scattering measures along the line of sight that are responsible for the overall scintillation.

The characteristic IDV time scale corresponds, in the RISS theory, to a source size[2]:

$$\theta = \frac{v}{\mathrm{d}} \frac{t_{IDV}}{2}. \tag{5.5}$$

It was noted above that the characteristic time scale of the ISM, t_{ISM}, is not present. However in all the SFs it is possible to measure the typical variability time scale, t_{IDV}. If t_{ISM} and t_{IDV} were both known from the SF, a multi-frequency approach would permit to determine the distance, d, of the scattering screen, the scattering measure SM, the exponent β of the power spectrum of the fluctuation in the ISM, the velocity v of the scattering screen and the apparent source size θ. That is the complete information on the ISM parameters and on the intrinsic size of the scattering component in the source (if the redshift is known). In our case and in all the SFs in our archive, it is difficult to find a good determination of t_{ISM} and one has to deal only with a multi-frequency study of t_{IDV} which provides the size of the scattering region in the core of the compact radio sources (table 5.1). Taking into account a linear dependence on the wavelength of the source size ($\theta_{\lambda_2} = \theta_{\lambda_1} \cdot \lambda_1/\lambda_2$), the apparent source size calculated at 11 and 6 cm are in good agreement: $\theta_{11} = 121 \pm 37\,\mu$as and $\theta_6 = 133 \pm 54\,\mu$as while the data at 2.8 cm ($\theta_{2.8} = 340 \pm 125\,\mu$as) again do not fit the scattering model as unique explanation for the observed variability (see fig. 5.4).

For the velocity of the scattering screen, we assumed that only the Earth motion has

[2]This expression for θ derives from the analytical solution of the SF discussed in Beckert et al. (2002a)

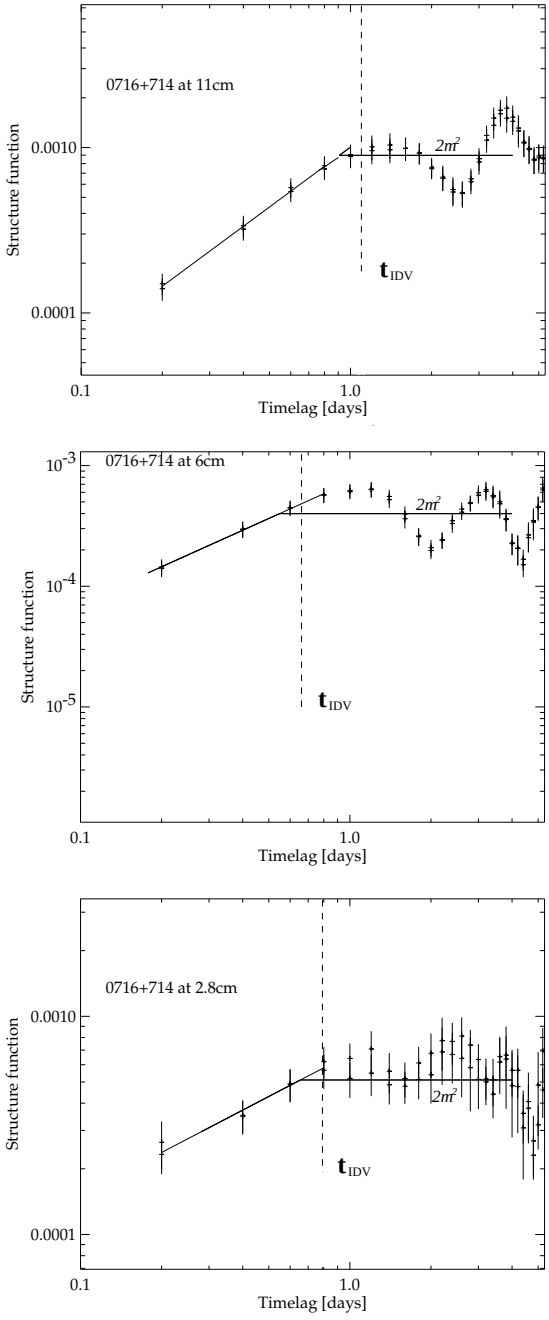

Figure 5.3: Structure function of 0716+714 at 11, 6 and 2.8 cm in March 2000. The modulation index (actually $2m^2$) is plotted as a horizontal line and corresponds to a "plateau" of the SF for large time lags. The best fit on the first part of the SF (see text) is showed and it defines the characteristic time scale of the variability in the light curve.

a dominant contribution, neglecting the random velocity distribution of the clouds in the ISM: in any case Cordes and Lazio (2001) calculated that the ISM structures have

λ [cm]	t_{IDV} [d]	d [pc]	v [km/s]	θ [μas]
11	1.10 ± 0.34	100	38	121 ± 37
6	0.66 ± 0.27	100	38	72 ± 30
2.8	0.79 ± 0.29	100	38	87 ± 32

Table 5.1: Apparent source size calculated from the SF.

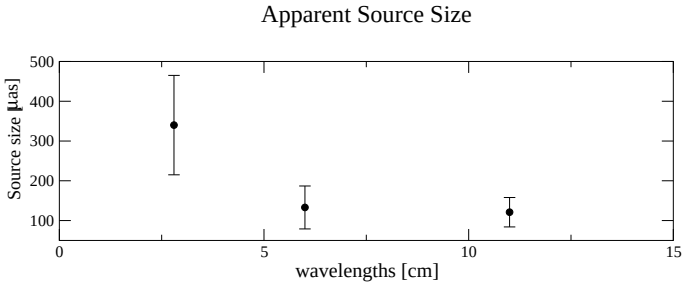

Figure 5.4: Apparent source sizes at different wavelengths, calculated as described in the text.

typical velocities not exceeding 10 km/s. During the observation in March 2000, the projected velocity of the Earth was $v = 38.03 \pm 0.65$ km/s. The error in this parameter is calculated considering the difference of the velocity between the starting and the ending date of the observations. Regarding the distance, we showed the results for an arbitrary, but reasonable value of 100 pc: the possibility of different distances, i.e. 10 pc, would imply an increase of the angular size of an order of magnitude.

5.4 Radio-Optical Campaign in March 2000

In optical bands, extremely rapid *intranight* variability is often observed. This effect is considered intrinsic and explained via perturbations in accretion disks of the AGN (see Krishan and Wiita 1994) or acceleration in shock front inside turbulent jets (Hughes et al. 1985 and Koenigl and Choudhuri 1985).

As discussed in section 1.1, the claimed correlations between the radio and optical bands put severe constraints on the nature of the radio IDV. In particular, with such a correlation the interstellar scintillation effects can be ruled out as the unique mechanism causing the rapid flux density variations of the radio emission. However, after the confirmed case for broad-band correlations in 0716+714 in 1990 and an indication of such a correlation in 0954+658 (Wagner et al. 1993), no further experiments showed such

effect. There are several problems which make a final confirmation of correlated variability characteristics between the radio and optical bands difficult. First of all, due to the oscillatory nature and the quasi-periodicity of the phenomenon, it is hard to unambiguously cross-correlate the variations observed in the different regimes. Furthermore a huge amount of continuous simultaneous observing time is necessary to cover all the possible time scales: many radio and optical telescopes around the world have to dedicate continuously at least 2–3 weeks of observing time to monitor the program sources.

In March 2000 (the table 5.2 shows the participating telescopes) it was possible to organize a coordinate multi-frequency campaign, intended to repeat the 1990 experiment. Unfortunately, however, the 100-m Effelsberg radio telescope, which had to provide the denser radio monitoring, could only participate for one week.
Figure 5.5 shows a general decreasing trend (after an initial remarkable outburst) of the optical light curve of 0716+714 between from J.D. 2451612 up to J.D. 2451620 and a slightly increasing trend afterwards. The data points from the IRAM monitoring at 3 mm are monotonically increasing while the Effelsberg observations (at 11, 6 and 2.8 cm) present no such long term effect. This pattern can be described in terms of a propagating shock visible at different times. Due to the different optical depths in radio and optical regimes, a change in flux density is faster in the optical than in the radio band. Therefore, the optical flux density would probably decrease if we are observing at a certain time after the maximum of the variation. At this time, the flux density at millimeter wavelengths would instead start to increase (the variation has just started in this band) while in the centimeter regime the source would show no long-term changes in flux density as the variation would not have yet started here.
Regarding the fast variations, figure 5.5 shows no clear evidence any correlation between the optical and the radio light curves of 0716+714. Moreover, a cross-correlation study was performed (fig. 5.5, *bottom right*): to compare the data sets, the slopes in the light curves have been removed (fig. 5.5, *bottom left*). The correlation coefficient at zero time lag resulted ~ 0.2. The maxima (CCF~ 0.5) in the correlation factors occurred with 1 day delay between 11 cm and the optical data and with 1.3 days time lag between the optical and the 6 cm observations. Notably, in all the data set a quasi-periodicity of ~ 2.5 days was detected. On the one hand, a common quasi-periodicity

Optical telescopes

Telescope	Size	Date
Calar Alto	1.23m	28/2 - 3/4
La Palma	0.7m	1/3 - 31/3
Flagstaff	1.8m	11/3 - 24/3
Cananea	2.1m	7/3 - 22/3
YunNan	1.0m	13/3 - 18/3
Beijing	0.6m	2/3 - 23/3
Abastumani	0.7m	28/3 - 3/4

Radio telescopes

Telescope	Date
Effelsberg	10/3 - 17/3, 24h per day
Pico Veleta	8/3 - 30/3
Westerbork	6/3 - 26/3, 2.5h per day
RATAN-600	6/3 - 29/3

Table 5.2: Telescopes involved in the March 2000 radio-optical campaign. The analysis is still in progress for the data from Westerbork and RATAN-600.

could be interpreted as an indicator for the same mechanism causing the rapid variations. On the other hand, it is difficult to exactly recognize which features are common to the different bands.

Clearly such experiments bear a huge potential for the future and have to be repeated. In particular, in the millimeter and radio bands, the time sampling should be improved.

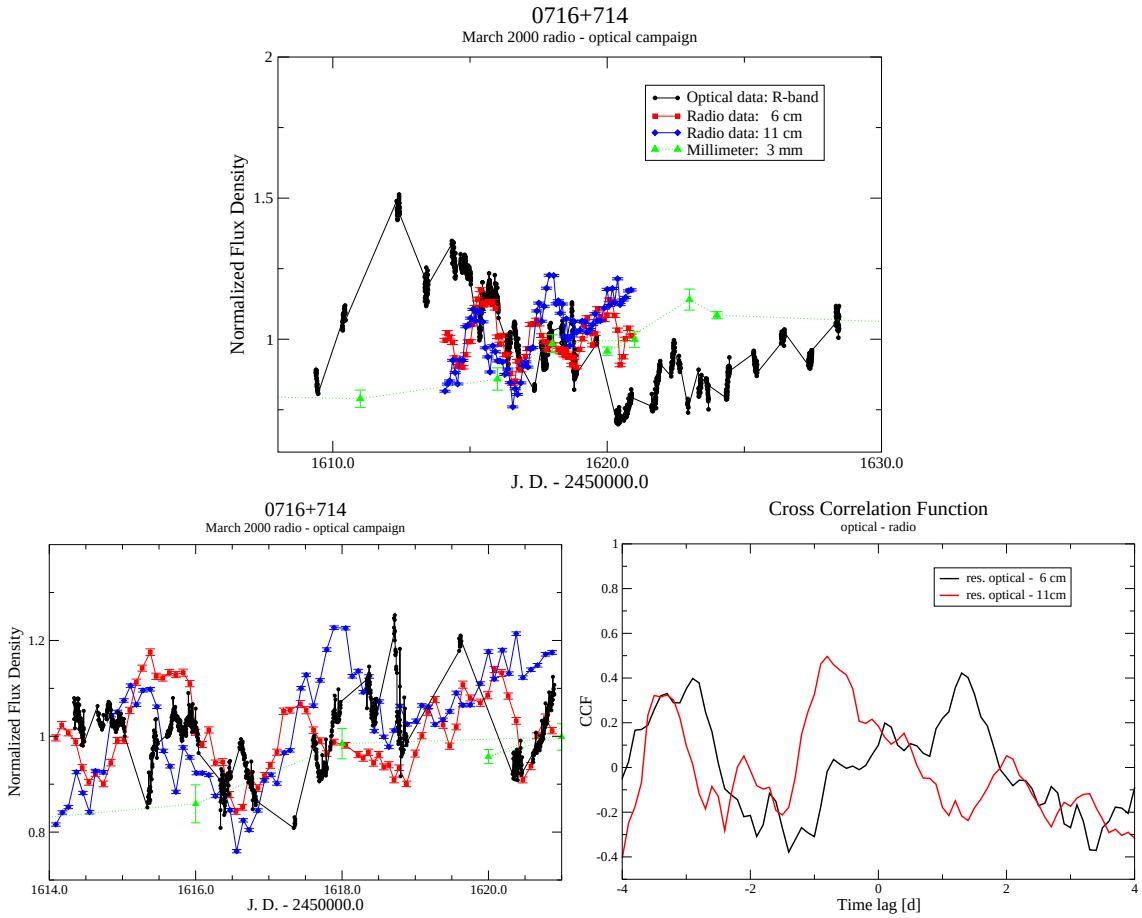

Figure 5.5: Radio-mm-Optical Data during the March 2000 Campaign.
Top: The *black circles* correspond to a preliminary analysis of the optical measurements in the R-band (Courtesy of Wagner and collaborators, Landessternwarte Heidelberg). Our data at 6 and 11 cm are plotted as *red squares* and *blue diamonds*, respectively. The *green triangles* corresponds to the Pico Veleta flux density monitoring of point-like radio sources.
Left bottom: The residual optical data compared to the radio data during the Effelsberg observing period. **Right bottom:** Cross-correlation functions between the residual optical and the radio data: the *black line* and the **red line** correspond to the optical-6 cm cross-correlation and the optical-11 cm cross-correlation, respectively.

Chapter 6

A very rapid Extreme Scattering Event in the IDV source 0954+658

The BL Lac object 0954+658 (m_V = 17 mag, Padovani and Giommi 1995; z=0.367, Stickel et al. 1994) is an extremely active radio source. Superluminal motion of the VLBI components have been observed (Jorstad et al. 2001) with apparent velocities up to $\sim 19h^{-1}c$ ($h = H_0/100$ is the reduced Hubble constant). The source is strongly polarized ($10 - 20\%$) and the polarization shows a complex structure at VLBI scale (Gabuzda and Cawthorne 1996). 0954+658 was the first source to show an Extreme Scattering Event (ESE: see Fiedler et al. 1987), indicating the presence of a clumpy interstellar medium along the line of sight. This BL Lac has been observed in most IDV monitoring projects discussed in this work. Also, fast variability in total and polarized flux density has been detected and the source is classified as a type II IDV (see section 3.2).

In the light curve of this object (fig. 6.1), observed in March 2000, we found that a drop in the flux density showed a systematic reversal of the time lags between adjacent frequencies. We explain such a particular variation as a very rapid ESE. It is here important to recall that the extreme scattering event seen by Fiedler et al. (1987) showed variations on a time scale of $\sim$ 18 weeks, much longer than the effect seen in our data (time scale $\sim$ 2 days).

In this chapter, the study of this ESE-like event will be shown and a description of the interstellar medium characteristics will be given using the multi-frequency approach to the IDV phenomenon as an instrument for the analysis.

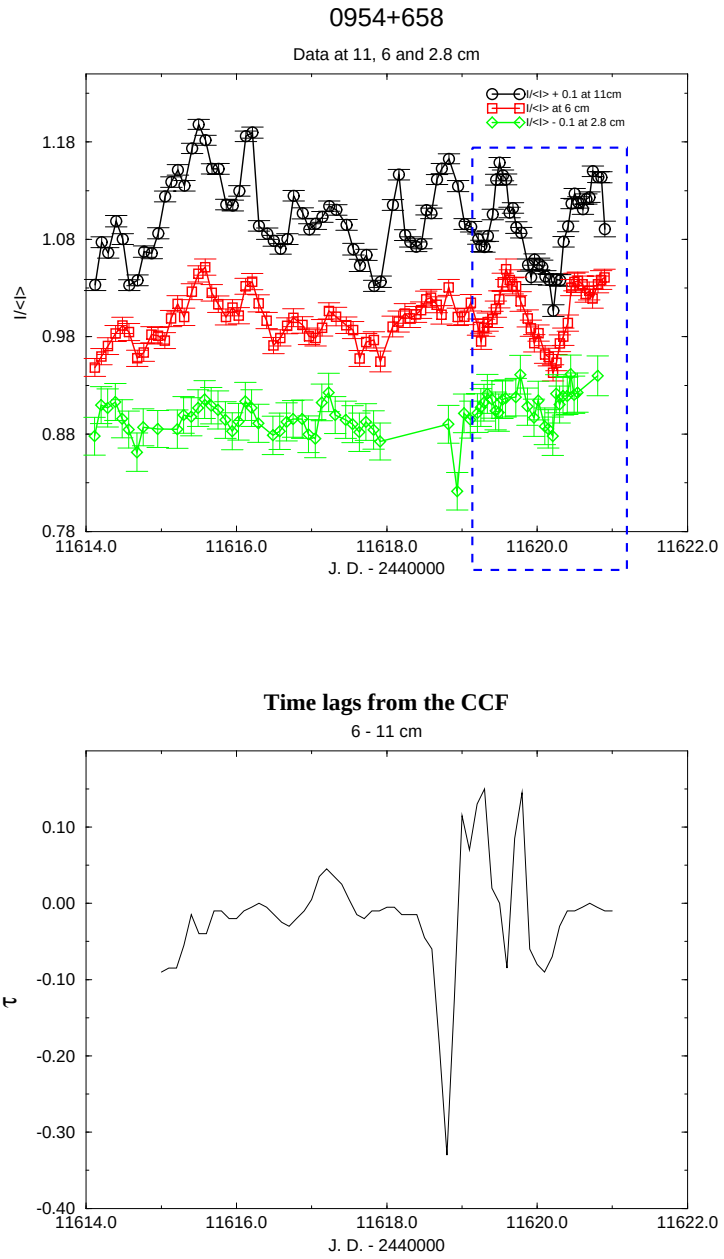

Figure 6.1: *Top:* Light curve of 0954+658 at 11, 6 and 2.8 cm. The dashed box highlights the ESE-like event. *Bottom:* Running Cross Correlation Function (CCF), where we plot time lags versus time. We were not able to perform a proper CCF analysis for the last few hours of the event because it occurred at the end of our observing period.

6.1 Analysis of the time series

The light curve of 0954+658 (fig. 6.1) shows the characteristic pattern of a type II intraday variable. The variations have a typical peak-to-peak amplitude of$\sim$ 12% at

11 cm and a characteristic time scale of 1.3 days. The amplitude of variability decreases with the wavelength, as expected by the RISS theory. However, we note two different behaviors regarding the time scales at the three observing frequencies. The first part of the data set (J.D. 2451614 – 2451619.5) does not show any time lag among the three frequencies while in the last part we measure rapid and (in time) delayed changes. At J.D.$\sim$ 2451619.6, we observe a systematic time lag, in the sense that the flux density at longer wavelengths peaks before the flux density at shorter wavelengths ($t_{11\,\mathrm{cm}} < t_{6\,\mathrm{cm}} < t_{2.8\,\mathrm{cm}}$). At J.D.$\sim$ 2451621.8, the situation reverses and the shorter wavelength peaks before the longer wavelength.

To check whether this systematic time reversal is real, a running cross correlation was performed, i.e. time lags between 11 and 6 cm versus time was calculated (see fig.6.1, *bottom*). The time series was binned in time intervals of 0.3 days and for each bin the time lag corresponding to the maximum of the cross-correlation coefficient between the frequencies was evaluated. The first part of the plot showed a flat pattern (centered at zero) indicating no time lag between 6 and 11 cm. During the last 2 days of observations, however, a different behaviour was seen. This again indicates that after J.D. 2451619.6, the variability pattern and the time lag between the frequencies must have changed.

Furthermore, an analysis of the polarization gives evidence for a difference in the variability patterns at different frequencies: we noted that the polarized flux density and the polarization angle variations after J.D.$\sim$ 2451619.6 are more pronounced and faster than before. Using a structure function analysis, we were able to quantify this change in the polarization characteristics of the source. The results are shown in figure 6.2, where we plot the structure functions for two different time intervals at 6 cm. The typical time scale of the variations changes from ≥ 1.5 to $\sim$0.4 days.

The time reversal phenomenon could also appear in weak scattering by random variations in the frequency dependence pattern of RISS (Rickett priv. communication). Here we suppose that the reversal of time lags is caused by changes in the optical depth of a single cloud in the ISM. Such an interpretation is supported by the observed variability pattern which resembles an extreme scattering event, but on much shorter time scales, $t_{ESE} \sim 2$ days, than the one seen earlier on the same source by Fiedler et al. (1987), $t_{ESE} \sim 8$ weeks (see next section for a description of the ESE characteristics).

Also, the sudden change in the polarization characteristics is a further indication of some peculiar event occurring after J.D. 2451619.5.

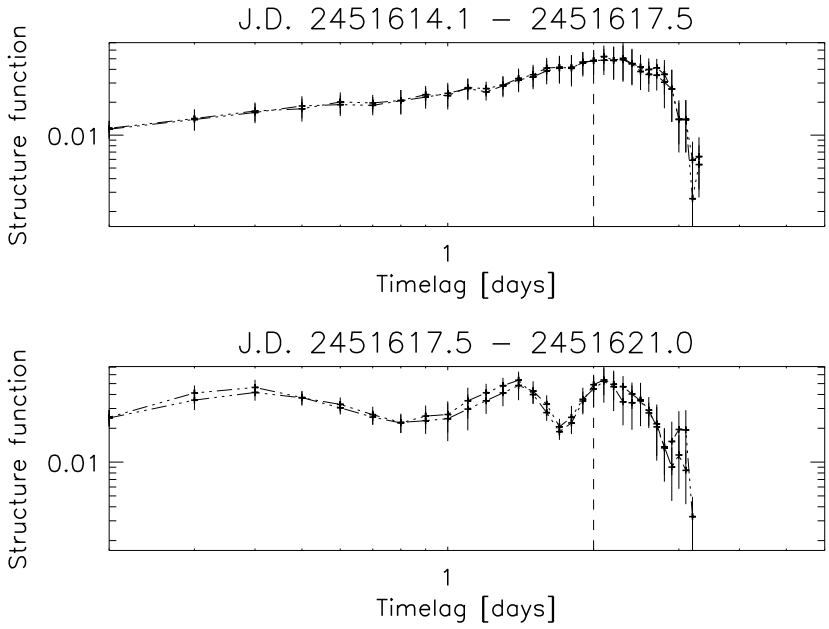

Figure 6.2: Structure functions of the polarized flux density. The *upper curve* corresponds to half of the time series where the usual variability behaviour is present. The *bottom curve* shows the SF for the second half where the ESE-like pattern is seen in the total intensity signal.

6.2 The Extreme Scattering Event phenomenon

An extreme scattering event is a flux density variation caused by ray path distortions within an isolated inhomogeneity ("plasma lens") in the interstellar medium located within the line of sight (fig. 6.3). These events are characterized by a deep minimum with surrounding maxima and have time scales which vary from weeks to months. A characteristic of these events is a well defined frequency dependence: variability indices, time scales, amplitudes of variations and amplitudes of the two surrounding maxima decrease with increasing frequency. Some of these features are similar to normal scattering processes and for shorter time scales it is hard to distinguish between small amplitude ESEs and refractive scintillation. In a statistical description of this phenomenon, Fiedler et al. (1994) suggested that the identification of an ESE is dif-

ficult, if the amplitude and the time scale of the variations are comparable to other possible origins of variability. An important difference between an ESE and standard scattering is the focusing which causes the reversal of the time lag: observations showed that in an ESE the flux density rises first at lower frequencies (first maximum). The flux density reaches the minimum at different frequencies simultaneously, then it rises again at higher frequencies first (second maximum). The two bracketing maxima are due to focusing at the edges of the cloud which, basically, acts like a lens.

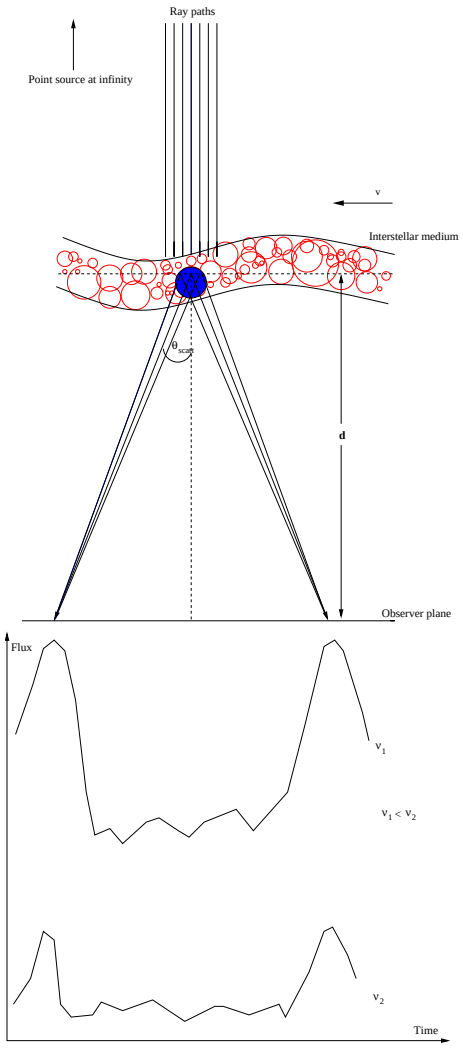

Figure 6.3: Scheme of an extreme scattering event.

6.3 Description of the model

Electron density fluctuations within isolated structures in the interstellar medium along the line of sight to a compact background extragalactic source are responsible for ESE. Such events seem to have a duration of weeks to months and do not appear very frequently. Clegg et al. (1998) developed a plasma lens model describing ESEs and in this work we extend their model to the small lenses generating the very rapid extreme scattering events. The model is described only by two parameters (Clegg et al. 1998):

$$\alpha_s \equiv \frac{\lambda^2 r_e N_0 \mathrm{d}}{\pi a^2} = 3.6 \left(\frac{\lambda}{1\,cm}\right)^2 \cdot \left(\frac{N_0}{1\,cm^{-3}\,pc}\right) \cdot \left(\frac{\mathrm{d}}{1\,kpc}\right) \cdot \left(\frac{a}{1\,AU}\right)^{-2} \quad (6.1)$$

$$\beta_s = \theta_i/\theta_l \quad (6.2)$$

The strength of the scintillation is described by the dimensionless parameterα_s, which is related to the wavelength and to the parameters describing the cloud: the column electron density N_0, the distance d, and the size a of the lens. The parameter β_s indicates the ratio between the apparent angular size of the source and that of the lens. We assumed a Gaussian brightness profile for both the plasma lens and the background source.

We applied this model to the last part of our light curve (box in figure 6.1), where the strong change of the time lag between 11 and 6 cm is seen. Figure 6.4 shows the modeled light curves and the cross correlations that we can immediately compare to our data (fig. 6.5).

6.4 The size of the clouds in the ISM

The table 6.1 shows the values for α_s and β_s used in our calculation. The spatial lens size was evaluated using the equation:

$$a \lesssim v\Delta t \quad (6.3)$$

At 11 cm Δt is 2 days, a lens speed of 30 km s^{-1} would correspond to a size of the lens of 0.035 A.U. Assuming that the lens is at 0.15 kpc (distance of Galactic Loop

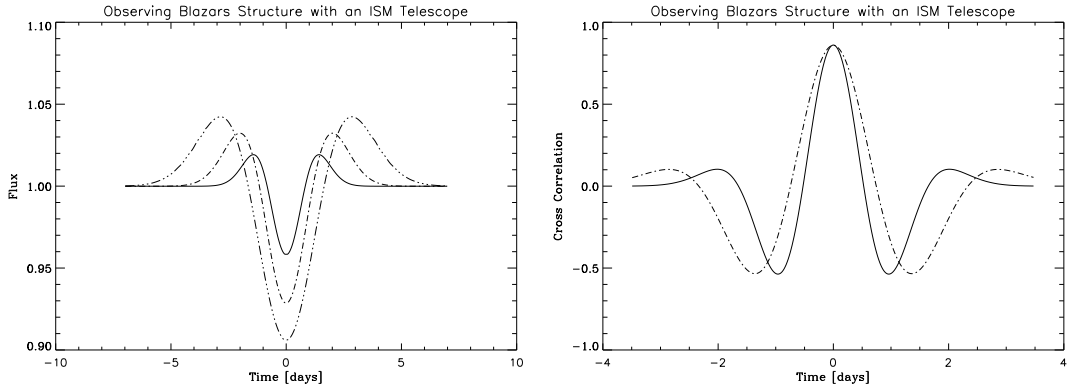

Figure 6.4: *Left:* normalized flux density model of light curves of a very rapid ESE at different frequencies, respectively: 11 cm (dotted line), 6 cm (dashed-dotted line) and 3 cm (solid line). *Right:* cross correlation functions for the model light curves for a very rapid ESE between 11 and 6 cm (dotted line) and between 6 and 3 cm (solid line).

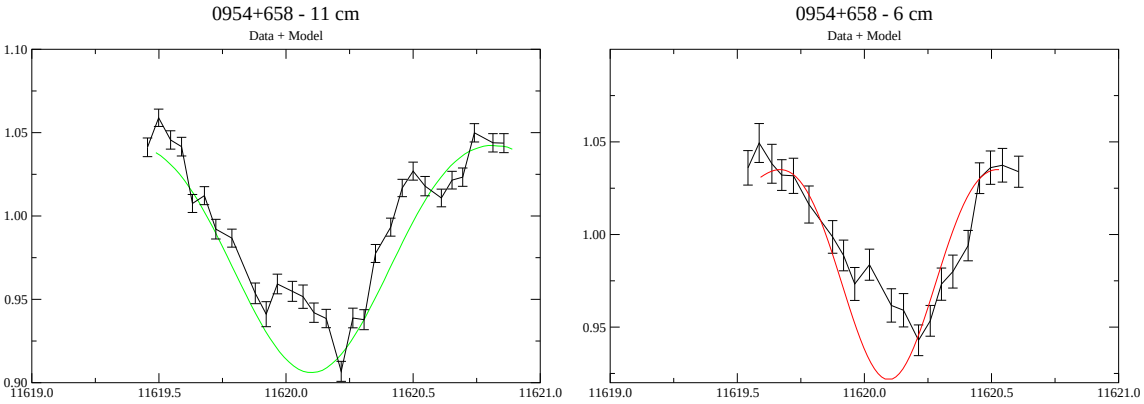

Figure 6.5: Models of the normalized flux densities and normalized data: 11 and 6 cm

III, direction close to the line of sight to 0954+658) we can evaluate the density of the plasma lens: $N_0 \approx 1.875 \cdot 10^{-5}$pc cm^{-3} and $n_e \approx 110.95\,\mathrm{cm}^{-3}$. For the standard Kolmogorov size distributions in the ISM (see 5.1), such structures are still physically reasonable, but they put new constraints on the clumpiness of the interstellar medium. Discussing the ESE in 1981, Clegg et al. (1998) derived (at 2.25 GHz and assuming the same distance) a lens size of 0.38 A.U.: **Thus the size of the lens derived here is 10 times smaller.**

It is therefore likely that the ISM has also a clumpy component, in addition to the "smooth" large scale distribution (with scale heights $h_1 = 500\,\mathrm{pc}$ and $h_2 = 100\,\mathrm{pc}$ as described by Cordes et al. (1988) using pulsar measurements). These "clumpy"

components have probably a low filling factor. The detection of this rapid ESE in 0954+658, together with the earlier detection of a slow ESE suggests that the size of these plasma lenses could be very different, at least by a factor 10. It is therefore not unlikely that the ISM is filled with such clouds in a inhomogeneous way.

λ	6 cm	11 cm
α_s	0.2980	1.00
β_s	0.90	1.450

Table 6.1: Parameter of the model from the data.

Part IV

Towards Higher Frequencies

Chapter 7

86 GHz observations at Pico Veleta

The theory of the interstellar scintillation and in particular the theory of RISS (see section 1.3) is capable of describing the rapid variations of compact objects in the centimeter regime. Since the amplitude of RISS decreases with λ^2, observations in the mm-band can be useful to disentangle source-intrinsic and propagation effects in the observed variability. Claims for detection of rapid variations at high frequency were presented by Wagner (1998) and Krichbaum et al. (2002) at 32 GHz. The detection of rapid variability at mm-wavelengths is difficult, and in particular the calibration is less accurate because of the strong weather influence: during our measurements, an accuracy of $\sim 5\,\%$ was achieved. Thereupon tests were performed on well suited sources (mainly 0716+714) to check whether IDV measurements (in total intensity and polarization) were at all possible at millimeter wavelengths. This chapter will describe the high frequency data measured at the IRAM 30-m telescope located in Pico Veleta at an altitude of 2920 m in the Spanish Sierra Nevada near Granada. The 30-m telescope, a Cassegrain-Nasmyth system with an altazimuth mount, was built following the homology principle (see section 2.3) and has a thermally insulated backup structure of the primary mirror. Moreover the temperature homogeneity of the panels is kept within 1 ° Celsius, via an active control system.

The main reflector surface has an accuracy of $70 \pm 5\,\mu$m.

Two observing campaigns (see table 7.1) were carried out in May 2001 (polarimetry experiments) and October 2002 (total intensity monitoring) using the 3 mm heterodyne receivers of the IRAM 30-m telescope. Two SIS (*Superconductor-Insulator-Superconductor*) receivers (A100 and B100) were used simultaneously in our experi-

ments. They work at intermediate frequency ($\nu_{IF} = 1.5\,GHz$) and can be tuned for continuum and line observations in the range of 80 – 115.5 GHz. In general we have:

$$\nu_{obs} = \nu_{LO} \pm \nu_{IF} \tag{7.1}$$

where $\pm$ defines the upper/lower bands to which a heterodyne receiver is sensitive. The ν_{LO} is the frequency of the local oscillator used to reach ν_{IF}.

7.1 The fast monitoring of 0716+714

The tentative detection of fast variability at 9 mm on 0716+714 with the Effelsberg 100-m radio telescope in 1998 (Krichbaum et al. 2002) initiated additional studies at 3 mm. During $3^{rd} - 4^{th}$ of October 2002, dedicated observations of this object were carried out in Pico Veleta at 86 GHz. The source was observed during these two consecutive nights, (~ 2 hrs per night) together with the secondary calibrator 0836+710. The telescope beam at 86 GHz is $28''$ and our sources were point-like and strong enough to be observed with cross-scans (see section 2.3). All our sources are part of the IRAM pointing catalogue for the 30-m telescope.

The command for a cross-scan is POINTING, a task which includes before each observation a calibration scan (CAL COLD). The CAL COLD scan measures the temperature of the sky and two loads (cold and warm) of known brightness temperature and calculates τ_{sky} (the sky opacity) using an atmospheric model (Pardo et al. 2001).

Earlier measurements suffered from intrinsic changes with the parallactic angle, since the source were observed with linear polarized feeds. Therefore, during the observations in October 2002 (the total intensity experiment), a quarter wave plate was inserted in front of the receivers. In this case, the receivers handled with the circular polarization

POL Experiment	May 2001	TOT Experiment	Oct 2002
Source	N	Source	N
0716+714	9	0716+714	28
0836+710	11	0836+710	25
1803+784	18	0954+658	7
		1044+719	7

Table 7.1: Summary of two IDV experiments carried out in Pico Veleta. N is the number of the observations for the given source.

components of the radiation (instead of the linear components). Usually such plates are used during the mm-VLBI experiments. Here it makes the polarization measurements independent of the variations of the parallactic angle.
The data were reduced using the program CLASS, a software of the GILDAS package (Grenoble Image and Line Data Analysis System) of IRAM, in the continuum mode. CLASS (Continuum and Line Analysis Single-dish Software) reads the telescope output file containing the measurements already calibrated (including the gain correction and the conversion factor temperature-to-Jansky) and makes an average of all the subscans. Finally, a Gaussian is fitted to this averaged scan.
To check the quality of the results, primary (eg. planets) and secondary calibrators were observed at regular intervals. In particular, a secondary calibrator was always observed after a program source. Due to the relevant influence of the weather conditions in the observations at mm-wavelengths, a calibration uncertainty of $\sim 5\%$ was achieved, which is larger than the $0.5 - 1\,\%$ obtained at cm-wavelengths.

7.1.1 Results

The source was observed with a very dense time sampling: one cross-scan every 3 minutes for the program source as well as for the calibrator. The light curves are plotted in figure 7.1. In both nights, we have marginally detected variability at $10\,\%$ level in 0716+714 with very small time scale of ~ 15 minutes. The uncertainty on the variability was derived from the modulation index of the calibrator $m_0 = 4\,\%$. The consistency of these variations was tested with a formal χ^2 test: it resulted $\chi^2_{red} = 0.77$, which gives only $25\,\%$ probability for 0716+714 to vary during the observing period. However, it is important to note that during this year the source showed a prominent outburst in the millimeter regime on longer time scales (see fig. 7.2). We may speculate once more (see chapter 4) that when a source is getting very bright, the rapid variations are quenched by physical changes (i.e. changes of size, ejection of new VLBI component) occurring in the radio core. This may have caused the low variability seen in this 3 mm experiment.

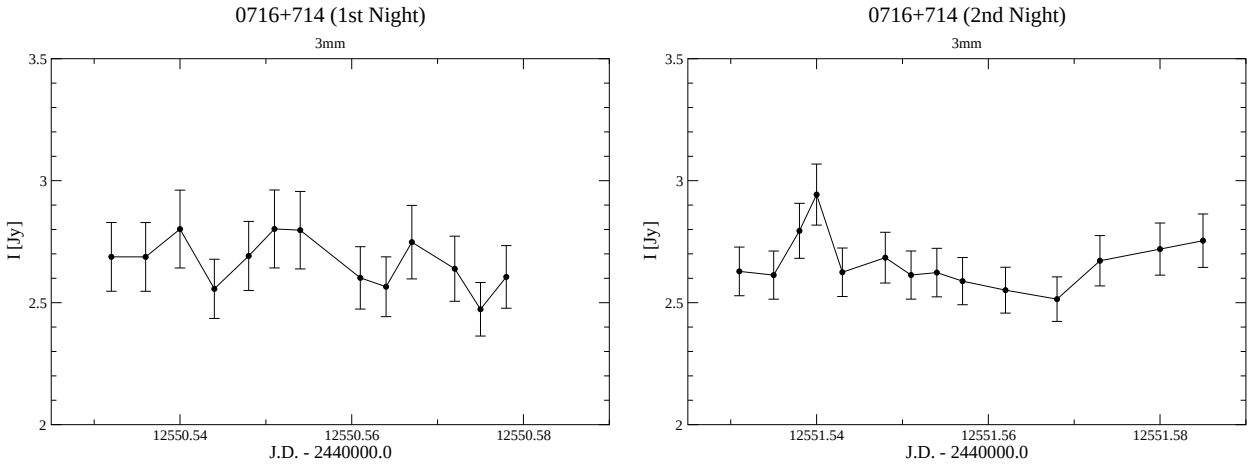

Figure 7.1: 0716+714 measured at 3 mm in October 2002 with the IRAM 30-m telescope.

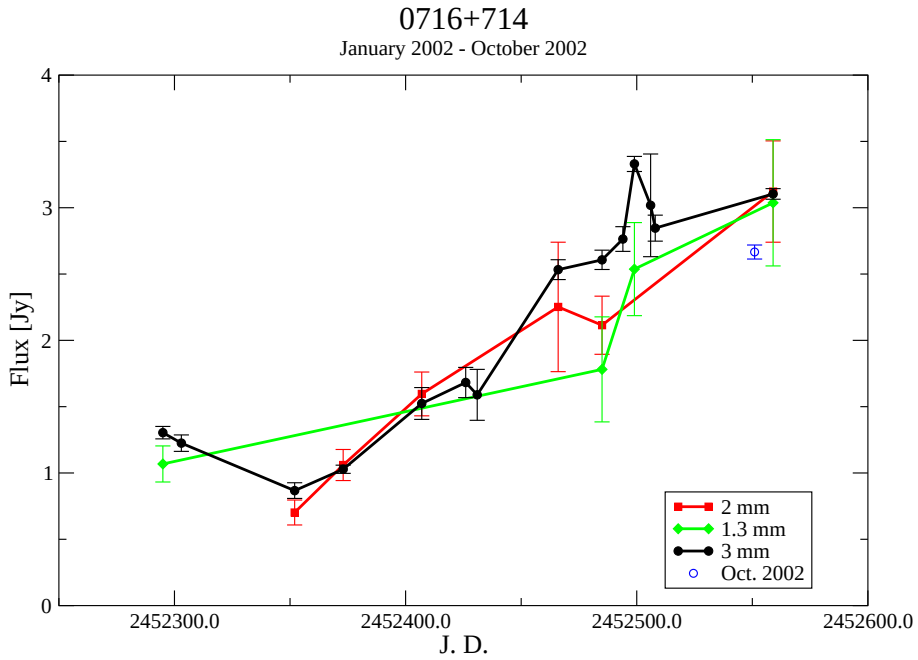

Figure 7.2: Long term variability of 0716+714 in the millimeter regime (IRAM pointing sources monitoring).

7.2 The experiment on the polarization variability of 0716+714

In a second observing campaign at 3 mm, we looked also for polarization variability in this regime.

The polarimeter (Thum et al. 2002) is designed for narrow band (40 MHz) line and continuum polarimetry. The radiation from the two orthogonally polarized receivers,

A100 (vertical component) and B100 (horizontal component), is fed to the polarimeter which generates four output signals (S1, S2, S3, S4). An autocorrelator combines the two original linear polarized signals from the receivers (S5, S6). With the four polarimeter outputs all four Stokes parameters can be derived.

- Using the polarimeter:

$$I = \frac{1}{2}(S1 + S2) = \frac{1}{2}(S3 + S4) \tag{7.2}$$

$$U = \frac{1}{2}(S1 - S2) \tag{7.3}$$

$$V = \frac{1}{2}(S3 - S4) \tag{7.4}$$

- Bypassing the polarimeter:

$$I = S5 + S6 \tag{7.5}$$

$$Q = S5 - S6 \tag{7.6}$$

The ON-OFF technique is suitable for weak objects and it was used for the polarimetry project since small polarized flux densities were expected. The telescope integrates alternatively ON source and OFF source to take into account and subtract the atmospheric effects. The integration time depends on the weakness of the sources following eq.(2.5). In both ON and OFF phases, the wobbler was on with a frequency of 0.25 Hz: the sub-reflector points to a different part of the sky improving the signal to noise ratio of the observations and the quality of the baseline of the individual scans.
Observations of unpolarized calibrators (eg. HII regions, planets, etc...) were used to measure and correct for the instrumental polarization. The data reduction was done using special CLASS procedures developed by C. Thum and H. Wiesemeyer (IRAM-Grenoble) and slightly modified for our purpose. Each ON-OFF is reduced by finding the mean value of the ON-source flux density and subtracting the OFF subscans. Then all the Stokes parameters (I, U, Q, V) were calculated and corrected for the instrumental polarization. Finally, for a single scan the procedures evaluated the Julian date of

the observation, the polarized flux density, the percentage of polarization, the polarization angle and the respective errors.

Thum et al. (2002) detected linearly polarized flux density at 3 mm on strong ($S_{3\,\mathrm{mm}} \sim 1 - 10\,\mathrm{Jy}$) active galactic radio sources. Aim of our experiment was to measure linear polarization and its possible variability also on weaker sources ($S_{3\,\mathrm{mm}} \gtrsim 0.5\,\mathrm{Jy}$).
The program source 0716+714 and the calibrators were observed for 24 hours. Unpolarized non-variable objects were used as primary calibrators and the polarized non-variable quasar 0836+710 was observed with a very dense time sampling to provide an accurate secondary calibration for the linear polarization. A preliminary analysis of the data (fig. 7.3) shows peak-to-peak variations of the polarization degree at a 34 % level in 0716+714 (the mean value is $< p >= 2.2 \pm 0.1\,\%$). In 0836+710 the observed polarization degree seems to be constant, for most of the observing session, with the value of $< p >= 4.0 \pm 0.1\,\%$.
Further data analysis and tests are still necessary to check whether the fast variability observed on the light curve of 0716+714 is due to intrinsic variability or external biases (i.e. systematic effects caused by receivers, feeds or the weather). If a detection of polarization variability could be confirmed, it would be the first case of intraday (polarization) variations observed in the millimeter regime.

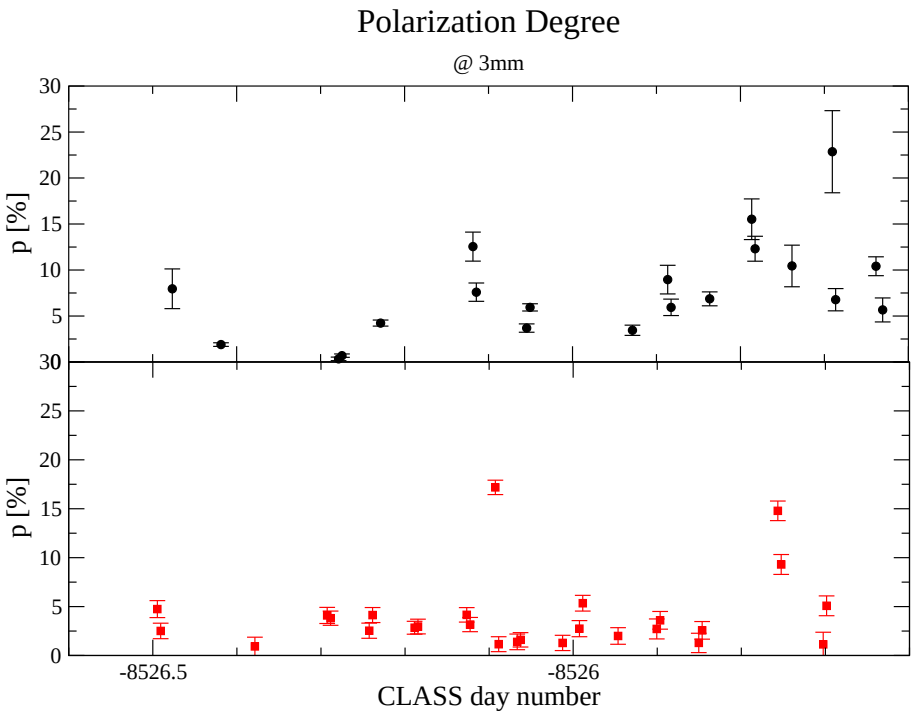

Figure 7.3: Linear polarization measurements (preliminary results) at 3 mm. The *top panel* shows the polarization degree of 0716+714. In the *bottom panel*, the polarization degree of the calibrator 0836+710 is plotted.

Chapter 8

345 GHz observations at the Heinrich-Hertz-Telescope

In this chapter, our experiments at the Heinrich Hertz Sub-Millimeter Telescope on Mount Graham (Arizona, USA) are discussed. In January 2002, first test measurements on polarization in the sub-mm regime (in collaboration with the MPIfR Bolometer group) were carried out at the Heinrich Hertz Sub-Millimeter Telescope (HHT) of the Steward Observatory using the MPIfR 19-channel bolometer array (at 345 GHz) with the ON-OFF technique. Furthermore at the HHT using the 19-channel bolometer, in May 2002 a monitoring project of flat-spectrum radio sources was carried out within a radio-submillimeter-optical campaign (see section 8.2.1).

8.1 Sub-Millimeter IDV monitoring of AGNs

The HHT is part of the Sub-Millimeter Observatory (SMTO) facilities and it is located at an altitude of 3186 m (10453 feet) on Mount Graham about 250 km north-east from Tucson in Arizona (USA). The telescope with diameter of 10-m, is an altazimuth mounted paraboloid with Nasmyth focus. The dish surface accuracy is better than 12 μm. The observing range in elevation is limited by the trees that surround the dome: in some directions, it is possible to observe only at elevation higher than35°. The MPIfR 19-channel bolometer array (Kreysa et al. 2002) consists of 19 individual continuum receivers sensitive around the wavelength of 0.87 mm (345 GHz). The array is arranged in two concentric hexagons around the central bolometer (fig.8.1). The azimuth distance between two adjacent channels is about50″ and the maximum beam

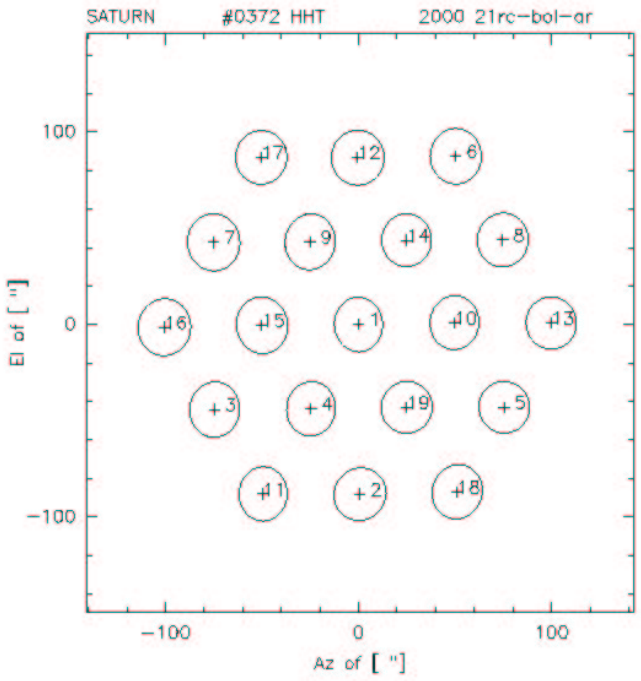

Figure 8.1: The array geometry at an elevation of 0 degrees. For increasing elevations, the image of the whole array rotates counterclockwise.

separation about 200″. Usually, a point-like source is observed with the central horn while the outer channels collect only the radiation of the surrounding sky.

At high frequencies, the measurements are very sensitive to atmospheric variations. Different methods are used to take into account the effects of the sky turbulence. Throughout all the measurements a 2 Hz wobbler was running and the ON (or OFF) signal collected by the backend is the result of an instantaneous subtraction of the empty sky seen with the wobbler. With the ON-OFF technique we can get rid of longer term sky noise. Furthermore, an event observed at the same time by all the bolometers has to be considered spurious as only the central horn points on the source. This is the so-called *correlated noise* and can be removed during the data reduction.

For the data reduction, the program NIC (a GILDAS software) was used. To obtain the actual value for the flux density, for each scan, NIC:

- calculates the mean and the variance of each single subscans

- removes the baseline of each ON-OFF pair of subscans
- removes the correlated noise
- subtracts from the central channel the weighted average of the outer channels[1]
- estimates the final errors.

Finally, the signals of each channel are corrected for the opacity: at sub-millimeter wavelengths, the sky opacity is relevant and it has to be carefully considered in the correction of the data. The atmospheric opacity (τ_{sky}) was calculated using the SKYDIP scans that measure the sky emission T_{sky} at different air masses $A = \sec Z$ (where Z is the Zenith angle equal to 90−elevation). We have:

$$T_{sky} = T_{atm}(1 - e^{A \cdot \tau_{zenith}}) \tag{8.1}$$

T_{atm} is the temperature of the atmosphere and τ_{zenith} is the opacity at the zenith. The slope of a least square fit of the T_{sky} at different air masses gives τ_{zenith}. Such operations were computed using NIC and MOPSI (a mapping software of Robert Zylka, MPIfR) and taking a mean value of the outputs for τ_{zenith} of the two programs. We performed a skydip scan after each measurement, to better sample the sky turbulence (fig.8.2). Strong and compact objects (Ultra Compact HII regions, planetary nebula and planets) of known flux density were observed at 345 GHz to provide the absolute calibration, that is the counts-to-Jansky factor to convert the counts of the bolometer array in physical unit (Jansky). Again Ultra Compact HII regions, planetary nebulae, planets or strong quasars were observed before and after the program sources: we obtained an overall calibration accuracy of $\sim 10 - 15\,\%$.

8.2 Intraday variability at 345 GHz

The detection of fast variability needs very accurate measurements to disentangle between source-intrinsic variations and instrumental and atmospheric effects. At cm-wavelengths, the influence of the atmosphere is negligible and with a proper calibration, as it is done for the Effelsberg/VLA data, it is possible to reach a very good level

[1] The horns that are inside the OFF-beam are not considered for the calculation of the average.

of accuracy: $\sim 1 - 0.5\,\%$ (see section. 2.3). On the other hand, our measurements at 345 GHz are more strongly affected by the weather conditions. As described in the section 8.1, the achieved calibration accuracy was $\sim 10\,\%$. Under these conditions, only variations larger than $30 - 35\,\%$ can be detected at the 3-σ level.

The observations were carried out from the 30^{th} of April to the 17^{th} of May, 2002. Our sample consists of 33 AGNs and 8 primary calibrators. Due to the large number of objects, only few of them were observed with the necessary time sampling to perform an intraday variability study. Some sources were too weak at 345 GHz at the time of our observations and only one data point was measured to get an estimate of the flux density in the sub-mm regime. The sources were selected from the IRAM pointing sources catalogue, which contains also some well known rapid variable sources from our previous IDV monitoring. The selection was based on the flatness of the millimeter spectra: $\alpha < 0.5$.
In our variability study, we focused on 0716+714. (In appendix B the data for all the

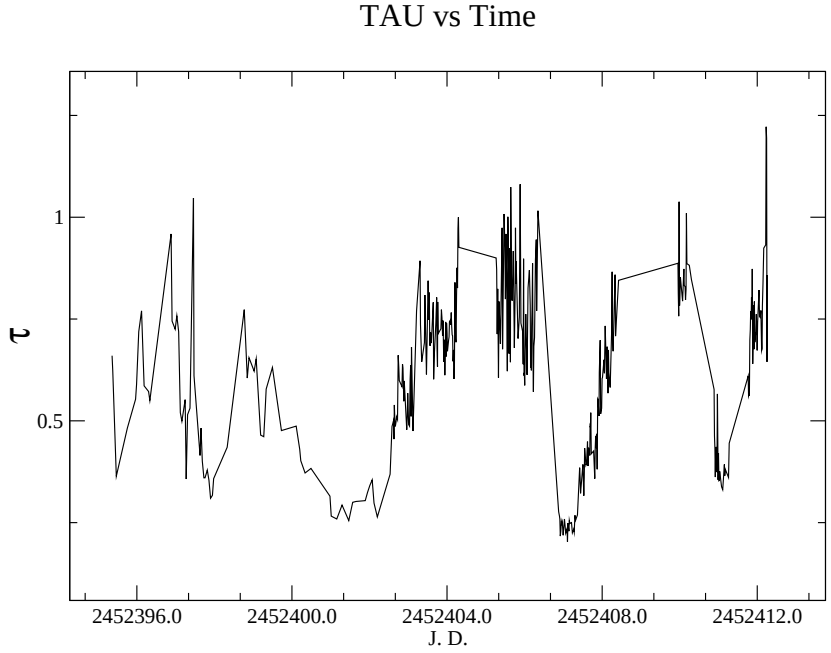

Figure 8.2: Opacity measurements during the May 2002 IDV monitoring session.

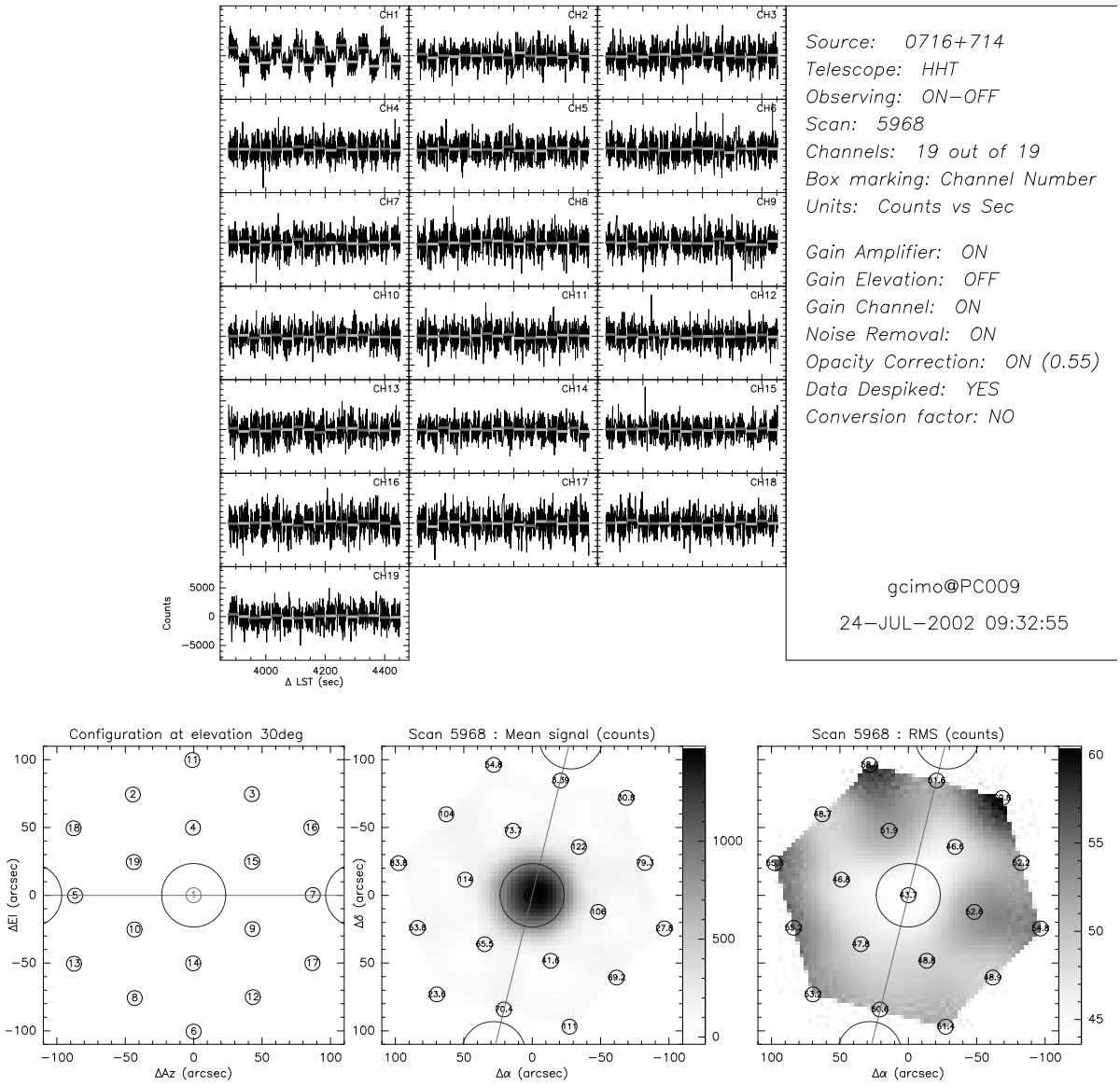

Figure 8.3: *Top:* Plot of the signal of 0716+714 in all the 19 channels. Note in the first channel, the difference between ON and OFF, while in the outer channels only the sky noise is visible. *Bottom left:* The array geometry at an elevation of 30 degrees. *Bottom center:* Total intensity of the 0716+714. Note that the source is seen only by the first channel. *Bottom right:* Noise map in the bolometer array.

program sources and some light curves for other interesting objects are also provided.) Even if the uncertainty of the calibration still is high (due to the atmospheric influence) the measured flux densities of the program source presents variations of the order of 25 % up to 40 % on a time scale of ~ 0.5 days (fig.8.4). Thus, intraday variability of the flux density in the submillimeter regime may be detected: the reducedχ^2 resulted

$\chi^2_{red} = 1.07$, which gives 87 % probability that the observed variations in 0716+714 are consistent with the hypothesis of a variable source. Such variations can not be due to propagation effects and a source-intrinsic scenario should be considered.

Do these fast variations violate the inverse Compton limit?
First of all, to calculate the apparent brightness temperature the luminosity distance[2] is needed (see eq. 1.2). However, the redshift of 0716+714 is not known. Here we use z$\geq$ 0.3 (Wagner et al. 1996). For a variation of 0.4 Jy in 0.5 days we obtain: $T_B \gtrsim 3 \cdot 10^{14}$ K. Thus, only a moderate Doppler factor of $D \gtrsim 7$ is required to avoid the Compton catastrophe. The relativistic beaming which is inferred from such Doppler factor is in agreement with the superluminal (v_{app} up to $11c$) motion seen in this source by Bach et al. (2002).

8.2.1 Comparison with simultaneous Radio and Optical observations

During our observations in May 2002, other telescopes were involved in collecting simultaneous data from different spectral bands, however, with a much looser time sampling. The telescopes involved are shown in table 8.1. From the sub-millimeter data plotted

Optical telescopes

Telescope	Size	Date
Calar Alto	1.23m	30/4 - 17/5
Greve	0.32m	29/4 - 17/5
Vallinfreda	0.50m	29/4 - 17/5

Radio telescopes

Telescope	Date
HHT	30/4 - 17/5, 24h per day
Torun	30/4 - 14/5, 24h per day
Metsahovi	$\sim$ 1 point per week

Table 8.1: Telescopes involved in the May 2002 radio-optical campaign.

[2]For the calculation of D_L we used: $H_0 = 50 \frac{Km}{sec \cdot Mpc}$ and q_0=0.5.

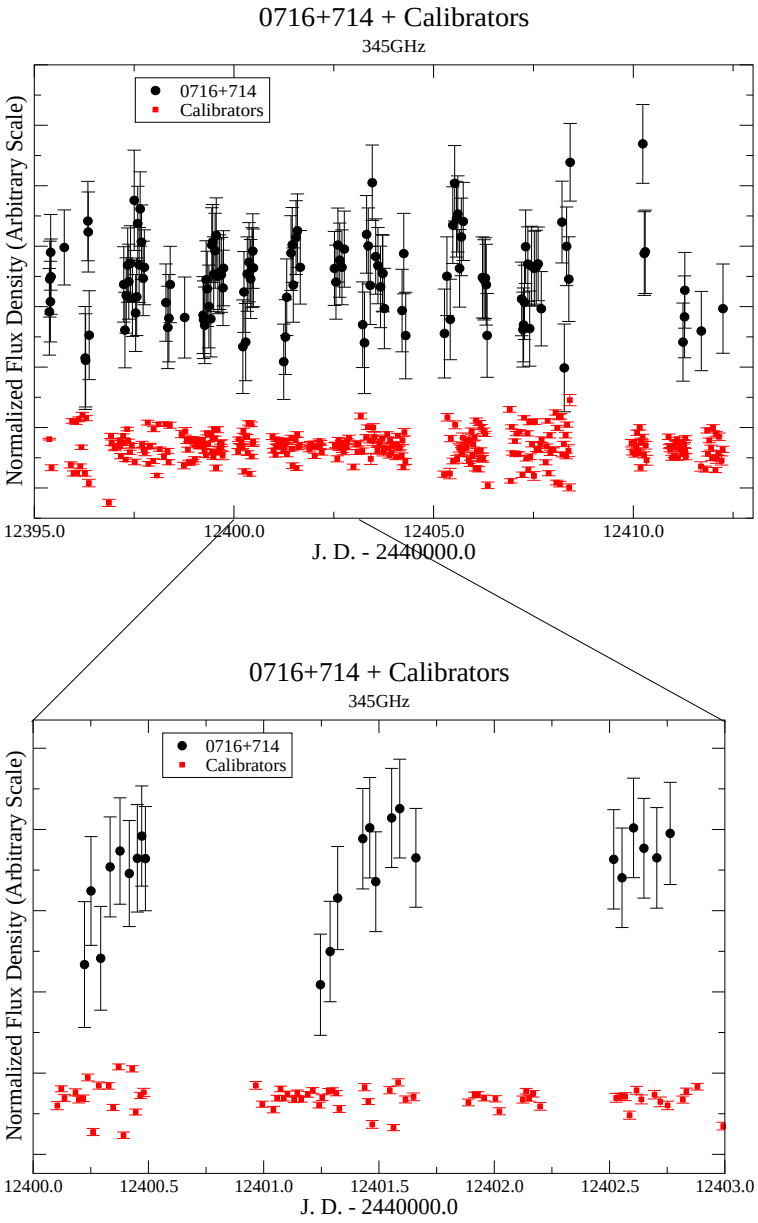

Figure 8.4: 345 GHz light curve of 0716+714 compared to all the observed calibrators.

in figure 8.4 we note that the variability is marginally present only at a 3σ level and a short-term comparison of the optical (fig. 8.5, right) and radio (fig. 8.5, left and 8.6) data is difficult to perform. Anyhow, a long-term variability analysis is still possible but one immediately sees that the observed patterns at different wavelengths only show uncorrelated features: the flux density in the sub-millimeter regime just shows fast variations and a flat long-term behaviour. A typical IDV pattern is visible in the 6 cm light curve and a simultaneous maximum together with the optical data seems to occur around J.D. 2452404. Such a single event is unique and is not supported by

the subsequent radio and optical observations. Finally, high frequency radio observations (fig. 8.6) show a flare starting around J.D. 2452400. Such a behaviour for the broad band properties of the observed IDV sources seems to favor the hypothesis of two different mechanisms causing the variations in the radio and optical spectral bands.

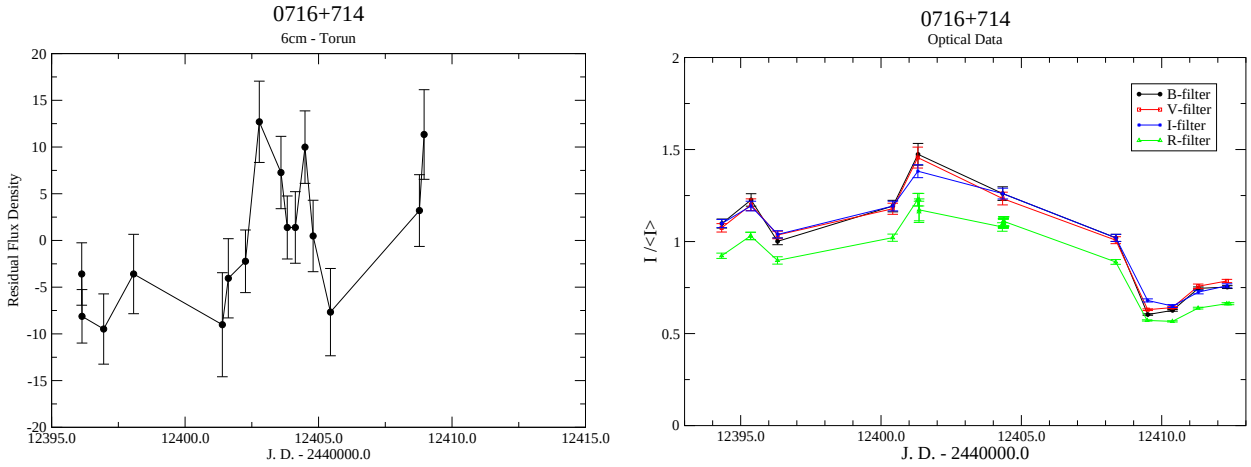

Figure 8.5: *Left:* 6 cm data of 0716+714 (Courtesy of R. Zajaczkowski, Torun center for Astronomy – Poland). *Right:* Optical data (Greve and Vallinfreda) of 0716+714 (Courtesy of R. Nesci, Università "La Sapienza" – Rome). Observations carried out in May 2002.

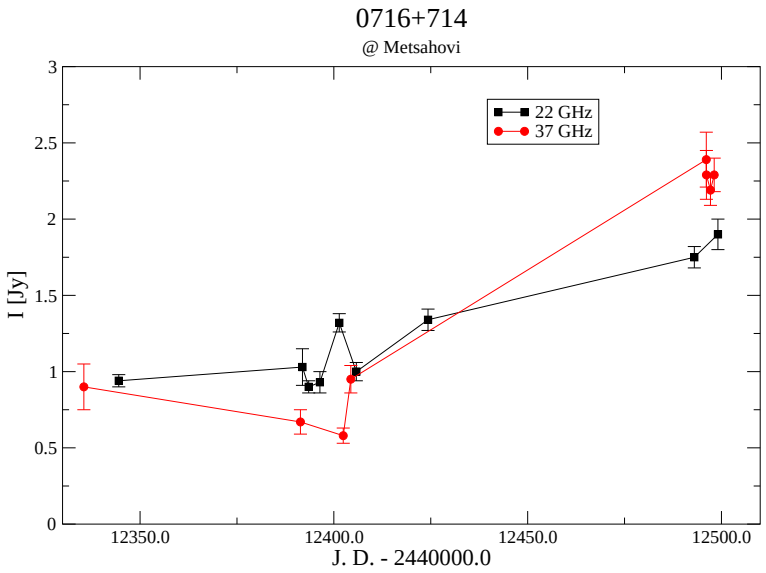

Figure 8.6: Data at 22 and 37 GHz of 0716+714 from Metsähovi in May 2002.

8.3 Polarization measurements

The polarimeter (Siringo et al. 2002) was projected and built by G. Siringo, E. Kreysa and other collaborators of the MPIfR Bolometer Group. It consists of two parts: a rotating (3.5 Hz) half wave plate and an analyzer. The half wave plate is made of a grid of conducting wires placed in front of a mirror. It creates the phase shift between the two component of the polarization via reflection: the radiation is reflected from the wires and from the mirror with different length paths. This half wave plate is mounted in the optical path of the telescope at an angle of 45 degrees. The polarized signal is selected by an analyzer which consists of a wire grid placed in front of the bolometers. The study of the characteristics of the instrument and the procedures for the data analysis are still in progress: details of the instrument and the data reduction are given in Siringo (2003). Our test experiment was successful. First encouraging result is the detection of linear polarization in the radio sources 3C279 and 1633+382. Figure 8.7 shows the polarization degree of these two objects measured by the central channel of the bolometer array compared to the measurements of the outer channels. Further analysis on variability of the polarized flux density is still in progress.

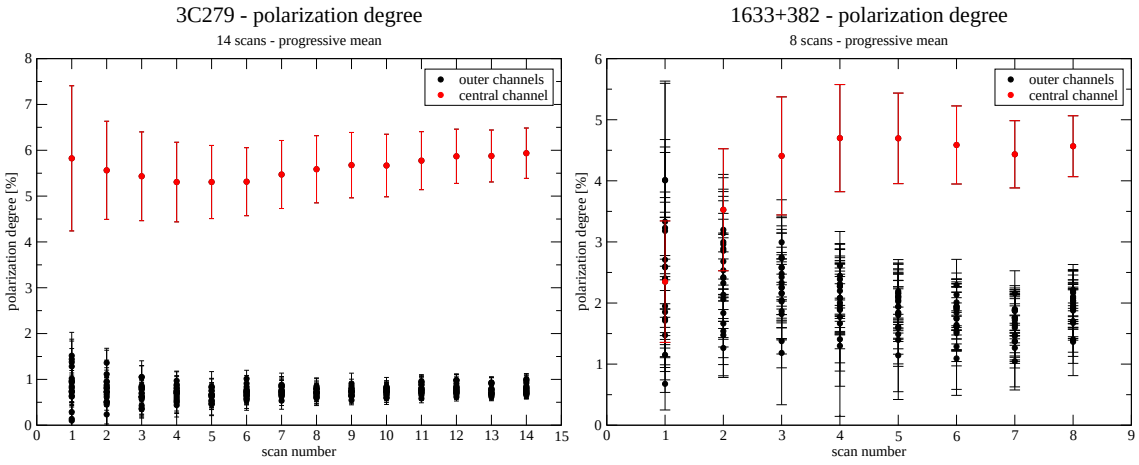

Figure 8.7: Detection of polarized flux density at 345 GHz in 3C279 (*left panel*) and 1633+382 (*right panel*). Courtesy of G. Siringo.

Part V

Conclusions

Chapter 9

Conclusions

The statistical analysis performed in this work has given a new insight on the nature of intraday variability. It was found that intrinsic long-term changes of the VLBI structures in the radio core, eg. emission of new components, could modify the short-term characteristics of flat-spectrum radio sources. Furthermore, the analysis of the polarization indicated a multi-component structure in the jet. Therefore, we propose a mixture of both intrinsic and extrinsic effects as a possible interpretation for the IDV phenomenon: **the rapid variations are caused mainly by refractive interstellar scintillation, but the occurrence and the strength of these variations in total intensity and polarization may be related to the jet structure at μas scale.**

All these findings indicate the existence of a close scattering screen as cause for the intraday variations. Following this interpretation, it was possible **to use the IDV measurements as a tool to evaluate the source sizes and to study the nature of the ISM.** In particular, an upper limit of the size of the scintillating components in the jets can be estimated from the typical time scale of the variability. Moreover, the size of the discrete clouds in the ISM was measured analyzing the time series of the BL Lac 0954+658, from the assumption that the local clouds are responsible for the observed IDV.

9.1 Detailed Summary of the Results

In this work, the occurrence of intraday variations in flat-spectrum radio sources was discussed with respect to the present models.

First of all, **a complete statistical analysis was performed.**
We combined all the Effelsberg and VLA data of the IDV monitoring projects from 1985 up to 2000. Our sample consisted of 32 flat-spectrum radio sources, selected from the 1 Jy catalogue. Intraday variability (of type II) was detected in $\sim 30\,\%$ of all flat-spectrum radio sources.

Galactic dependences of the IDV phenomenon. No strong b-dependence of the strength of variability was found. We argue that the observed features of IDV are not caused by the global distribution of matter in the ISM, but they could be rather due to local clouds which may cause "interstellar weather" and therefore rapid extreme scattering events.

Dependence of the variability on the brightness of the source. A correlation between the amplitude of variations and brightness of the radio source was marginally detected. This could be considered as an indication for larger variability at low flux densities. We suggest that when a new component is emitted from the core, the variability is quenched due to the larger source size.

Redshift dependence. No correlations were found between variability and redshift. However, different IDV characteristics for the same sources was noted at different epochs. The changes of the IDV characteristics with the epoch and the lack of any evidence for a z dependence are further indications of intrinsic structural changes in the observed sources and of a very localized scattering medium.

Spectral index variability. Previous studies predict that sources with steeper spectrum are less variable. We suggest that even very inverted-spectrum sources show less variability due to intrinsically larger source sizes.
Furthermore, we explain the observed intraday variability of the spectral indices with the RISS theory.

Polarization angle variability. We assume that the nature of the observed polarization angle variations lies in the source and we suggest a multi-component structure (Qian et al. 2001) of the innermost regions of the radio jet.

Besides the statistical analysis, we tested the potential of IDV as tool for studying the ISM and the compact structures in the radio cores.

A multi-frequency approach:

We compared statistical models for the RISS to our data and we tried to analyze the mixture of effects causing the rapid variability in active galactic nuclei.

Again, different IDV behaviors of a source, observed at different epochs, was noted. We interpret such effect as due to intrinsic variations of the source size with time. Furthermore, we showed that, in some cases, the variability amplitudes increase towards high frequencies. This is not in agreement with the predictions of the RISS theory.

In the time series of simultaneous observations in different bands of the electromagnetic spectrum (from optical to radio), the observed long-term variability could be explained as a propagating shock, visible at different times in the different regimes. Regarding the intraday variations, no correlated features were clearly detected. Therefore, while the same mechanism could be responsible for the long-term variations, one should consider different processes causing the rapid flux density variations in the different bands.

Determination of the source size via IDV measurements:

Using the model developed by Beckert et al. (2002a), it was possible to reproduce qualitatively the behaviour of the rapid variability in the quenched scattering regime. Furthermore, the size of the scattering region in the core of the compact radio sources was derived. We found that, in case of 0716+714, the scattering component should have a size (at 11 cm) of 121μas for a screen 100 pc distant.

The size of the clouds in the interstellar medium via IDV measurements:

In the BL Lac object 0954+658, we have detected a variability pattern which resembles an extreme scattering event, but on much shorter time scales ($t_{ESE} \sim 2$ days) than seen earlier ($t_{ESE} \sim 18$ weeks). We suggest that a very rapid ESE occurred in this source. This implies 10 times smaller clouds than generally presumed in the ISM.

Detection of IDV at high frequencies:

Test experiments of polarimetry at millimeter and submillimeter wavelengths were performed on the BL Lac object 0716+714. While the total intensity of the source at 3 mm only shows marginal variability, intraday polarization variations were tentatively detected. More detailed measurements will be necessary to confirm this effect.

Moreover, the flux density of 33 AGNs was measured at 345 GHz. In particular, the

flux density of 0716+714 showed peak-to-peak variability at $25 - 40\,\%$ level with time scales of ~ 0.5 days. Such variations are source-intrinsic and can be explained via shock propagation in the jet.

Part VI

Appendices

Appendix A

Effelsberg observations in March 2000

In the following pages, the light curves of the flat-spectrum radio sources observed in March 2000 are shown. In the **top panel**, the total intensity light curve is plotted. The **central panel** shows the behaviour of the polarized flux density. Finally in the **bottom panel**, the polarization angle versus time is plotted.

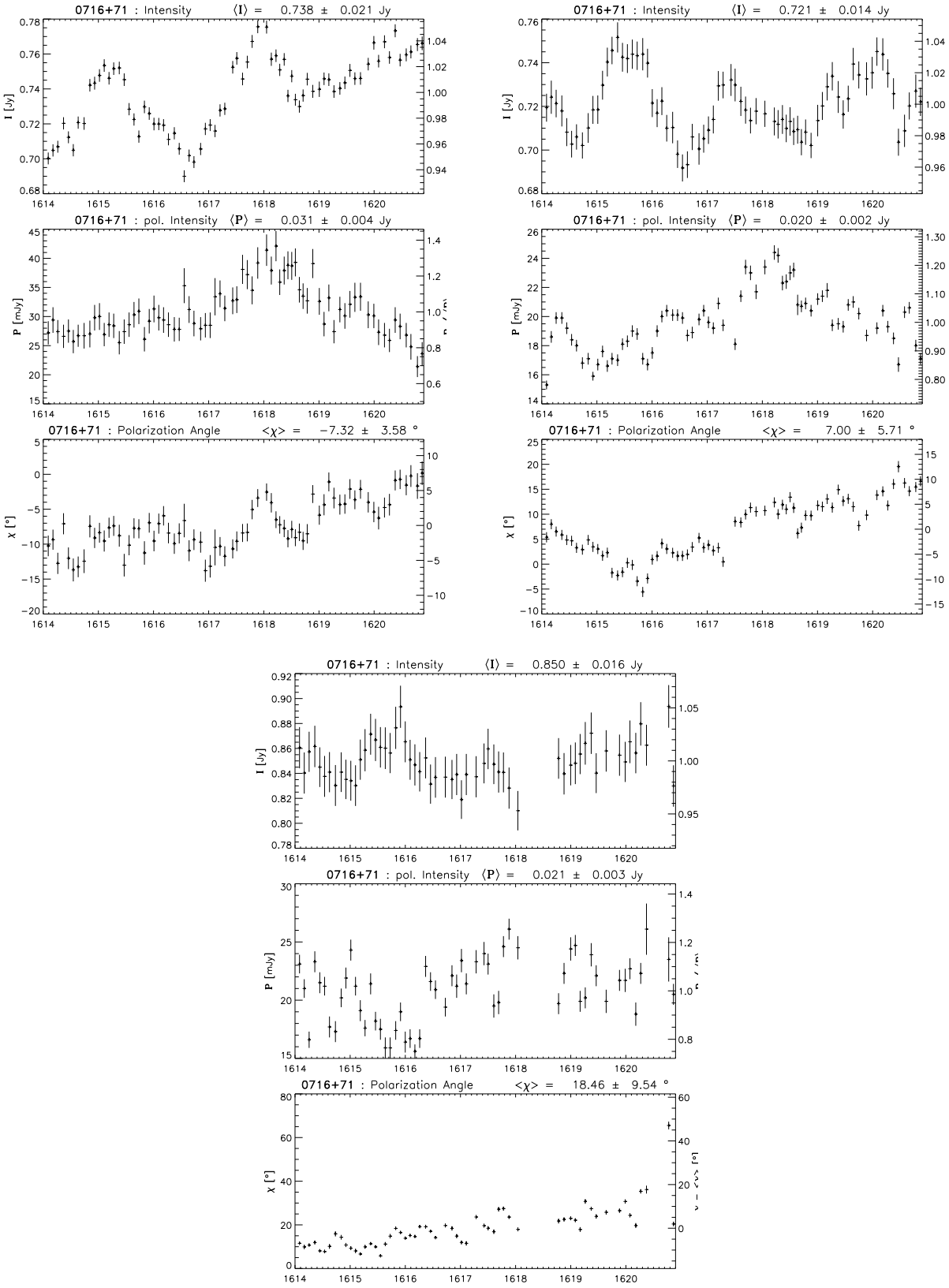

Figure A.1: 0716+71 in March 2000: total intensity and polarization. **Top left:** 11 cm. **Top right:** 6 cm. **Bottom:** 2.8 cm.

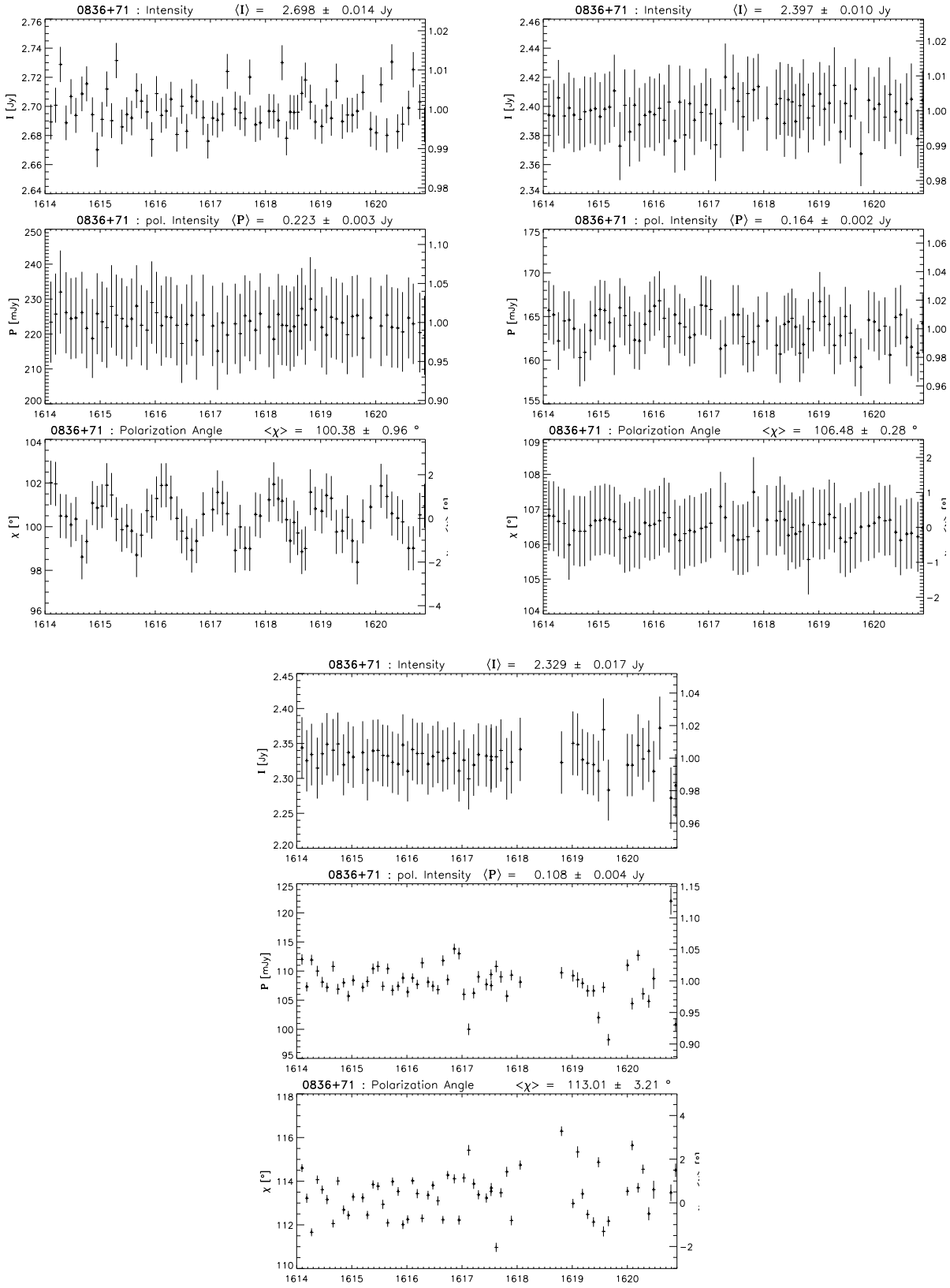

Figure A.2: 0836+71 in March 2000: total intensity and polarization. **Top left:** 11 cm. **Top right:** 6 cm. **Bottom:** 2.8 cm.

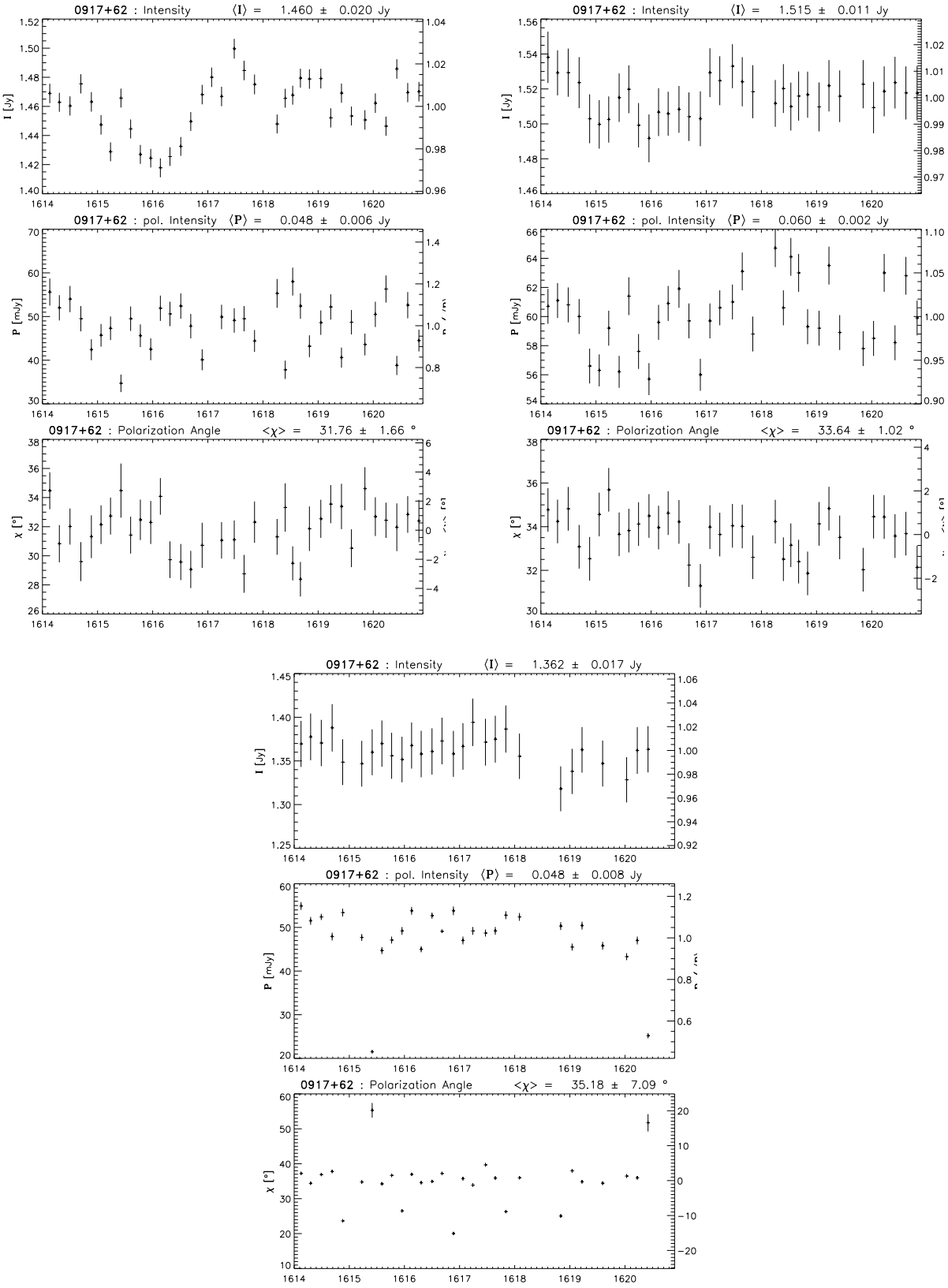

Figure A.3: 0917+62 in March 2000: total intensity and polarization. **Top left:** 11 cm. **Top right:** 6 cm. **Bottom:** 2.8 cm.

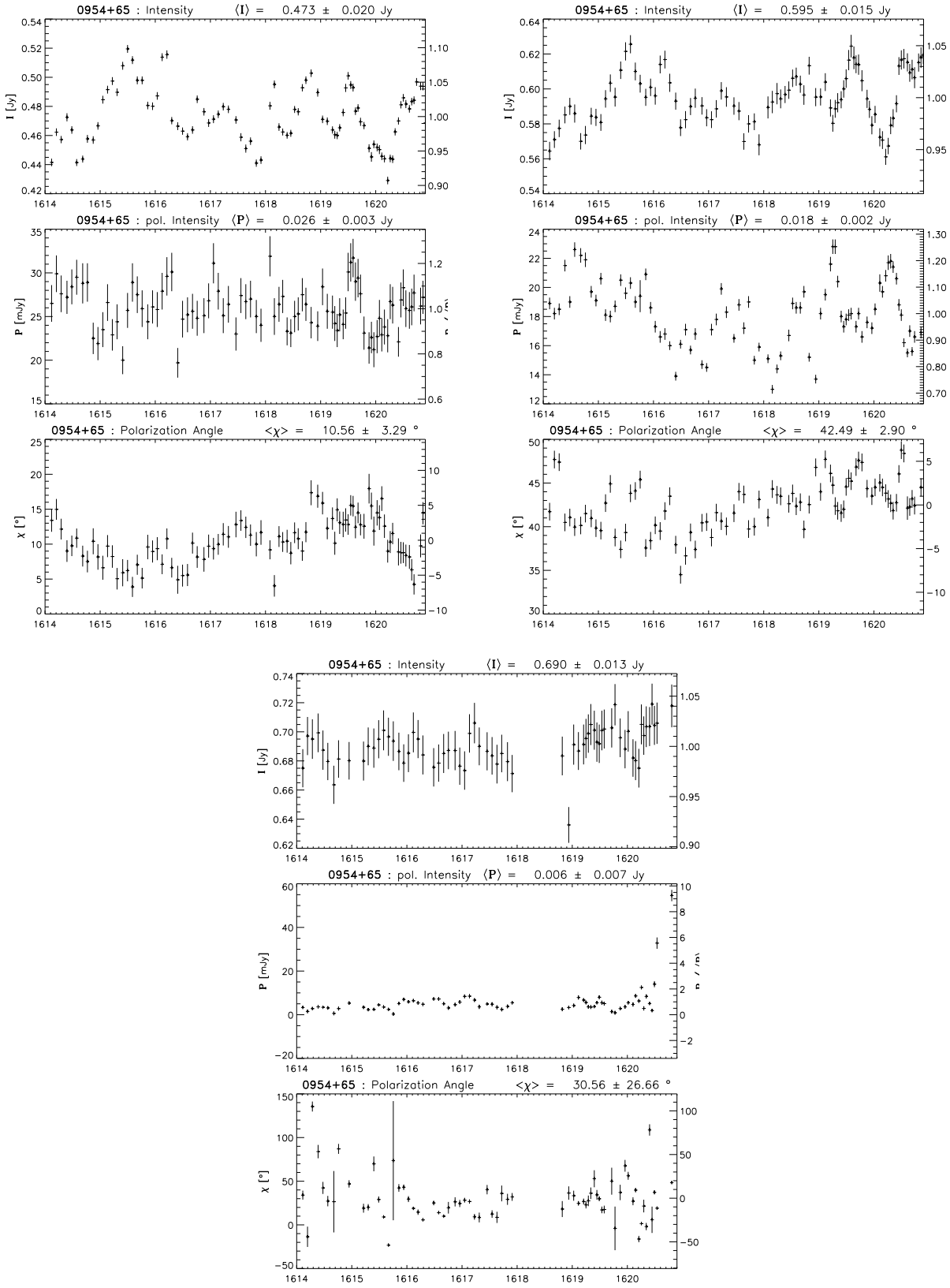

Figure A.4: 0954+65 in March 2000: total intensity and polarization. **Top left:** 11 cm. **Top right:** 6 cm. **Bottom:** 2.8 cm.

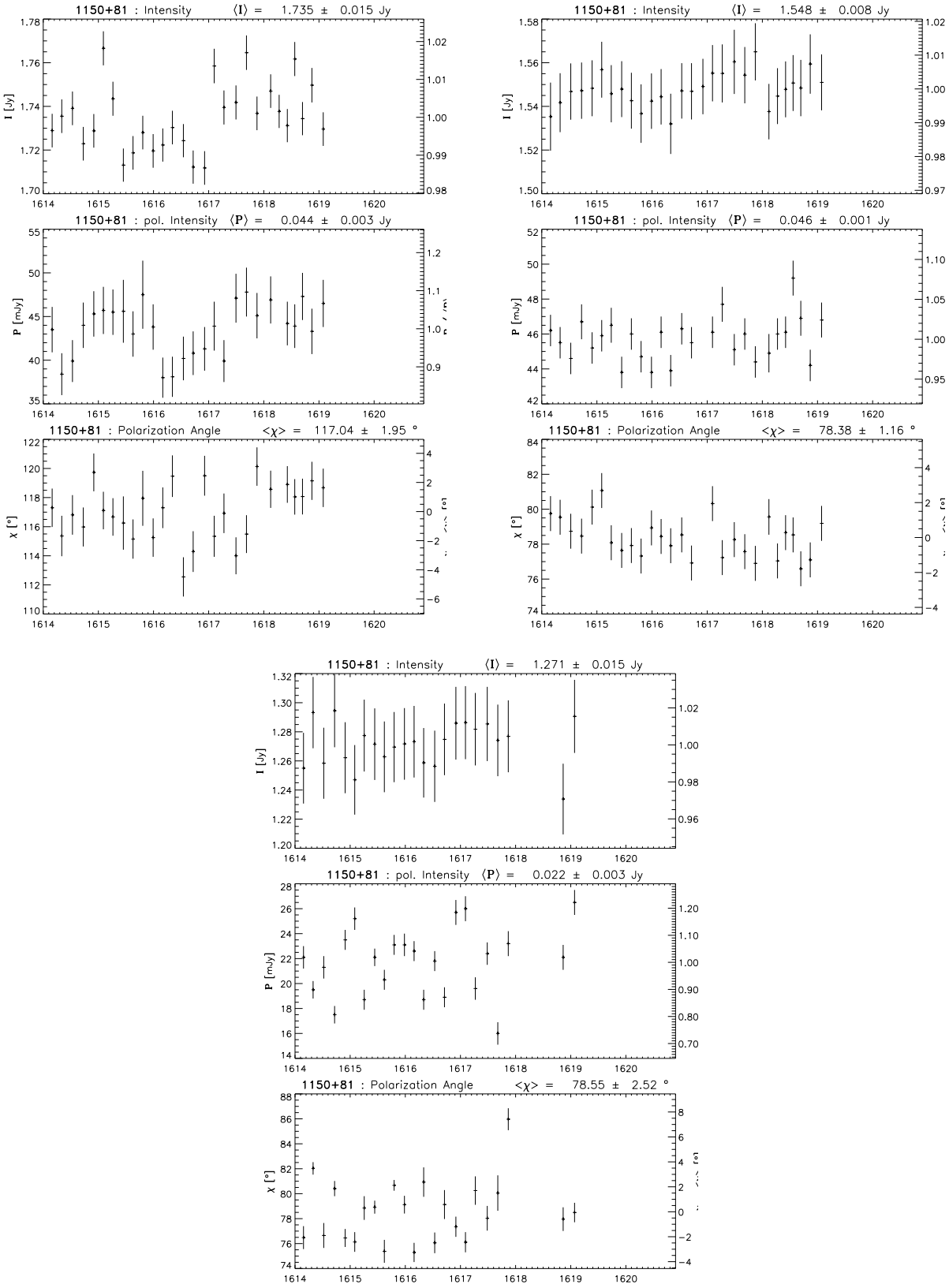

Figure A.5: 1150+81 in March 2000: total intensity and polarization. **Top left:** 11 cm. **Top right:** 6 cm. **Bottom:** 2.8 cm.

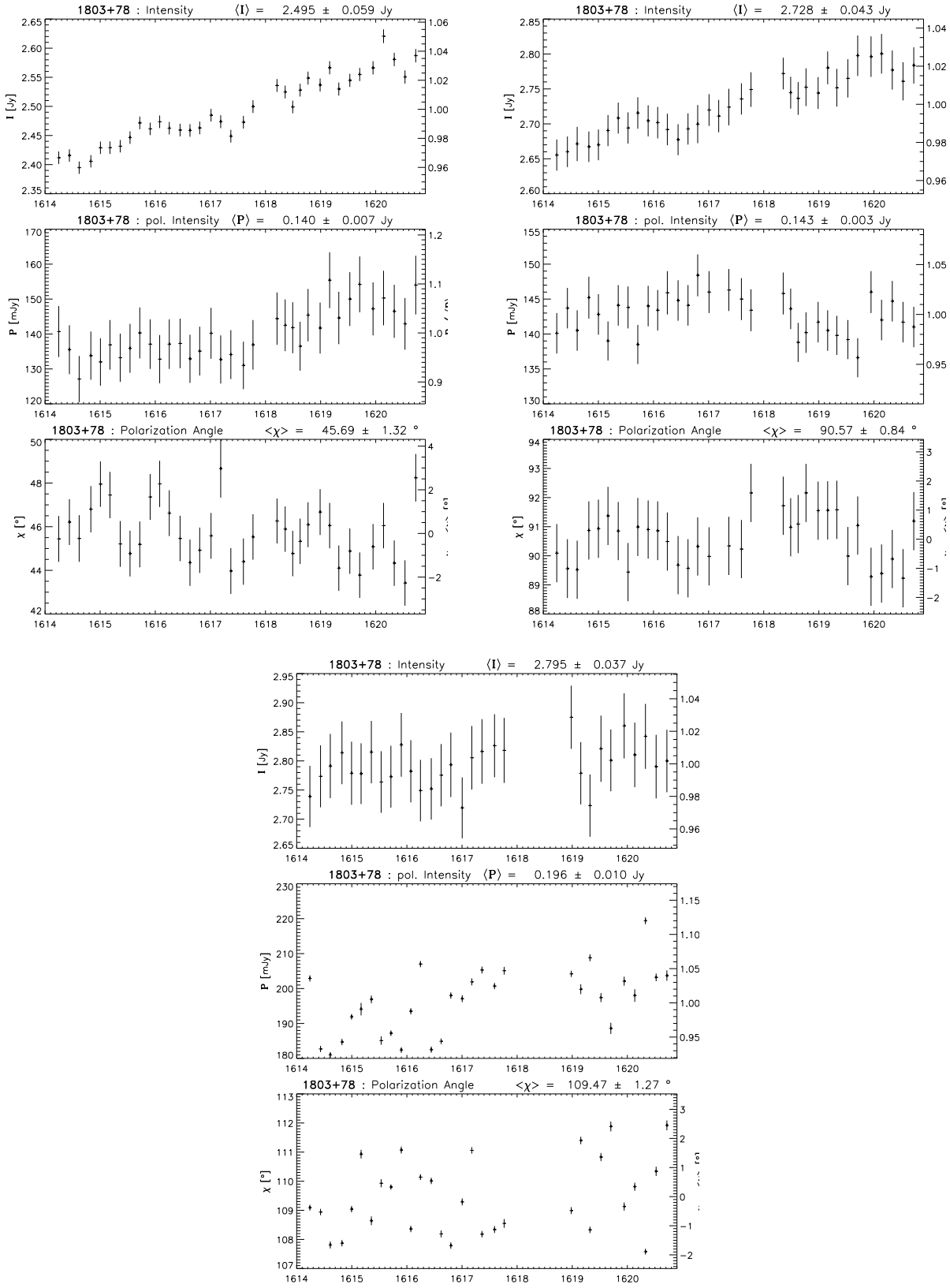

Figure A.6: 1803+78 in March 2000: total intensity and polarization. **Top left:** 11 cm. **Top right:** 6 cm. **Bottom:** 2.8 cm.

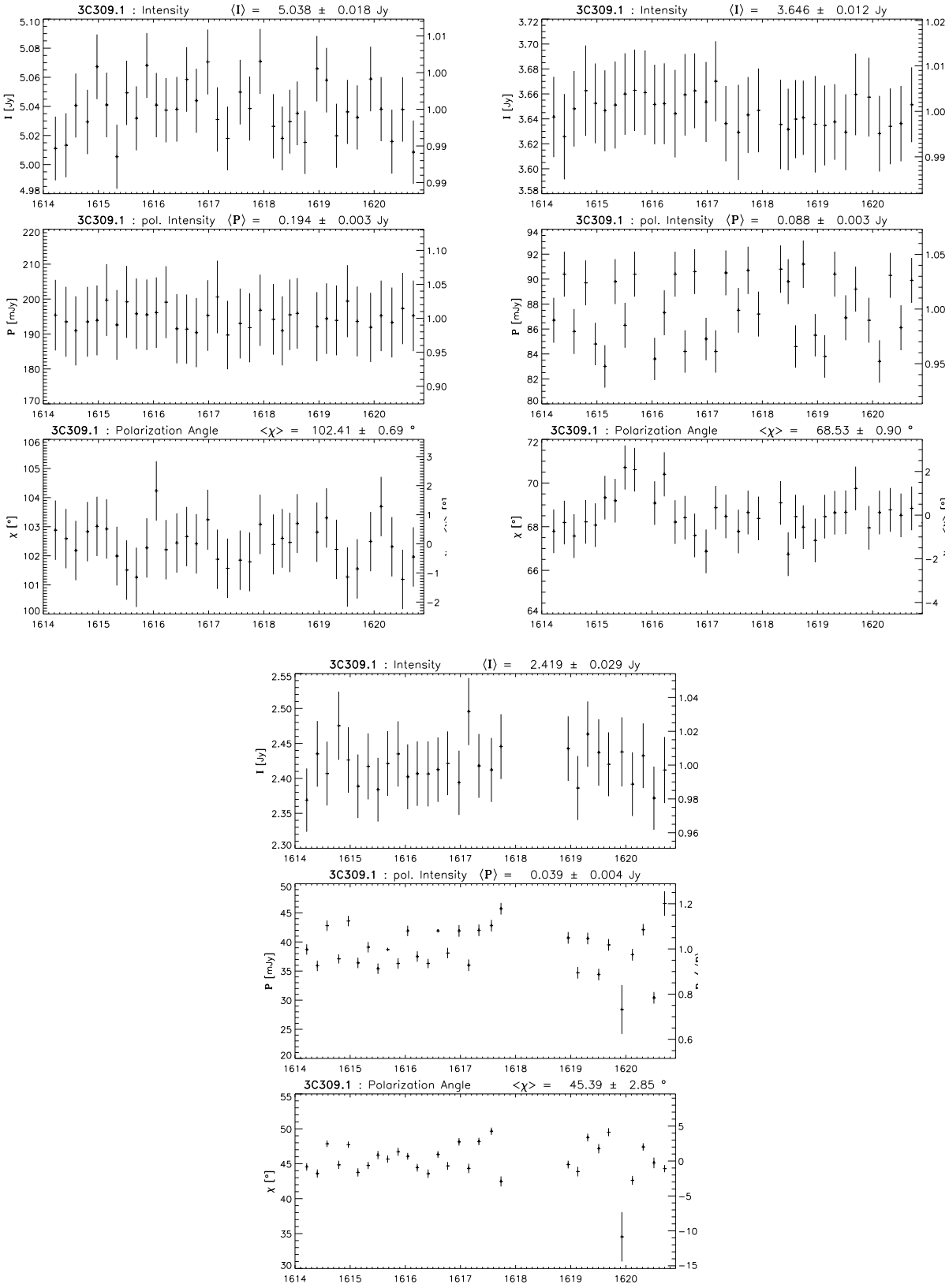

Figure A.7: 1458+71 in March 2000: total intensity and polarization. **Top left:** 11 cm. **Top right:** 6 cm. **Bottom:** 2.8 cm.

Appendix B

Observations at 345 GHz

In this section, the data at 345 GHz measured at the Heinrich Hertz Sub-Millimeter Telescope (HHT) of the Steward Observatory (Tucson, USA) are showed. The program sources are shown in table B: the measured flux densities, the errors and the number of measurements for each source are listed.
Furthermore, the light curves of the most frequently observed objects are shown. The plotted flux densities are normalized and an arbitrary scaling factor was used to compare the measurements of the program sources to the calibrators.

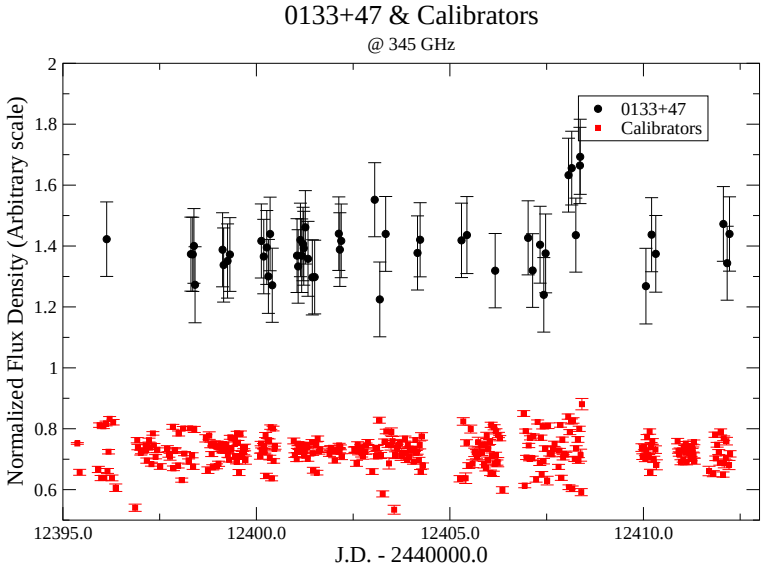

Figure B.1: 345 GHz light curve of 0133+47 compared to all the observed calibrators. $\chi^2_{red} = 0.645$

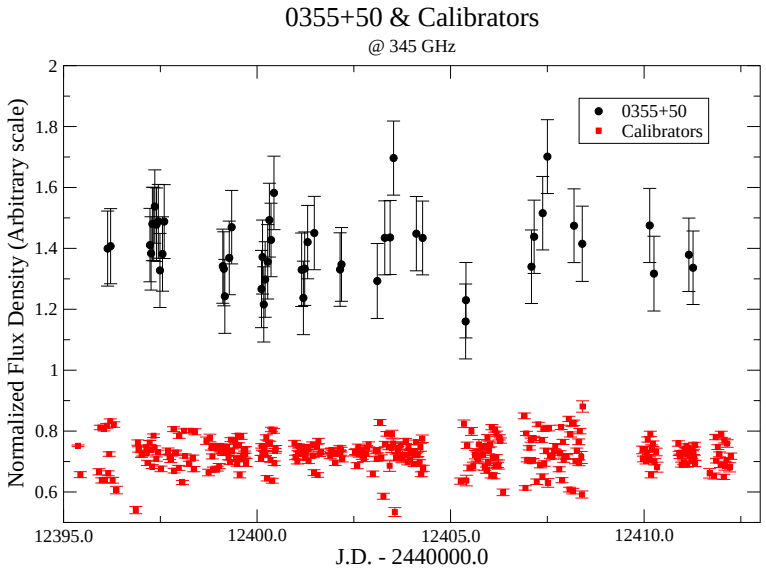

Figure B.2: 345 GHz light curve of 0355+50 compared to all the observed calibrators. $\chi^2_{red} = 0.791$

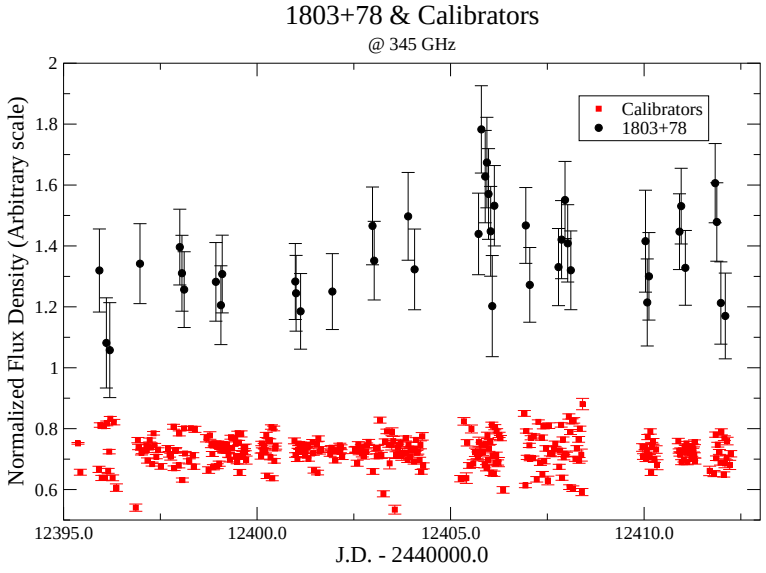

Figure B.3: 345 GHz light curve of 1803+78 compared to all the observed calibrators. $\chi^2_{red} = 1.252$

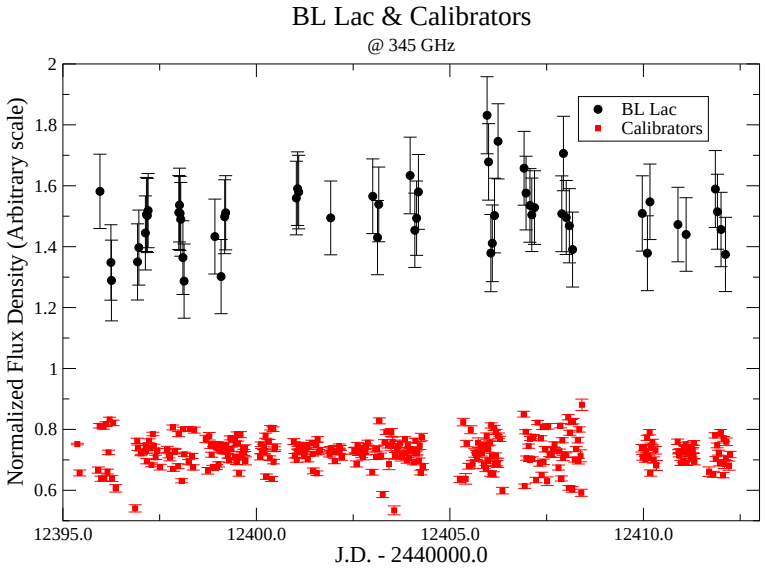

Figure B.4: 345 GHz light curve of 2200+42 compared to all the observed calibrators. $\chi^2_{red} = 0.763$

Source	$< S >$[Jy]	Err[Jy]	N
W3OH	26.034	1.565	149
NGC7027	4.268	0.344	7
NGC7538	21.193	2.982	3
GL490	5.741	0.419	12
K3-50A	17.460	0.887	67
G34.3	71.129	8.117	26
CWLEO	5.605	0.343	53
1757−24	34.525	4.913	24
0133+47	2.024	0.199	52
0355+50	2.736	0.297	50
0716+71	1.166	0.177	129
0736+01	2.309	0.297	5
0851+20	1.466	0.379	8
0923+39	1.067	0.176	8
0954+65	0.378	0.069	12
1156+29	1.542	0.160	3
1219+28	0.243	0.062	7
1226+02	4.049	0.449	12
1253−05	9.646	1.464	7
1308+32	0.906	0.153	19
1510−08	0.560	0.107	3
1622−29	0.225	0.028	3
1633+38	2.975	0.399	12
1641+39	2.285	0.031	2
1652+39	0.400	0.071	11
1730−13	2.500	0.257	14
1739+52	0.355	0.075	2
1741−03	1.758	0.152	6
1749+09	1.914	0.111	7
1803+78	0.879	0.138	43
1921−29	3.531	0.431	1
1928+73	0.919	0.232	2
2005+40	0.247	0.047	1
2007+77	0.448	0.065	1
2037+51	0.316	0.053	1
2013+37	1.322	0.163	1
2200+42	1.586	0.172	55
2201+31	0.537	0.034	5
2223−05	1.543	0.010	2
2230+11	2.409	0.292	1
2251+15	4.571	0.550	1

Table B.1: List of sources observed at 345 GHz in May 2002. The calibrators are listed in the **upper panel**.

Bibliography

J. R. P. Angel and H. S. Stockman. Optical and infrared polarization of active extragalactic objects. *ARA&A*, 18:321–361, 1980.

J. W. M. Baars, R. Genzel, I. I. K. Pauliny-Toth, and A. Witzel. The absolute spectrum of CAS A - an accurate flux density scale and a set of secondary calibrators. *A&A*, 61:99–106, October 1977.

U. Bach, T. P. Krichbaum, E. Ros, S. Britzen, A. Witzel, and J. A. Zensus. Is 0716+714 a superluminal blazar? In *Proceedings of the 6th European VLBI Network Symposium*, page 119, July 2002.

T. Beckert, L. Fuhrmann, G. Cimò, T. P. Krichbaum, A. Witzel, and J. A. Zensus. Understanding Scintillation of Intraday Variables. In *Proceedings of the 6th European VLBI Network Symposium*, page 79, July 2002a.

T. Beckert, T. P. Krichbaum, G. Cimò, L. Fuhrmann, A. Kraus, A. Witzel, and J. A. Zensus. The Size of IDV Jet Cores. *Publications of the Astronomical Society of Australia*, 19:55–59, 2002b.

G. Benford. Collective emission from rapidly variable quasars. *ApJL*, 391:L59–L62, June 1992.

G. Benford and H. Lesch. Coherent emission and the escape of high brightness temperature radiation in active galactic nuclei. *MNRAS*, 301:414–418, December 1998.

A. D. Biggs, I. W. A. Browne, P. Helbig, L. V. E. Koopmans, P. N. Wilkinson, and R. A. Perley. Time delay for the gravitational lens system B0218+357. *MNRAS*, 304:349–358, April 1999.

A. D. Biggs, I. W. A. Browne, and P. N. Wilkinson. Intrinsic intraday variability in the gravitational lens system B0218+357. *MNRAS*, 323:995–998, May 2001.

H. E. Bignall, D. L. Jauncey, L. L. Kedziora-Chudczer, J. E. J. Lovell, J.-P. Macquart, D. P. Rayner, S. J. Tingay, A. K. Tzioumis, R. W. Clay, R. G. Dodson, P. M. McCulloch, and G. D. Nicolson. New Results from an ATCA Study of Intraday Variable Radio Sources. *Publications of the Astronomical Society of Australia*, 19: 29–33, 2002.

M. Bondi, L. Padrielli, L. Gregorini, F. Mantovani, N. Shapirovskaya, and S. R. Spangler. One-year modulation in the flux density time series of low frequency variables. *A&A*, 287:390–402, July 1994.

A. W. Clegg, A. L. Fey, and T. J. W. Lazio. The Gaussian Plasma Lens in Astrophysics: Refraction. *ApJ*, 496:253, March 1998.

W. A. Coles, B. J. Rickett, J. L. Codona, and R. G. Frehlich. Refractive scintillation in the interstellar medium. *ApJ*, 315:666–674, April 1987.

J. M. Cordes and T. J. W. Lazio. Anomalous Radio-Wave Scattering from Interstellar Plasma Structures. *ApJ*, 549:997–1010, March 2001.

J. M. Cordes, S. R. Spangler, J. M. Weisberg, and T. R. Clifton. Galactic distribution of electron density turbulence. In *AIP Conf. Proc. 174: Radio Wave Scattering in the Interstellar Medium*, pages 180–184, 1988.

J. Dennett-Thorpe and A. G. de Bruyn. The Discovery of a Microarcsecond Quasar: J1819+3845. *ApJL*, 529:L65–L68, February 2000.

J. Dennett-Thorpe and A. G. de Bruyn. Monitoring the Microarcsecond Quasar J1819+3845. *Ap&SS*, 278:101–104, 2001.

R. A. Edelson and J. H. Krolik. The discrete correlation function: A new method for analyzing unevenly sampled variability data. In *A Decade of UV Astronomy with the IUE Satellite, Volume 2*, volume 2, pages 387–390, June 1988.

R. Fiedler, B. Dennison, K. J. Johnston, E. B. Waltman, and R. S. Simon. A summary of extreme scattering events and a descriptive model. *ApJ*, 430:581–594, August 1994.

R. L. Fiedler, K. J. Johnston, J. H. Spencer, E. B. Waltman, S. R. Florkowski, D. N. Matsakis, F. J. Josties, P. E. Angerhofer, W. J. Klepczynski, and D. D. McCarthy. Observations of SS 433 at 2695 and 8085 MHz, 1979-1985. *AJ*, 94:1244–1250, November 1987.

L. Fuhrmann, T. P. Krichbaum, G. Cimò, T. Beckert, A. Kraus, A. Witzel, J. A. Zensus, S. J. Qian, and B. J. Rickett. Annual Modulation in the Variability Properties of the IDV Source 0917+624? *Publications of the Astronomical Society of Australia*, 19:64–68, 2002.

D. C. Gabuzda and T. V. Cawthorne. The parsec-scale polarization structure of nine BL Lacertae objects at lambda=3.6cm. *MNRAS*, 283:759–776, December 1996.

J. A. Högbom. Aperture Synthesis with a Non-Regular Distribution of Interferometer Baselines. *A&AS*, 15:417–+, June 1974.

D. S. Heeschen. Flickering of extragalactic radio sources. *AJ*, 89:1111–1123, August 1984.

D. S. Heeschen, T. Krichbaum, C. J. Schalinski, and A. Witzel. Rapid variability of extragalactic radio sources. *AJ*, 94:1493–1507, December 1987.

P. A. Hughes, H. D. Aller, and M. F. Aller. Polarized Radio Outbursts in Bl-Lacertae - Part Two - the Flux and Polarization of a Piston-Driven Shock. *ApJ*, 298:301, November 1985.

D. L. Jauncey, L. L. Kedziora-Chudczer, J. E. J. Lovell, G. D. Nicolson, R. A. Perley, J. E. Reynolds, A. K. Tzioumis, and M. H. Wieringa. The Origin of Intra-Day Variability. In *Astrophysical Phenomena Revealed by Space VLBI, Proceedings of the VSOP Symposium, held at the Institute of Space and astronautical Science, Sagamihara, Kanagawa, Japan, January 19 - 21, 2000, Eds.: H. Hirabayashi, P.G. Edwards,*

and D.W. Murphy, Published by the Institute of Space and Astronautical Science, p. 147-150., pages 147–150, April 2000.

Jenkins and Watts. *Spectral Analysis and its Applications*. Holden Day, 1969.

T. W. Jones and S. L. O'dell. Transfer of polarized radiation in self-absorbed synchrotron sources. I - Results for a homogeneous source. *ApJ*, 214:522–539, June 1977.

S. G. Jorstad, A. P. Marscher, J. R. Mattox, A. E. Wehrle, S. D. Bloom, and A. V. Yurchenko. Multiepoch Very Long Baseline Array Observations of EGRET-detected Quasars and BL Lacertae Objects: Superluminal Motion of Gamma-Ray Bright Blazars. *ApJS*, 134:181–240, June 2001.

L. Kedziora-Chudczer, D. L. Jauncey, M. H. Wieringa, M. A. Walker, G. D. Nicolson, J. E. Reynolds, and A. K. Tzioumis. PKS 0405-385: The Smallest Radio Quasar? *ApJL*, 490:L9, November 1997.

L. L. Kedziora-Chudczer, D. L. Jauncey, M. H. Wieringa, A. K. Tzioumis, and J. E. Reynolds. The ATCA intraday variability survey of extragalactic radio sources. *MNRAS*, 325:1411–1430, August 2001.

K. I. Kellermann and I. I. K. Pauliny-Toth. The Spectra of Opaque Radio Sources. *ApJL*, 155:L71+, February 1969.

A. Koenigl and A. R. Choudhuri. Force-free equilibria of magnetized jets. *ApJ*, 289: 173–187, February 1985.

A. Kraus, T. P. Krichbaum, R. Wegner, A. Witzel, G. Cimò, A. Quirrenbach, S. Britzen, L. Fuhrmann, A. P. Lobanov, C. E. Naundorf, K. Otterbein, B. Peng, M. Risse, E. Ros, and J. A. Zensus. Intraday variability in compact extragalactic radio sources: II. Observations with the Effelsberg 100m radio telescope. *A&A*, 2003.

A. Kraus, A. Witzel, T. P. Krichbaum, A. P. Lobanov, B. Peng, and E. Ros. A change in the variability properties of the intraday variable quasar 0917+624. *A&A*, 352: L107–L110, December 1999.

E. Kreysa, H.-P. Gemünd, A. Raccanelli, L. A. Reichertz, and G. Siringo. Bolometer arrays for Mm/Submm astronomy. In *Experimental Cosmology at Millimetre Wavelengths: 2K1BC Workshop. AIP Conference Proceedings, Vol. 616. Breuil-Cervinia, Valle d'Aosta, Italy, 9-13 July, 2001. Edited by Marco De Petri and Massimo Gervasi. American Institute of Physics, 2002., p.262-269*, pages 262–269, 2002.

T. P. Krichbaum, A. Kraus, L. Fuhrmann, G. Cimò, and A. Witzel. Intraday Variability in Northern Hemisphere Radio Sources. *Publications of the Astronomical Society of Australia*, 19:14–18, 2002.

V. Krishan and P. J. Wiita. Plasma mechanisms for variability in active galactic nuclei. *ApJ*, 423:172–179, March 1994.

H. Kühr, A. Witzel, I. I. K. Pauliny-Toth, and U. Nauber. A catalogue of extragalactic radio sources having flux densities greater than 1 Jy at 5 GHz. *A&AS*, 45:367–430, September 1981.

M. P. C. Legg and K. C. Westfold. Elliptic Polarization of Synchrotron Radiation. *ApJ*, 154:499, November 1968.

A. P. Lobanov and J. A. Zensus. Spectral Evolution of the Parsec-Scale Jet in the Quasar 3C 345. *ApJ*, 521:509–525, August 1999.

J. Macquart. Circular Polarisation in AGN. *Publications of the Astronomical Society of Australia*, 19:43–48, 2002.

J.-P. Macquart, A. G. de Bruyn, and J. Dennett-Thorpe. The microarcsecond properties of J1819+385. In *Active Galactic Nuclei: from Central Engine to Host Galaxy Abstract Book, meeting held in Meudon, France, July 23-27, 2002, Eds.: S. Collin, F. Combes and I. Shlosman. To be published in ASP (Astronomical Society of the Pacific), Conference Series, p. 43.*, July 2002.

A. P. Marscher, S. G. Marchenko-Jorstad, J. R. Mattox, A. E. Wehrle, and M. F. Aller. High-Frequency Observations of Blazars. In *Astrophysical Phenomena Revealed by Space VLBI, Proceedings of the VSOP Symposium, held at the Institute of Space and astronautical Science, Sagamihara, Kanagawa, Japan, January 19 - 21, 2000,*

Eds.: H. Hirabayashi, P.G. Edwards, and D.W. Murphy, Published by the Institute of Space and Astronautical Science, p. 39-46., pages 39–46, April 2000.

J. R. Mattox, D. L. Bertsch, J. Chiang, B. L. Dingus, C. E. Fichtel, R. C. Hartman, S. D. Hunter, G. Kanbach, D. A. Kniffen, P. W. Kwok, Y. C. Lin, H. A. Mayer-Hasselwander, P. F. Michelson, C. von Montigny, P. L. Nolan, K. Pinkau, E. Schneid, P. Sreekumar, and D. J. Thompson. The EGRET detection of quasar 1633 + 382. *ApJ*, 410:609–614, June 1993.

R. Narayan. The physics of pulsar scintillation. *Phil. Trans. R. Soc. Lond.*, 1992.

T. E. Nordgren, J. M. Cordes, and Y. Terzian. The scale height of the galactic free electron cloud. *AJ*, 104:1465–1471, October 1992.

M. Ott, A. Witzel, A. Quirrenbach, T. P. Krichbaum, K. J. Standke, C. J. Schalinski, and C. A. Hummel. An updated list of radio flux density calibrators. *A&A*, 284: 331–339, April 1994.

P. Padovani and P. Giommi. A Sample-Oriented Catalogue of Bl-Lacertae Objects. *MNRAS*, 277:1477, December 1995.

J. R. Pardo, J. Cernicharo, and E. Serabyn. . *IEEE transc. Antennas and Propagation*, 2001.

S. Qian, A. Kraus, X. Zhang, T. P. Krichbaum, A. Witzel, and J. A. Zensus. Multifrequency Polarization Variations in the Quasar 0917+624. *Chinese Journal of Astronomy & Astrophysics, Vol. 2, p. 325-346*, 2:325–346, August 2002.

S. Qian and X. Zhang. Annual Modulation in Intraday Variability Timescales of Extragalactic Radio Sources. *Chinese Journal of Astronomy & Astrophysics, Vol. 1, p. 133-143*, 1:133–143, April 2001.

S. J. Qian, A. Quirrenbach, A. Witzel, T. P. Krichbaum, C. A. Hummel, and J. A. Zensus. A model for the rapid radio variability in the quasar 0917 + 624. *A&A*, 241: 15–21, January 1991.

S. J. Qian, A. Witzel, A. Kraus, T. P. Krichbaum, and S. Britzen. Spectral Evolution of the Intraday Variations in the QSO 0917+624. In *ASP Conf. Ser. 100: Energy Transport in Radio Galaxies and Quasars*, pages 55–+, 1996.

S. J. Qian, A. Witzel, A. Kraus, T. P. Krichbaum, and J. A. Zensus. Rapid polarization variations at 20 cm in 0917+624. *A&A*, 367:770–779, March 2001.

A. Quirrenbach, A. Kraus, A. Witzel, J. A. Zensus, B. Peng, M. Risse, T. P. Krichbaum, R. Wegner, and C. E. Naundorf. Intraday variability in compact extragalactic radio sources. I. VLA observations. *A&AS*, 141:221–256, January 2000.

A. Quirrenbach, A. Witzel, T. P. Kirchbaum, C. A. Hummel, R. Wegner, C. J. Schalinski, M. Ott, A. Alberdi, and M. Rioja. Statistics of intraday variability in extragalactic radio sources. *A&A*, 258:279–284, May 1992.

B. J. Rickett, L. Kedziora-Chudczer, and D. L. Jauncey. Interstellar Scintillation of the Polarized Flux Density in Quasar PKS 0405-385. *ApJ*, 581:103–126, December 2002.

B. J. Rickett, A. Quirrenbach, R. Wegner, T. P. Krichbaum, and A. Witzel. Interstellar scintillation of the radio source 0917+624. *A&A*, 293:479–492, January 1995.

D. H. Roberts, J. Lehar, and J. W. Dreher. Time Series Analysis with Clean - Part One - Derivation of a Spectrum. *AJ*, 93:968, April 1987.

J. Rutman. Characterization of Phase and Frequency Instabilities in Precision Frequency Suoces: Fifteen Years of Progress. In *Proceeding of the IEEE*, 1978.

N. Y. Shapirovskaya and T. I. Larchenkova. The galactic latitude distribution of the intensity modulation index of radio sources in the wide frequency range. *Astronomical and Astrophysical Transactions*, 7:29–45, April 1995.

G. Siringo. *PolKa: A Polarimeter for Submillimeter Bolometer Arrays*. PhD thesis, 2003.

G. Siringo, L. A. Reichertz, and E. Kreysa. PolKa: A tunable polarimeter for mm/submm wavelengths. In *Experimental Cosmology at Millimetre Wavelengths:*

2K1BC Workshop. AIP Conference Proceedings, Vol. 616. Breuil-Cervinia, Valle d'Aosta, Italy, 9-13 July, 2001. Edited by Marco De Petri and Massimo Gervasi. American Institute of Physics, 2002., p.187-189, pages 187–189, 2002.

M. Stickel, K. Meisenheimer, and H. Kühr. The optical identification status of the 1 Jy radio source catalogue. *A&AS*, 105:211–234, June 1994.

K. Subramanian and Gopal-Krishna. Enhanced probability of intensity outbursts via superluminal microlensing of quasars. *A&A*, 248:55–+, August 1991.

C. Thum, H. Wiesemeyer, S. Navarro, D. Morris, and M. Torres. Versatile if polarimeter at the iram 30m telescope. In *Polarimetry in Astronomy*, 2002.

Z. Turlo, T. Forkert, W. Sieber, and W. Wilson. Calibration of the instrumental polarization of radio telescopes. *A&A*, 142:181–188, January 1985.

G. L. Verschuur and K. I. Kellermann. *Galactic and extra-galactic radio astronomy* Berlin: Springer, 1988, 2nd ed., edited by Verschuur, Gerrit L.; Kellermann, Kenneth I., 1988.

S. J. Wagner. Intraday Variability of Flat-Spectrum Radio Sources. In*ASP Conf. Ser. 144: IAU Colloq. 164: Radio Emission from Galactic and Extragalactic Compact Sources*, page 257, 1998.

S. J. Wagner and A. Witzel. Intraday Variability In Quasars and BL Lac Objects. *ARA&A*, 33:163–198, 1995.

S. J. Wagner, A. Witzel, J. Heidt, T. P. Krichbaum, S. J. Qian, A. Quirrenbach, R. Wegner, H. Aller, M. Aller, K. Anton, I. Appenzeller, A. Eckart, A. Kraus, C. Naundorf, R. Kneer, W. Steffen, and A. Zensus. Rapid Variability in S5 0716+714 Across the Electromagnetic Spectrum. *ApJ*, 111:2187, June 1996.

S. J. Wagner, A. Witzel, T. P. Krichbaum, R. Wegner, A. Quirrenbach, K. Anton, U. Erkens, R. Khanna, and A. Zensus. Intraday variability in the BL Lac object 0954 + 658. *A&A*, 271:344, April 1993.

M. A. Walker. Interstellar scintillation of compact extragalactic radio sources.*MNRAS*, 294:307, February 1998.

J. Wambsganss and T. Kundic. Gravitational Microlensing by Random Motion of Stars: Analysis of Light Curves. *ApJ*, 450:19, September 1995.

A. Witzel, D. S. Heeschen, C. Schalinski, and T. Krichbaum. Kurzzeit-Variabilität extragalaktischer Radioquellen. *Mitteilungen der Astronomischen Gesellschaft, Vol. 65, p.239*, 65:239, 1986.

Acknowledgments

In the very last pages of my thesis, I wish to express my gratitude to all the people who helped me to arrive at the end of such important and difficult task.

First of all, I would like to thank Dr. J. A. Zensus, director of the VLBI group of the Max-Planck-Institut für Radioastronomie, who gave me the opportunity to work in this institute.

I wish to especially thank Dr. Arno Witzel for his helpful guidance during my work. He was of great help not only for the scientific support but for also being open to any kind of discussion, and there to help with all sorts of problems.

For his constant presence and continuous help, I would like to thank Dr. Thomas Krichbaum, whose countless ideas contributed to this thesis. Much of this work owes to the numerous fruitful discussions with him.

I would like to thank all the members of the VLBI group. I spent three years in a very inspiring and friendly working atmosphere. In particular, my gratitude goes to Dr. Alex Kraus and Dr. Thomas Beckert for their help in my understanding of the mathematical problems and the theoretical implications of my Ph.D. project. A special thank goes to Violetta Impellizzeri and all the other students of the VLBI group.

Countless valuable advice for my work came from Lars Fuhrmann: my room-mate but, mainly, a Friend. He was always present in all the important moments of these three years, whether on top of a mountain in Arizona or in the middle of the Australian desert.

I am grateful to the staff at the Effelsberg radio telescope for their support during the observations.

I wish to thank Prof. Dr. U. Klein and Prof. Dr. W. Huchtmeier for supervising this thesis.
My thanks go to Dr. E. Kreysa, for the fruitful collaboration during the first observing session at the Heinrich-Hertz-Telescope. Thanks also to Dr. C. Thum and Dr. H. Wiesemeyer from IRAM, the 3 mm polarimetry experiment would not have been possible without their help and their advice.

I thank the members of the MPIfR soccer team, in the hope that they will forgive me for deserting them on rainy days.

My special gratitude goes to Giorgio Siringo, for the interesting scientific discussion (in particular about high frequency polarimetry), but especially for his friendship in every moment.
I also wish to remember all my friends here in Bonn: Cristina, Violetta, Claudia, Silvia, Andrea "Hans Pils" and all the others, who crossed my life during these years. I will never forget you.

Last, but not least, I wish to thank my family. They live far away but I feel them always close to me. Grazie!